NORTHWESTERN UNIVERSITY

Electrodynamics of particles in bulk fluid and on an interface

A DISSERTATION

SUBMITTED TO THE GRADUATE SCHOOL
IN PARTIAL FULFILLMENT OF THE REQUIREMENTS

for the degree

DOCTOR OF PHILOSOPHY

Field of Engineering Sciences and Applied Mathematics

By

Yi Hu

EVANSTON, ILLINOIS

September 2021

© Copyright by Yi Hu 2021
All Rights Reserved

ABSTRACT

Electrodynamics of particles in bulk fluid and on an interface

Yi Hu

The focus on this thesis is on the dynamics of colloidal particles in an applied electric field in a uniform bulk fluid and on a fluid-fluid interface. In a bulk fluid, the dynamics of an isolated particle, one pair, and a cluster of particles under an applied nonuniform electric field are modeled and simulated. The local and far-field electric field perturbation by a spherical particle trapped at a fluid-fluid interface is also studied. The electric potential is found by using the Mehler-Fock integral transform, which reduces the problem to a system of Fredholm integral equations. These equations are solved numerically and asymptotically. The force on an isolated particle is identified numerically, while the far-field interaction force between two particles is identified asymptotically. We show that, at leading order, the interaction between perfect dielectric particles is dominated by the induced dipoles and hence it is repulsive. For leaky dielectric particles the induced quadrupole can become significant and the interaction force can be either attractive or repulsive depending on material parameters. Moreover, a mathematical model to simulate the dynamics of colloidal particles on a drop interface in an applied electric field is presented. The model accounts for the electric field driven flow within the drop and suspending fluid, particle-particle electrostatic interaction, and the particle motion and rotation due to the induced flow and the applied electric field. A study is presented on the impact of particle concentration and electric field strength on the collective motions of the particles. In the case of non-conducting particles, we find that in the presence of Quincke rotation, the amplitude of the undulations of the observed equatorial particle belt increases with particle concentration but decreases with electric field strength. We also show that the wavelength of the undulations appears independent of the applied field strength.

Acknowledgements

Firstly, I would like to thank my advisor: Prof. Michael Miksis. He has given me the best instructions and patience for all the problems when doing this research. I also appreciate all the work he devoted to help me publish the three journal papers. The moments of academic travelling with him to SIAM and APS meetings in the U.S and abroad are also unforgettable.

My thanks also goes to my co-advisor: Prof. Petia Vlahovska. I can still remember the time I met her in Brown University and the moment I come around with those insteresting experiment videos. She also gave me the best support and advices throughout my study.

I would also like to thank Prof. David Chopp to join my thesis committee. I learned the skill of parallel computing used in this research from his High Performace Computation class.

Additional thanks to Prof. Alvin Bayliss, Prof. Vladimir Volpert and all other department faculties who taught me the best applied mathematic courses and gave me many help in person as well.

Finally, I would thank my family and friends for their love and company.

Table of Contents

ABSTRACT 3

Acknowledgements 5

Table of Contents 6

List of Tables 9

List of Figures 10

Chapter 1. Introduction 15

- 1.1. Collective Motions of Colloidal Particles on Drop Surface 15
- 1.2. Liquid Drop Electrohydrodynamics: Leaky-dielectric Model 16
- 1.3. Particle Dielectrophoresis 19
- 1.4. Outline of This Thesis 21

Chapter 2. Particle Electrodynamics in A Non-uniform Electric Field 23

- 2.1. Problem Formulation 23
- 2.2. An Isolated Sphere in A Linear Electric Field 31
- 2.3. Multi-particle System in Linear Electric Fields 37
- 2.4. Multi-particle Dynamics in Slowly Varying Non-uniform Fields 50
- 2.5. Conclusion 58

Chapter 3. Colloidal Particle at A Fluid-fluid Interface 61
3.1. Introduction 61
3.2. Problem Formulation 63
3.3. Computational Results: Induced Potential Lines 76
3.4. Electric Field Near the Contact Line 76
3.5. Electric Force on An Isolated Particle 82
3.6. Far-field Asymptotic Expansion of Potentials 86
3.7. Interaction of Widely Separated Particles 92

Chapter 4. Electrohydrodynamic assembly of colloidal particles on a drop interface 103
4.1. Introduction 103
4.2. Problem Formulation 105
4.3. Simulation Results 111
4.4. Conclusion 122

Chapter 5. Conclusion 125

References 128

Appendix A. Symmetries of the multipole moments 138

Appendix B. Mehler-Fock Integral Transform 139

Appendix C. Functions in The Integral Equations of Section 3.2.3 140

Appendix D. Convergence tests on the numerical solution of far-field coefficients for Chapter 3 142

Appendix E. Proving 3.113 using an analogy of the method by Danov and Kralchevsky, when $\gamma = \epsilon$, in a tangential field 144

Appendix F. Proving $\mathcal{F}^{\mathcal{I}}_{c3,d} = \frac{5}{3}\mathcal{F}^{\mathcal{I}}_{c,d}$ when $\gamma = \epsilon$ in Chapter 3 148

List of Tables

D.1 Convergence with respect to the grid size $\Delta\tau$. Integration upper bound $\tau_U = 60$. 142

D.2 Convergence with respect to the integration upper bound τ_U. $\Delta\tau = 1/200$. 143

List of Figures

1.1 Circulation inside and outside of a silicon oil drop in a mixture of castor oil and corn oil in a DC field directed vertically. 17

1.2 Fluid streamlines inside and outside of a silicon oil drop in a mixture of castor oil and corn oil in a DC field directed vertically, assuming undeformed surface. 20

2.1 One particle trajectory starting at $x = 2.5$, $z = 6.0$. Initial perturbations at the magnitude of $O(10^{-4})$ are randomly generated. The red circle indicates the non-Quincke region satisfying Eq. 2.28. The markers p1 to p4 indicate four positions when z first hits the value of $0.0, 1.0, 2.0, 3.0$. $G = 0.4000$. The particle does not rotate in the equilibrium state. 37

2.2 The evolution of corresponding multiple moments and rotation rate to the single particle dynamic in Fig 2.1. 38

2.3 Particle trajectories in different field gradient strength. Initial position $x = 5.0$, $z = 2.0$ and a random initial polarization perturbation at $O(10^{-4})$. $D = 5.1520$, $D' = 5.6054$. (a). $G = 1.0$, (b). $G = 2.3$, (c). $G = 3.0$. The final time interval $\tilde{t} = 380 - 400$ is indicated by red color. 39

2.4 Stationary trajectory shape vs G. r_a and r_b are the short and long radius of the steady orbit. When no steady orbit is observed, r_a and r_b are the minimum and maximum distance to the origin in a chosen time frame. $D' = 5.6054$, $\epsilon'_{cm} = -0.0670$, $\sigma'_{cm} = -0.3333$. 40

2.5 Particle dynamic patterns with different field strength parameter G. Initial $\mathbf{P}$ is given randomly at $O(10^{-4})$ The non-electrorotation region is indicated by the circle satisfying Eq. 2.28. $D = 5.1520$, $D' = 5.6054$. (a) co-rotating pair, $G = 0.1$, (b) counter-rotating pair, $G = 0.1$, (c) co-rotating pair, $G = 1.0$, (d) counter-rotating pair, $G = 1.0$. 49

2.6 Dynamics of 20 particles in linear field with random initial positions. Chaining at Y-axis is observed. $G = 1.0$. $D = 5.1520$. $\tilde{t} = 0, 20, 200, 2000$. 50

2.7 Dynamics of 60 particles in periodical field with random initial positions with $\tilde{x} \in [0, 60]$. Clustering at $\tilde{z} = 0$ plane is observed. Four chains are formed at $\tilde{x} = 8, 24, 40, 56$. $E_0/E'_c = 1.0$. $\delta' = \frac{\pi}{16}$. $D = 5.1520$. $\tilde{t} = 0, 20, 200, 2000$. 59

3.1 Spherical particle trapped at fluid-fluid interface. The x-axis of a cartesian system (x, y, z) is noted in the figure. 64

3.2 Toroidal coordinates system. 67

3.3 Applied normal electric field. Equal potential lines of Φ_k, $\alpha = \pi/2$, $\gamma_{ul} = 4$. (a) $\gamma_{pl} = 1/2$. (b) $\gamma_{pl} = 2$, for better demonstration, smaller potential level is used. Select values of the potential are noted on each figure. 77

3.4 Applied tangential electric field. Equal potential lines of Φ_k, $\alpha = \pi/2$, $\gamma_{ul} = 4$. (a) $\gamma_{pl} = 1/2$. (b) $\gamma_{pl} = 2$, for better demonstration, smaller potential level is used. Select values of the potential are noted on each figure. 77

3.5 ν vs. α for different values of γ_{ul} with $\gamma_{pl} = 1$. Here α is given in degrees. The $\gamma_{ul} \to \infty$ limit recovers the case considered in the study done by Danov and Kralchevsky. 81

3.6 In applied normal field. Here $\gamma = \epsilon$. (a) $\mathcal{F}^{\mathcal{S}}$ vs. ϵ_{pl}, when $\epsilon_{ul} = 1, 2, 4, 16, 100$. $\alpha = \pi/2$. (b) $\mathcal{F}^{\mathcal{S}}$ vs. α. $\epsilon_{ul} = 4$, $\epsilon_{pl} = 1/4, 1, 2, 4, 16$. 84

3.7 In applied tangential field with $\gamma = \epsilon$. (a) $\mathcal{F}^{\mathcal{S}}$ vs. ϵ_{pl}, when $\epsilon_{ul} = 1, 4, 16, 100$. $\alpha = \pi/2$. (b) $\mathcal{F}^{\mathcal{S}}$ vs. α. $\epsilon_{ul} = 4$, $\epsilon_{pl} = 1/4, 1, 2, 4, 16$. 86

3.8 (Normal field) C_2^l and C_4^l when $\alpha = \pi/2$. (a) C_2^l vs. γ_{pl}, when $\gamma_{ul} = 1, 4, 16, 100$, (b) C_2^l vs. γ_{ul}, when $\gamma_{pl} = 1, 4, 16, 100$, (c) C_4^l vs. γ_{pl}, when $\gamma_{ul} = 1, 4, 16, 100$, (d) C_4^l vs. γ_{ul}, when $\gamma_{pl} = 1, 4, 16, 100$. 90

3.9 (Normal field) (a) C_2^l vs. α in degrees, when $\gamma_{pl} = 1/4, 1/2, 1, 2, 4, 16$, $\gamma_{ul} = 4$. The solid lines are numerical results while the broken lines at the approximate solutions C_{2A}^l. (b) C_4^l vs. α in degrees, when $\gamma_{pl} = 1/4, 1/2, 1, 2, 4, 16$, $\gamma_{ul} = 4$. 91

3.10 Particle locations in inter-particle force calculation. Normal field: assume the second particle centered at $(R_0, 0, -\cos\alpha)$, without losing any generality. Tangential field: assume the second particle centered at $(R_0 \cos\beta, R_0 \sin\beta, -\cos\alpha)$. 93

3.11 (Normal field) $\mathcal{F}^{\mathcal{I}}$ vs. γ_{pl}, $\alpha = 2\pi/3$. (a) $\gamma = \epsilon$, $\epsilon_{ul} = 2, 4, 16$. (b) $\gamma = \sigma$, $\sigma_{ul} = 2, 4, 16$ and $\epsilon_{ul} = 1$ is used for all cases. 96

3.12 (Tangential field) $\mathcal{F}_{c,d}$ (solid lines) and $\mathcal{F}_{c,q}$ (dashed lines) vs. σ_{pl} when $\sigma_{ul} = 2, 4, 16$. $\alpha = \pi/2$ and $\epsilon_{ul} = 1$ is used. 101

4.1 Sketch of the problem: Colloidal spheres with radius a are trapped at the interface of a drop with radius R_0, $a/R_0 << 1$. The dielectric constants of the particles, drop, and suspending fluid are ϵ_p, ϵ_d, and ϵ_f, conductivities are σ_p, σ_d, and σ_f, and the viscosities of the drop and suspending fluids are μ_d, μ_f, respectively. A uniform DC electric field **E** is applied globally. **n** and **t** are unit normal and tangential vectors on the drop surface. 106

4.2 512 particles on a spherical drop. The particle size is for illustrative purposed. Large particle are on the near face of the 3D sphere while small particles are projections from the rear of the sphere. a. Initial random distribution. b. Particle distribution at $t = t_f$ with $E_0 = 200V/mm$. Red particles are rotating clockwise, blue particles are rotating counter-clockwise.c .Particle distribution at $t = t_f$ with $E_0 = 100V/mm$ 112

4.3 Particle distribution at $t = t_f$ for $N = 512$ particles with $E = 200V/mm$. The damping parameter $\chi = 1.0$. 115

4.4 $E_0 = 200V/mm$ on a spherical drop. Red particles are rotating clockwise, blue particles are rotating counter-clockwise. a. $N = 256$, $t = t_f$. b. .$N = 1024$ particles, $t = t_f$. c .$N = 2048$ particles, $t \approx t_f$. 116

4.5 Particle distribution at $t = t_f$ for $N = 512$ particles with $E_0 = 400V/mm$ 118

4.6 Amplitude of the angle of oscillation A_θ in radians as a function of electric field strength E_0 for $N = 512$ and 1014 particles. 120

4.7 Wave number of maximum amplitude A_w as a function of electric field strength E_0 for 512 and 1014 particles 121

4.8 Steady state 512 particle distribution. High conductivity. $E_0 = 200V/m$ 123

E.1 Two widely separated particles at $(-R_0/2, 0, -\cos\alpha)$ and $(R_0/2, 0, -\cos\alpha)$, where $R_0 >> 1$. A general tangential field (parallel to $x-y$ plane) is imposed in the entire space. For simplicity, we assume the gradient of the applied potential $\nabla\phi_a$ inclines at an angle β with respect to the line connecting particle centers, as shown above. Parallel auxiliary planes are used for the derivation of inter-particle force. 144

F.1 Geometry of applying divergence theorem. 148

CHAPTER 1

Introduction

1.1. Collective Motions of Colloidal Particles on Drop Surface

Colloidal particles are one of the most interesting topics which can be seen in various research fields like material science, biology and chemical engineering. A colloidal suspension refers to a mixture composed by microscopically dispersed insoluble particles, as the dispersed phase, and another substance, usually fluids, as the continuous phase. Typical diameters of colloidal particles in previous studies range from several nanometers to hundreds of micrometers.

Emulsions of particle-coated drops (so called Pickering emulsions [**1, 2**]) are widely used in the pharmaceutical, food, personal care and many other industries [**3**]. Colloidosomes, which are microcapsules with shells made of colloid particles [**4**], are used for drug delivery due to the great degree of control of the shell permeability [**5**]. Colloidal particles get trapped at interfaces between immiscible (e.g., oil/water) fluids [**6**] (since the energy to detach a particle adsorbed at an interface exceeds the thermal energy by the thousands) and at high packing density form a shell encapsulating the drop that stabilizes emulsions against coalescence and enables selective permeability [**4, 7, 8, 9, 10**]. Colloids at low surface coverage, however, do not form static structures, but instead assemble dynamically [**11, 12, 13, 14**]. For example, a uniform electric field was found to induce various patterns such as an equatorial belt, pole-to-pole chains or a band of dynamic vortices [**11, 12**]. The latter intriguing phenomenon has not been explained thus far and motivates our study.

The presence of the interface strongly modifies the electrostatic and hydrodynamic interactions between the particles, and introduces new interactions such as the classic capillary attraction (Cheerios effect)[**15**]. The latter arises from local deformation of the interface (e.g., if the particle has weight) [**16, 17, 18, 19, 20**]. The interfacial distortions increase the interfacial area and thus raise the interfacial free energy; one way of minimizing this effect is to bring the particles together so that their menisci overlap. The electrostatic interaction between charged particles in the absence of electric field [**21**] or in the presence of electric field [**22, 23**] can significantly differ from the particle interactions in a homogeneous medium.

1.2. Liquid Drop Electrohydrodynamics: Leaky-dielectric Model

To understand the motion of trapped colloidal particles along a drop interface, we first must consider the Electrohydrodynamics(EHD) behavior of a clean liquid drop. EHD usually refers to the motion of a fluid media induced by an applied electric field, which is of interest in a wide variety of scientific and engineering applications. An early record of an electrohydrodynamic experiment is the observation of forming a conical shape upon bringing a charged rod above a sessile drop [**24**]. Unlike the perfect conductor or perfect dielectric, the study on weakly conducting fluids started in the 1960s when Taylor[**25**] introduced the leaky dielectric model to explain the behavior of droplets deformed by a steady field, and Melcher used it extensively to develop electrohydrodynamics[**26**]. The EHD phenomenon studied by Taylor can be seen in fig. 1.1 which is taken from[**26**].

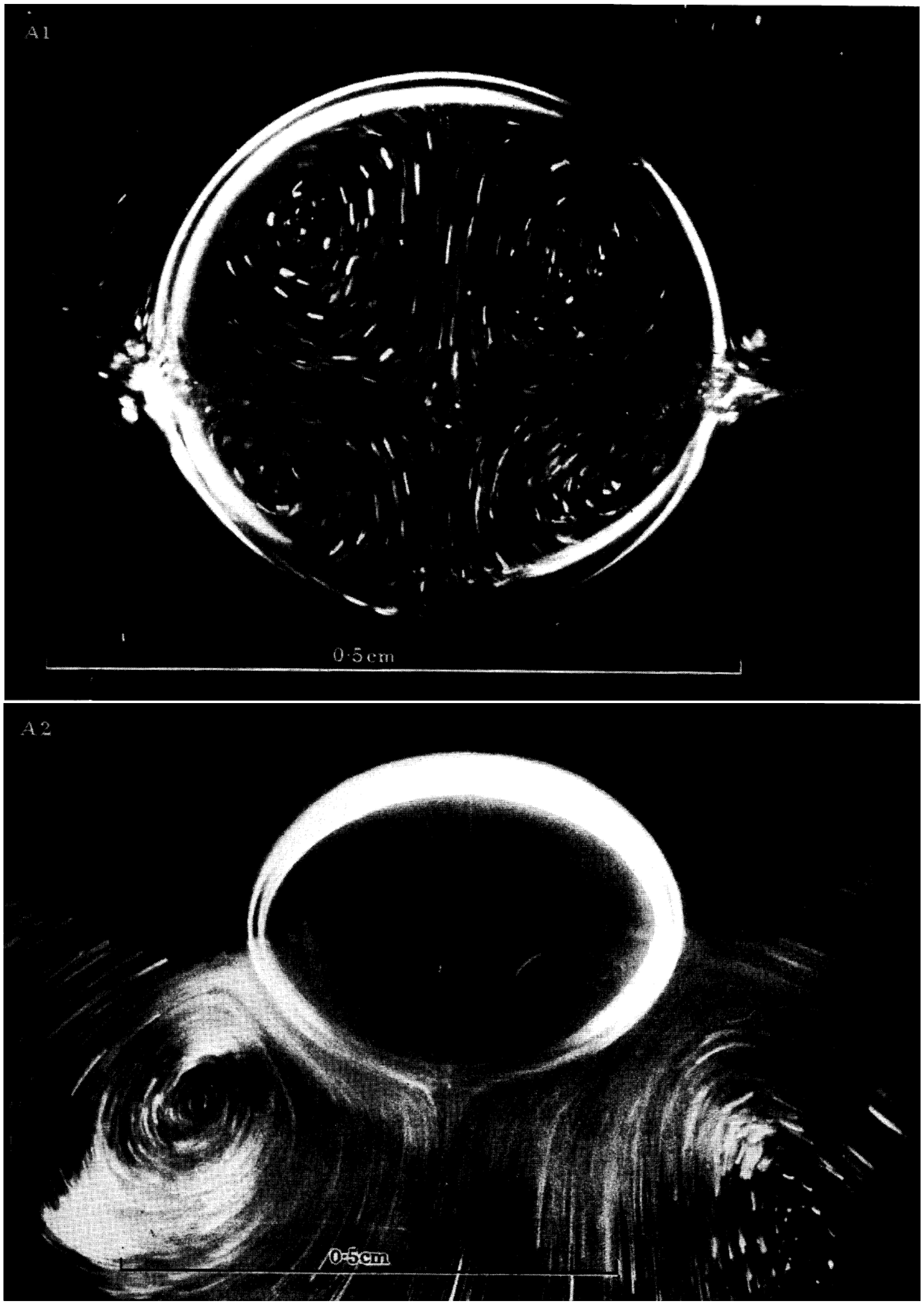

Figure 1.1. Circulation inside and outside of a silicon oil drop in a mixture of castor oil and corn oil in a DC field directed vertically.

The Taylor-Melcher leaky dielectric model consists of fluid motion described by the Stokes' equation, and the conservation of current employing an Ohmic conductivity. At the fluid-fluid interface, the charge gradient brought by conduction produces a tangential electric stresses, which are different from those present in perfect conductors and perfect dielectrics, where only normal stresses are present. Free charge accumulated on the interface modifies the field, while viscous drag from the flow balances the tangential Maxwell electric stress.

The incompressible Stokes' equation for Newtonian fluid reads,

$$-\nabla p + \mu \nabla^2 \mathbf{u} = 0, \tag{1.1}$$

$$\nabla \cdot \mathbf{u} = 0, \tag{1.2}$$

where μ is the kinetic viscosity. p and $\mathbf{u}$ are the fluid pressure and velosity vector, respectively.

The electric problem defined by the conservation of current $\mathbf{J} = \sigma \mathbf{E}$ in the bulk is given by

$$\nabla \cdot \sigma \mathbf{E} = 0, \tag{1.3}$$

where σ is the Ohmic conductivity, $\mathbf{E}$ is the electric field vector (either in the particle or fluid). Zero local free charge density is assumed.

The fluid and electric problem coupling also happens at the interface boundary where,

$$\frac{\partial q}{\partial t} + \mathbf{n} \cdot [\sigma \mathbf{E}] + \nabla_s \cdot (q\mathbf{u}) = 0, \tag{1.4}$$

$$\mathbf{n} \cdot [\epsilon \mathbf{E}] = q, \tag{1.5}$$

where q is the surface charge density, ϵ is the dielectric constants of the medium, $\mathbf{n}$ is the unit normal vector to particle interface, $\nabla_s = (\mathbf{I} - \mathbf{nn}) \cdot \nabla$, and $[f]$ represents the jump in f across the interface[**27**].

Taylor[**25**] derived a steady solution for the fluid flow about a spherical drop in a uniform applied electric field using his leaky dielectric model(without convection). The stream lines for his solution are illustrated in fig. 1.2 which is taken from[**26**].

In an expansion in small capillary number, the first correction to the balance of normal stresses at the interface can be used to predict the deformation of the surface shape.

Applications of electrohydrodynamics abound: spraying, the dispersion of one liquid in another, coalescence, ink jet printing, boiling, augmentation of heat and mass transfer, fluidized bed stabilization, pumping, and polymer dispersion are but a few. Some applications of EHD are striking.

1.3. Particle Dielectrophoresis

Besides the EHD flow, the dielectrophoresis interactions between particles induce sustainable collective motion. The spontaneous rotation of a particle in a uniform electric field, first observed over a century ago [**28**] and now known as Quincke rotation, has been subject of increasing interest in recent years. An isolated sphere [**29, 30**] or ellipsoid [**31, 32**] displays various rotational motions including chaotic reversal of the direction of

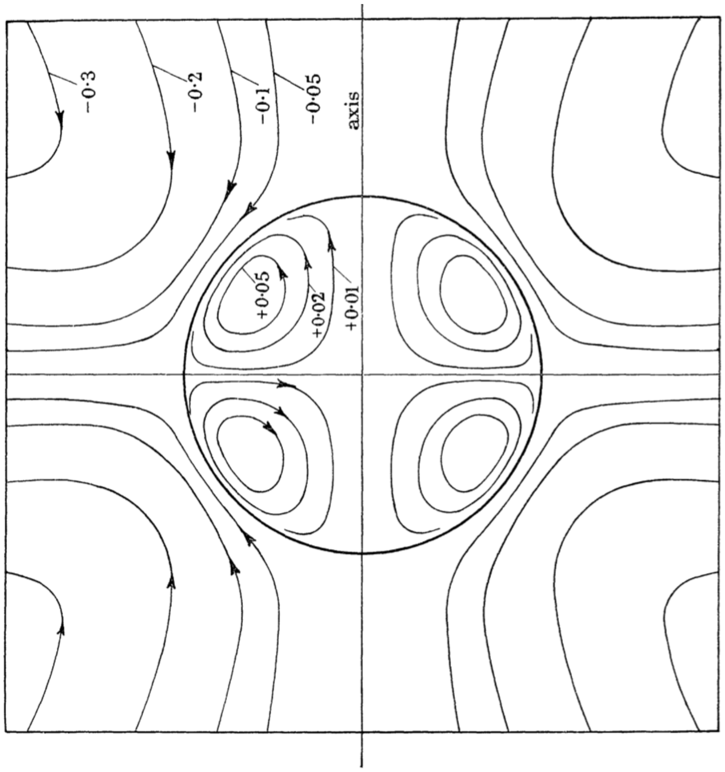

Figure 1.2. Fluid streamlines inside and outside of a silicon oil drop in a mixture of castor oil and corn oil in a DC field directed vertically, assuming undeformed surface.

rotation. Even more complex dynamics is found in a collection of particles. A pair of spheres can undergo intricate trajectories [**33, 34, 35**], large populations can self-organize in dynamic patterns [**36, 37, 38, 39, 40, 41, 42**], and a suspension can exhibit lower effective viscosity [**43, 44, 45**] or increased conductivity [**46**] compared to the suspending fluid.

While the Quincke rotation of an isolated particle in a uniform electric field is well understood [**30, 47, 48**], the collective dynamics of many Quincke rotors is a largely unexplored problem. Its modeling is particularly challenging because the induced dipole of a particle is affected by the presence of other particles. Hence, the question arises

- how is electrorotation affected by nonuniformities in the electric field (either due to the presence of other particles, or applied by design, i.e., using complex arrangement of electrodes)? A non-uniform field also induces dielectrophoresis [**49, 50, 51**], hence the overall particle dynamics becomes a complex mix of translation and rotation.

We will also explore the dynamics of spheres in a nonuniform DC electric field. In the case of an isolated sphere, we derive the threshold for Quincke rotation in a linear field. In the case of a pair of spheres, we identify the evolution equations for the multipolar moments (dipole and quadrupole) and particle positions. The model we developed can be generalized to many particles and arbitrary non-uniform fields.

1.4. Outline of This Thesis

In this thesis, we discuss electric-induced particle motion in a homogeneous fluid and with a fluid-fluid interface. The results provide insights concerning the collective motion of particles.

In Chapter 2, we investigate the colloidal particles in a homogenous fluid, with electrodynamics induced by a non-uniform field. Due to the complexity of the nonuniformity, we focus on a linear electric field, which can be regarded as an approximation for many real applications. Also, a periodic electric field is discussed.

In Chapter 3, we investigate the force on a spherical particle trapped at a fluid-fluid interface, under either a normal or tangential uniform electric field. The electric problem for a single particle is solved under a toroidal coordinate system. Far-field asymptotics of the induced potential are analyzed. Electric dipping forces are evaluated for different physical parameters and contact angles. The interaction forces between two widely separated identical particles are calculated. At the leading order in separation there is a dipole-dipole interaction similar to the result in a homogeneous fluid.

In Chapter 4, the dynamics of particles on the interface of a liquid drop is discussed. Here we generalize the results of chapter 2 and 3 to develop a mathematical model to determine the collective motion and assembly of colloidal spheres trapped at a drop interface in a uniform applied electric field. Our aim is to use this model to simulate the dynamics seen in recent experiments on particle covered drops [**11, 12**] and to systematically show the impact of particle concentration and field strength on the dynamics. The model presented here accounts for the electric field driven flow within the drop and suspending fluid, particle-particle electrostatic interaction, and the particle motion and rotation due to the induced flow and the applied electric field. The impact of particle concentration and electric field strength on the collective motions of the particles is investigated. We also present simulations illustrating the effect of changing particle coverage and applied field strength to the observed clustering phenomenon near the equator of the drop.

CHAPTER 2

Particle Electrodynamics in A Non-uniform Electric Field

Here we build up a mathematical model based on multipole expansion and leaky dielectric boundary conditions to investigate the electrorotation of suspended particles. In the case of an isolated sphere, we will derive the threshold for particle rotation in a linear field. In the case of a pair of spheres, we will identify the evolution equations for the multipolar moments (dipole and quadrupole) and particle positions.

2.1. Problem Formulation

2.1.1. Electrostatic Field

Consider an isolated spherical particle with permittivity ϵ_p and conductivity σ_p suspended in a homogeneous fluid with permittivity ϵ_f and conductivity σ_f. We adopt the leaky dielectric model [**26, 27**], which assumes a charge-free bulk. Accordingly, the electric potentials satisfy the Laplace equation, i.e, $\nabla^2\phi = 0$, with the electric field defined as $\mathbf{E} = -\nabla\phi$. If the applied electric field is $\mathbf{E}_\infty = -\nabla\phi_a$, the total electric potential can be written as $\phi = \phi_a + \phi_d$ and the perturbation in the electric field due to the presence of the sphere ϕ_d can be written as a multipolar expansion in r as,

$$\phi_d(\mathbf{r}) = \frac{\mathbf{r}\cdot\mathbf{P}}{|\mathbf{r}|^3} + \frac{1}{2}\frac{\mathbf{rr}:\mathbf{Q}}{|\mathbf{r}|^5} + \frac{1}{2}\frac{\mathbf{rrr}[\cdot]^3\boldsymbol{\mathcal{O}}}{|\mathbf{r}|^7} + \cdots, \qquad |\mathbf{r}| > a, \tag{2.1}$$

$$\bar{\phi}_d(\mathbf{r}) = \frac{\mathbf{r}\cdot\mathbf{P}}{a^3} + \frac{1}{2}\frac{\mathbf{rr}:\mathbf{Q}}{a^5} + \frac{1}{2}\frac{\mathbf{rrr}[\cdot]^3\boldsymbol{\mathcal{O}}}{a^7} + \cdots, \qquad |\mathbf{r}| \le a, \tag{2.2}$$

where $\mathbf{P}$, $\mathbf{Q}$ and $\boldsymbol{\mathcal{O}}$ are the dipole, quadrupole and octopole moments. a is the sphere radius. The coordinates system is centered at the sphere. The operators $\cdot$, $:$ and $[\cdot]^3$ are inner product operators of vector, tensor and third order tensor respectively. Specifically, $\mathbf{A}[\cdot]^3\mathbf{B} = \Sigma_{ijk}A_{ijk}B_{ijk}$. Variables with a bar are inside the particle while variables without a bar are outside the particle in the suspending fluid.

Hence we obtain the gradients as,

$$\begin{aligned}\nabla\phi_d(\mathbf{r}) = {}& \frac{\mathbf{P}}{|\mathbf{r}|^3} - \frac{3\mathbf{r}\cdot\mathbf{P}}{|\mathbf{r}|^5}\mathbf{r} + \frac{1}{2}(\frac{2\mathbf{Q}\cdot\mathbf{r}}{|\mathbf{r}|^5} - \frac{5\mathbf{rr}:\mathbf{Q}}{|\mathbf{r}|^7}\mathbf{r}) \\ & + \frac{1}{2}(\frac{3\boldsymbol{\mathcal{O}}:\mathbf{rr}}{|\mathbf{r}|^7} - \frac{7\boldsymbol{\mathcal{O}}[\cdot]^3\mathbf{rrr}}{|\mathbf{r}|^9}\mathbf{r}) + \cdots, \qquad |\mathbf{r}| > a,\end{aligned} \tag{2.3}$$

$$\nabla\bar{\phi}_d(\mathbf{r}) = \frac{\mathbf{P}}{a^3} + \frac{\mathbf{Q}\cdot\mathbf{r}}{a^5} + \frac{3}{2}\frac{\boldsymbol{\mathcal{O}}:\mathbf{rr}}{a^7} + \cdots, \qquad |\mathbf{r}| \le a. \tag{2.4}$$

Meanwhile, the Taylor expansion of the applied electric potential at the particle center is given by,

$$\begin{aligned}\phi_a(\mathbf{r}) = {}& \phi_a(\mathbf{0}) + \mathbf{r}\cdot\nabla\phi_a(\mathbf{0}) + \frac{1}{2}\mathbf{rr}:\nabla\nabla\phi_a(\mathbf{0}) \\ & + \frac{1}{6}\mathbf{rrr}[\cdot]^3\nabla\nabla\nabla\phi_a(\mathbf{0}) + \cdots.\end{aligned} \tag{2.5}$$

Then the gradient of potential is,

$$\nabla\phi_a(\mathbf{r}) = \nabla\phi_a(\mathbf{0}) + \nabla\nabla\phi_a(\mathbf{0})\cdot\mathbf{r} + \frac{1}{2}\nabla\nabla\nabla\phi_a(\mathbf{0}):\mathbf{rr} + \cdots. \tag{2.6}$$

Now a leaky-dielectric boundary condition is considered. The Ohmic currents from the bulk, $\mathbf{J} = \sigma\mathbf{E}$, charge the interface and give rise to induced free charge $q = \mathbf{n}\cdot[\epsilon_f\mathbf{E} - \epsilon_p\bar{\mathbf{E}}]$. Here $\bar{\mathbf{E}} = -\nabla(\phi_a + \bar{\phi}_d)$ is evaluated on the particle side of the interface. In addition to conduction, the induced charge is affected by convection due to the particle rotation

$$\frac{\partial q}{\partial t} + \mathbf{n}\cdot[\mathbf{J} - \bar{\mathbf{J}}] + \nabla_s\cdot(q\mathbf{u}_s) = 0 \quad \text{at} \quad r = a, \tag{2.7}$$

where $\mathbf{n}$ is the unit normal vector, $\nabla_s = (\mathbf{I} - \mathbf{nn}) \cdot \nabla$ and $\mathbf{u}_s$ is the velocity of a point on the particle surface. In a frame of reference translating with the particle, the surface motion is pure rotation Ω and hence $\mathbf{u}_s = \boldsymbol{\Omega} \times \mathbf{r} = \boldsymbol{\Omega} \times a\mathbf{n}$.

Using the expansion of Eq. 2.6, from the definition of the induced charge q we obtain,

$$
\begin{aligned}
q &= -\mathbf{n} \cdot [\epsilon_f(\nabla\phi_a + \nabla\phi_d) - \epsilon_p(\nabla\phi_a + \nabla\bar{\phi}_d)] \\
&= -\mathbf{r}/a \cdot [\\
&\epsilon_f(\nabla\phi_a(\mathbf{0}) + \nabla\nabla\phi_a(\mathbf{0}) \cdot \mathbf{r} + \frac{1}{2}\nabla\nabla\nabla\phi_a(\mathbf{0}) : \mathbf{rr} + \cdots \\
&+ \frac{\mathbf{P}}{|\mathbf{r}|^3} - \frac{3\mathbf{r} \cdot \mathbf{P}}{|\mathbf{r}|^5}\mathbf{r} + \frac{1}{2}(\frac{2\mathbf{Q} \cdot \mathbf{r}}{|\mathbf{r}|^5} - \frac{5\mathbf{rr} : \mathbf{Q}}{|\mathbf{r}|^7}\mathbf{r}) \\
&+ \frac{1}{2}(\frac{3\boldsymbol{\mathcal{O}} : \mathbf{rr}}{|\mathbf{r}|^7} - \frac{7\boldsymbol{\mathcal{O}}[\cdot]^3\mathbf{rrr}}{|\mathbf{r}|^9}\mathbf{r}) + \cdots) \\
&- \epsilon_p(\nabla\phi_a(\mathbf{0}) + \nabla\nabla\phi_a(\mathbf{0}) \cdot \mathbf{r} + \frac{1}{2}\nabla\nabla\nabla\phi_a(\mathbf{0}) : \mathbf{rr} + \cdots \\
&+ \frac{\mathbf{P}}{a^3} + \frac{\mathbf{Q} \cdot \mathbf{r}}{a^5} + \frac{3}{2}\frac{\boldsymbol{\mathcal{O}} : \mathbf{rr}}{a^7} + \cdots)], \\
&= (\epsilon_p - \epsilon_f)\frac{\mathbf{r} \cdot \nabla\phi_a(\mathbf{0})}{a} + (\epsilon_p - \epsilon_f)\frac{\mathbf{rr} : \nabla\nabla\phi_a(\mathbf{0})}{a} \\
&+ \frac{(\epsilon_p - \epsilon_f)}{2}\frac{\mathbf{rrr}[\cdot]^3\nabla\nabla\nabla\phi_a(\mathbf{0})}{a} + \cdots \\
&+ (2\epsilon_f + \epsilon_p)\frac{\mathbf{r} \cdot \mathbf{P}}{a^4} + (\frac{3}{2}\epsilon_f + \epsilon_p)\frac{\mathbf{rr} : \mathbf{Q}}{a^6} \\
&+ (2\epsilon_f + \frac{3}{2}\epsilon_p)\frac{\mathbf{rrr}[\cdot]^3\boldsymbol{\mathcal{O}}}{a^8} + \cdots, \qquad |\mathbf{r}| = a.
\end{aligned}
\tag{2.8}
$$

Here we truncated at cubic terms in $|\mathbf{r}|$. The higher order expansions in $|\mathbf{r}|$ can be added to the end of Eq. 2.8 by a similar calculation when needed.

Similarly, the jump of the Ohmic current is

$$\begin{aligned}
\mathbf{n}\cdot[\mathbf{J}] &= -\mathbf{n}\cdot[\sigma_f(\nabla\phi_a+\nabla\phi_d)-\sigma_p(\nabla\phi_a+\nabla\bar{\phi}_d)]\\
&= (\sigma_p-\sigma_f)\frac{\mathbf{r}\cdot\nabla\phi_a(\mathbf{0})}{a}+(\sigma_p-\sigma_f)\frac{\mathbf{rr}:\nabla\nabla\phi_a(\mathbf{0})}{a}\\
&+\frac{(\sigma_p-\sigma_f)}{2}\frac{\mathbf{rrr}[\cdot]^3\nabla\nabla\nabla\phi_a(\mathbf{0})}{a}+\cdots\\
&+(2\sigma_f+\sigma_p)\frac{\mathbf{r}\cdot\mathbf{P}}{a^4}+(\frac{3}{2}\sigma_f+\sigma_p)\frac{\mathbf{rr}:\mathbf{Q}}{a^6}\\
&+(2\epsilon_f+\frac{3}{2}\epsilon_p)\frac{\mathbf{rrr}[\cdot]^3\boldsymbol{\mathcal{O}}}{a^8}+\cdots, \qquad |\mathbf{r}|=a.
\end{aligned}\tag{2.9}$$

Substituting $\mathbf{u}_s$ into the convection term, we have

$$\begin{aligned}
\nabla_s\cdot(q\mathbf{u}_s) &= q\nabla_s\cdot(\boldsymbol{\Omega}\times\mathbf{r})+(\boldsymbol{\Omega}\times\mathbf{r})\cdot\nabla_s q\\
&= q\boldsymbol{\Omega}\cdot(\nabla_s\times\mathbf{r})+q\mathbf{r}\cdot(\nabla_s\times\boldsymbol{\Omega})+(\boldsymbol{\Omega}\times\mathbf{r})\cdot\nabla_s q\\
&= (\boldsymbol{\Omega}\times\mathbf{r})\cdot\nabla_s q.
\end{aligned}\tag{2.10}$$

The terms $\nabla_s\times\boldsymbol{\Omega}$ and $\nabla_s\times\mathbf{r}$ vanish because $\boldsymbol{\Omega}$ is spacially independent and $\mathbf{r}=a\mathbf{n}$ is curl-free.

Moreover, the convection term is calculated by the steps below,

$$\begin{aligned}
\nabla_s q = {} & (\mathbf{I} - \mathbf{nn}) \cdot \nabla \\
& [(\epsilon_p - \epsilon_f)\frac{\mathbf{r} \cdot \nabla\phi_a(\mathbf{0})}{a} + (\epsilon_p - \epsilon_f)\frac{\mathbf{rr} : \nabla\nabla\phi_a(\mathbf{0})}{a} \\
& + \frac{(\epsilon_p - \epsilon_f)}{2}\frac{\mathbf{rrr}[\cdot]^3\nabla\nabla\nabla\phi_a(\mathbf{0})}{a} + \cdots \\
& + (2\epsilon_f + \epsilon_p)\frac{\mathbf{r} \cdot \mathbf{P}}{a^4} + (\frac{3}{2}\epsilon_f + \epsilon_p)\frac{\mathbf{rr} : \mathbf{Q}}{a^6} \\
& + (2\epsilon_f + \frac{3}{2}\epsilon_p)\frac{\mathbf{rrr}[\cdot]^3\boldsymbol{\mathcal{O}}}{a^8} + \cdots] \\
& = (\mathbf{I} - \hat{\mathbf{n}}\hat{\mathbf{n}})\cdot \\
& [(\epsilon_p - \epsilon_f)\frac{\nabla\phi_a(\mathbf{0})}{a} + 2(\epsilon_p - \epsilon_f)\frac{\nabla\nabla\phi_a(\mathbf{0}) \cdot \mathbf{r}}{a} \\
& + \frac{3(\epsilon_p - \epsilon_f)}{2}\frac{\nabla\nabla\nabla\phi_a(\mathbf{0}) : \mathbf{rr}}{a} + \cdots \\
& + (2\epsilon_f + \epsilon_p)\frac{\mathbf{P}}{a^4} + (3\epsilon_f + 2\epsilon_p)\frac{\mathbf{Q} \cdot \mathbf{r}}{a^6} \\
& + (6\epsilon_f + \frac{9}{2}\epsilon_p)\frac{\boldsymbol{\mathcal{O}} : \mathbf{rr}}{a^8} + \cdots].
\end{aligned} \tag{2.11}$$

Thus,

$$
\begin{aligned}
(\mathbf{\Omega}\times\mathbf{r})\cdot\nabla_s q =&(\mathbf{\Omega}\times\mathbf{r})\cdot\{(\mathbf{I}-\mathbf{nn})\cdot\\
&[(\epsilon_p-\epsilon_f)\frac{\nabla\phi_a(\mathbf{0})}{a}+2(\epsilon_p-\epsilon_f)\frac{\nabla\nabla\phi_a(\mathbf{0})\cdot\mathbf{r}}{a}\\
&+\frac{3(\epsilon_p-\epsilon_f)}{2}\frac{\nabla\nabla\nabla\phi_a(\mathbf{0}):\mathbf{rr}}{a}+\cdots\\
&+(2\epsilon_f+\epsilon_p)\frac{\mathbf{P}}{a^4}+(3\epsilon_f+2\epsilon_p)\frac{\mathbf{Q}\cdot\mathbf{r}}{a^6}\\
&+(6\epsilon_f+\frac{9}{2}\epsilon_p)\frac{\boldsymbol{\mathcal{O}}:\mathbf{rr}}{a^8}+\cdots]\}\\
=&-\mathbf{r}\cdot\{\mathbf{\Omega}\times[(\epsilon_p-\epsilon_f)\frac{\nabla\phi_a(\mathbf{0})}{a}+(2\epsilon_f+\epsilon_p)\frac{\mathbf{P}}{a^4}]\}\\
&-\mathbf{rr}:\{\mathbf{\Omega}\times[2(\epsilon_p-\epsilon_f)\frac{\nabla\nabla\phi_a(\mathbf{0})}{a}+(3\epsilon_f+2\epsilon_p)\frac{\mathbf{Q}}{a^6}]\}\\
&-\mathbf{rrr}[\cdot]^3\{\mathbf{\Omega}\times[\frac{3(\epsilon_p-\epsilon_f)}{2}\frac{\nabla\nabla\nabla\phi_a(\mathbf{0})}{a}+(6\epsilon_f+\frac{9}{2}\epsilon_p)\frac{\boldsymbol{\mathcal{O}}}{a^8}+\cdots]\}\\
&-\cdots .
\end{aligned}
\tag{2.12}
$$

Here $[\mathbf{\Omega}\times\mathbf{P}]_i=\epsilon_{ijk}\Omega_j P_k$, $[\mathbf{\Omega}\times\mathbf{Q}]_{ij}=\epsilon_{ikl}\Omega_k Q_{jl}$, $[\mathbf{\Omega}\times\boldsymbol{\mathcal{O}}]_{ijk}=\epsilon_{imn}\Omega_m\mathcal{O}_{jkn}$, following the Einstein notation. Contributions from higher order moments can be added in the same way above.

Substituting back into Eq. 2.7, the equation has contributions in different order of multipole products with $\mathbf{r}$. As we mentioned, $\mathbf{r}$ is a position vector at any point on the particle surface. It should be noted here that, $\mathbf{\Omega}$ will be later determined by solving the particle mobility problem. Using the symmetries of the multipole moments, Eq. 2.12 is separable at each order of $\mathbf{r}$ (see Appendix A). Independent equations for each multipole moment can be derived. Here we obtain the equations for the dipole moment $\mathbf{P}$ and the quadrupole moment $\mathbf{Q}$,

$$\begin{aligned}&\frac{d}{dt}[(2\epsilon_f+\epsilon_p)\frac{\mathbf{r}\cdot\mathbf{P}}{a^4}]+(2\sigma_f+\sigma_p)\frac{\mathbf{r}\cdot\mathbf{P}}{a^4}+(\sigma_p-\sigma_f)\frac{\mathbf{r}\cdot\nabla\phi_a(0)}{a}\\&-\mathbf{r}\cdot\{\boldsymbol{\Omega}\times[(\epsilon_p-\epsilon_f)\frac{\nabla\phi_a(0)}{a}+(2\epsilon_f+\epsilon_p)\frac{\mathbf{P}}{a^4}]\}=0,\end{aligned}\tag{2.13}$$

$$\begin{aligned}&\frac{d}{dt}[(\frac{3}{2}\epsilon_f+\epsilon_p)\frac{\mathbf{rr}:\mathbf{Q}}{a^6}]+(\frac{3}{2}\sigma_f+\sigma_p)\frac{\mathbf{rr}:\mathbf{Q}}{a^6}\\&+(\sigma_p-\sigma_f)\frac{\mathbf{rr}:\nabla\nabla\phi_a(0)}{a}-\mathbf{rr}:\{\boldsymbol{\Omega}\times[2(\epsilon_p-\epsilon_f)\frac{\nabla\nabla\phi_a(0)}{a}\\&+(3\epsilon_f+2\epsilon_p)\frac{\mathbf{Q}}{a^6}]\}=0.\end{aligned}\tag{2.14}$$

Eq. 2.13 reduces to

$$\frac{d\mathbf{P}}{dt}=\boldsymbol{\Omega}\times[\mathbf{P}+a^3\epsilon_{cm}\nabla\phi_a(0)]-\frac{1}{\tau_{mw}}[\mathbf{P}+a^3\sigma_{cm}\nabla\phi_a(0)],\tag{2.15}$$

where

$$\epsilon_{cm}=\frac{\epsilon_p-\epsilon_f}{\epsilon_p+2\epsilon_f},\quad \sigma_{cm}=\frac{\sigma_p-\sigma_f}{\sigma_p+2\sigma_f},\quad \tau_{mw}=\frac{\epsilon_p+2\epsilon_f}{\sigma_p+2\sigma_f},$$

Eq. 2.14 reduces to

$$\begin{aligned}\frac{d\mathbf{Q}}{dt}=&\{\boldsymbol{\Omega}\times[\mathbf{Q}+2a^5\epsilon'_{cm}\nabla\nabla\phi_a(0)]\}\\&+\{\boldsymbol{\Omega}\times[\mathbf{Q}+2a^5\epsilon'_{cm}\nabla\nabla\phi_a(0)]\}^{\mathsf{T}}\\&-\frac{1}{\tau'_{mw}}[\mathbf{Q}+2a^5\sigma'_{cm}\nabla\nabla\phi_a(0)],\end{aligned}\tag{2.16}$$

where

$$\epsilon'_{cm}=\frac{\epsilon_p-\epsilon_f}{2\epsilon_p+3\epsilon_f},\quad \sigma'_{cm}=\frac{\sigma_p-\sigma_f}{2\sigma_p+3\sigma_f},\quad \tau'_{mw}=\frac{2\epsilon_p+3\epsilon_f}{2\sigma_p+3\sigma_f}.$$

Here ϵ_{cm}, ϵ'_{cm}, σ_{cm} and σ'_{cm} are referred to as the Clausius-Mossotti factors and τ_{mw}, τ'_{mw} are the Maxwell-Wagner relaxation times [**51**]. Note we always assume $\mathbf{Q}$ is symmetric to satisfy the original Laplace equation.

It is interesting to note that

$$\mathbf{M} = \mathbf{M^T} \quad \Rightarrow \quad tr(\mathbf{\Omega} \times \mathbf{M}) = 0 \quad \forall \text{ vector } \mathbf{\Omega}, \text{ and } \mathbf{M} \in \boldsymbol{\mathcal{R}}_{3\times 3}, \tag{2.17}$$

see Appendix A.

Here even though $\mathbf{\Omega} \times \mathbf{Q}$ doesn't have to be symmetric at all time, given a traceless and symmetric $\mathbf{Q}$ initially, Eq. 2.16 preserves symmetry and zero trace. In the absence of rotation, the dipole and quadrupole moments relax toward the steady state with two slightly different Maxwell-Wagner times τ_{mw} and τ'_{mw}, which depend on material electric properties. The evolution of higher order moments in the expansion Eq. 2.3 can be obtained in a similar way. However, in a linear applied electric field (i.e., a spatially slowly varying external electric field) these contributions come at a higher order and are negligible in the far-field approximation.

The force and torque on the particle are calculated by the effective multipole moment method [**50, 51**], which at the order of our approximation gives

$$\begin{aligned} \mathbf{F}^{el} &= -4\pi\epsilon_f(\mathbf{P} \cdot \nabla\nabla\phi_a(\mathbf{0}) + \frac{1}{6}\mathbf{Q} : \nabla\nabla\nabla\phi_a(\mathbf{0})), \\ \mathbf{T}^{el} &= -4\pi\epsilon_f(\mathbf{P} \times \nabla\phi_a(\mathbf{0}) + (\mathbf{Q} \cdot \nabla) \times \nabla\phi_a(\mathbf{0})). \end{aligned} \tag{2.18}$$

Note that the above expressions are strictly valid for an isolated sphere in a linear applied field.

2.1.2. Single Particle Motion

For small particles, inertia is negligible. Accordingly, the translational velocity, $\mathbf{U}$, and rotational rate, $\boldsymbol{\Omega}$, of a sphere is determined by the balance of electrostatic force and Stokes drag,

$$\begin{aligned}\mathbf{F}^{el} &= 6\pi\eta_f a(-\mathbf{u}^{\infty} - \frac{a^2}{6}\nabla^2\mathbf{u}^{\infty} + \mathbf{U}),\\ \mathbf{T}^{el} &= 8\pi\eta_f a^3(-\boldsymbol{\Omega}^{\infty} + \boldsymbol{\Omega}),\end{aligned} \tag{2.19}$$

where η_f is the viscosity of the suspending fluid, and $\mathbf{u}^{\infty}$ (and $-\boldsymbol{\Omega}^{\infty}$) is a background flow (either applied or generated by the motion of other spheres, if present) evaluated at the sphere center. In our study, the background flow is zero for an isolated particle. In the case of multiple particles, the background flow is the flow induced by the motion of the rest of the particles.

2.2. An Isolated Sphere in A Linear Electric Field

2.2.1. Threshold for Electrorotation

The classic Quincke electrorotation considers an isolated sphere suspended in a homogeneous fluid and exposed to uniform DC electric field $\mathbf{E}_{\infty}$. The threshold field for electrorotation is given by [**47, 48**],

$$|\mathbf{E}| > E_c = \sqrt{\frac{2\eta_f}{\epsilon_f \tau_{mw}(\epsilon_{cm} - \sigma_{cm})}}, \tag{2.20}$$

and the rotation rate is

$$|\boldsymbol{\Omega}| = \pm\frac{1}{\tau_{mw}}\sqrt{\left(\frac{|\mathbf{E}_{\infty}|}{E_c}\right)^2 - 1}. \tag{2.21}$$

Eq. 2.20 shows that electro-rotation can occur only if $\epsilon_{cm} > \sigma_{cm}$.

In an non-uniform field, this criterion can be generalized. Eq. 2.15 and Eq. 2.16 show that the steady dipole and symmetric quadrupole moments satisfy,

$$\begin{aligned} &\mathbf{\Omega} \times [\mathbf{P} + a^3\epsilon_{cm}\nabla\phi_a] - \frac{1}{\tau_{mw}}[\mathbf{P} + a^3\sigma_{cm}\nabla\phi_a] = \mathbf{0} \\ &\mathbf{\Omega} \times [\mathbf{Q} + 2a^5\epsilon'_{cm}\nabla\nabla\phi_a] - \frac{1}{2\tau'_{mw}}[\mathbf{Q} + 2a^5\sigma'_{cm}\nabla\nabla\phi_a] = \mathbf{0}. \end{aligned} \tag{2.22}$$

By taking inner and outer product of Eq. 2.22 with $\mathbf{\Omega}$, we obtain $\mathbf{P}$ and $\mathbf{Q}$ in terms of $\mathbf{\Omega}$,

$$\begin{aligned} \mathbf{P} &= A_1[\mathbf{\Omega} \times \nabla\phi_a + \tau_{mw}(\mathbf{\Omega}\cdot\nabla\phi_a)\mathbf{\Omega}] - A_2\nabla\phi_a \\ \mathbf{Q} &= A_3[\mathbf{\Omega} \times \nabla\nabla\phi_a + 2\tau'_{mw}(\mathbf{\Omega}\cdot\nabla\nabla\phi_a)\mathbf{\Omega}] - A_4\nabla\nabla\phi_a, \end{aligned} \tag{2.23}$$

where the coefficients are,

$$\begin{aligned} A_1 &= \frac{a^3\tau_{mw}(\epsilon_{cm} - \sigma_{cm})}{1 + \Omega^2\tau^2_{mw}}, A_2 = a^3[\epsilon_{cm} - \frac{\epsilon_{cm} - \sigma_{cm}}{1 + \Omega^2\tau^2_{mw}}], \\ A_3 &= \frac{2a^5\tau'_{mw}(\epsilon'_{cm} - \sigma'_{cm})}{1 + 4\Omega^2\tau'^2_{mw}}, A_4 = 2a^5[\epsilon'_{cm} - \frac{\epsilon'_{cm} - \sigma'_{cm}}{1 + 4\Omega^2\tau'^2_{mw}}]. \end{aligned} \tag{2.24}$$

Substituting Eq. 2.23 back into the torque balance equation Eq. 2.19, and taking the inner product with $\mathbf{\Omega}$, we find an equation for $\mathbf{\Omega}$

$$\begin{aligned} 2\eta_f|\mathbf{\Omega}|^2 = \epsilon_f &\frac{\tau_{mw}(\epsilon_{cm} - \sigma_{cm})}{1 + |\mathbf{\Omega}|^2\tau^2_{mw}}[-(\mathbf{\Omega}\cdot\mathbf{E}_\infty)^2 + |\mathbf{\Omega}|^2|\mathbf{E}_\infty|^2] \\ &+ \epsilon_f\frac{4\tau'_{mw}a^2(\epsilon'_{cm} - \sigma'_{cm})}{1 + 4|\mathbf{\Omega}|^2\tau'^2_{mw}}[-|\mathbf{\Omega}\cdot\nabla\mathbf{E}_\infty|^2 + |\mathbf{\Omega}|^2\|\nabla\mathbf{E}_\infty\|^2]. \end{aligned} \tag{2.25}$$

Here we denote $\|\mathbf{T}\|^2 = \sum T^2_{ij}$. Unlike the uniform field case, in a non-uniform field $\mathbf{\Omega}\cdot\mathbf{E}_\infty$ in general is nonzero.

Eq. 2.25 yields a trivial solution,

$$\mathbf{\Omega} = 0. \tag{2.26}$$

A nontrivial solution of Eq. 2.25 requires that

$$\begin{aligned}2\eta_f &= \epsilon_f \frac{\tau_{mw}(\epsilon_{cm}-\sigma_{cm})}{1+|\mathbf{\Omega}|^2\tau_{mw}^2}(|\mathbf{E}_\infty|^2 - \frac{|\mathbf{\Omega}\cdot\mathbf{E}_\infty|^2}{|\mathbf{\Omega}|^2}) \\ &+ \epsilon_f \frac{4\tau'_{mw}a^2(\epsilon'_{cm}-\sigma'_{cm})}{1+4|\mathbf{\Omega}|^2\tau'^2_{mw}}(\|\nabla\mathbf{E}_\infty\|^2 - \frac{|\mathbf{\Omega}\cdot\nabla\mathbf{E}_\infty|^2}{|\mathbf{\Omega}|^2}). \end{aligned} \tag{2.27}$$

In particular, when $\epsilon_p/\sigma_p \geq \epsilon_f/\sigma_f$, it is easy to show that $\epsilon_{cm}-\sigma_{cm}$ and $\epsilon'_{cm}-\sigma'_{cm}$ are both non-negative. Although this equation is difficult to be solved explicitly for Ω, we can identify a necessary condition for the existence of a nontrivial solution.

In particular, when $\epsilon_p/\sigma_p \geq \epsilon_f/\sigma_f$, it is easy to show that $\epsilon_{cm}-\sigma_{cm}$ and $\epsilon'_{cm}-\sigma'_{cm}$ are both non-negative. Then Eq. 2.27 leads to

$$2\eta_f \leq \epsilon_f\tau_{mw}(\epsilon_{cm}-\sigma_{cm})|\mathbf{E}_\infty|^2 + 4\epsilon_f\tau'_{mw}a^2(\epsilon'_{cm}-\sigma'_{cm})\|\nabla\mathbf{E}_\infty\|^2. \tag{2.28}$$

As an example of a nonuniform electric field let us consider

$$\mathbf{E}_\infty = \alpha(x\mathbf{i} - z\mathbf{k}), \tag{2.29}$$

which can be experimentally generated by a hyperbolic cylinder electrodes; here $\mathbf{i}$ and $\mathbf{k}$ are the unit vectors in the x and z direction. The parameter α ia a measure of the field gradient. It should be noted that if a constant field were added to Eq. 2.29 for nonzero α, the effect would simply be a translation of the coordinate system, and hence this term is not included here.

From Eq. 2.22, Eq. 2.23, Eq. 2.27 and Eq. 2.29, we obtain for a particle centered at $x = 0$ and $z = 0$, a steady rotation around the y axis, with the magnitude

$$|\mathbf{\Omega}| = \sqrt{\frac{\epsilon_f(\epsilon'_{cm}-\sigma'_{cm})a^2\alpha^2}{\eta_f\tau'_{mw}} - \frac{1}{4\tau'^2_{mw}}}. \tag{2.30}$$

Introduce $G = a\alpha/E_c$, this is a dimensionless measure of the field gradient strength over the particle. With this definition, we can identify a critical value of G, G^*, in Eq. 2.30 which generates a nonzero rotation predicted when $|\mathbf{\Omega}| = 0$,

$$G^* = \frac{1}{4}\sqrt{2\frac{\tau_{mw}(\epsilon_{cm} - \sigma_{cm})}{\tau'_{mw}(\epsilon'_{cm} - \sigma'_{cm})}}. \tag{2.31}$$

This is the threshold for electorotation in a linear field in the whole plane.

2.2.2. Dynamics and Particle Trajectories

Here we consider particle motion in the nonuniform electric field Eq. 2.29. Since the applied field direction is parallel to the x-z plane, particle motion is expected to be confined to the x-z plane. This special case will allow us to illustrate the effect of non-uniformities on the particle dynamics. Note that although the evolution equations Eq. 2.15, Eq. 2.16 and Eq. 2.19 are derived for a slowly varying electric field, they are exact for the special case Eq. 2.29.

Henceforth we non-dimensionalize all variables by the drop radius a, electrohydrodynamic time $t_{ehd} = \eta_f/\epsilon_f E_c^2$ and electric field threshold for Quincke rotation E_c given by Eq. 2.20. All dimensionless variables are denoted by tilde. The dimensionless Eq. 2.15 and Eq. 2.16 are

$$\begin{aligned}\frac{d\widetilde{\mathbf{P}}}{d\tilde{t}} =& \widetilde{\mathbf{\Omega}} \times [\widetilde{\mathbf{P}} - \epsilon_{cm} G(\hat{x}\mathbf{i} - \hat{z}\mathbf{k})] \\ & - \frac{1}{D}[\widetilde{\mathbf{P}} - \sigma_{cm} G(\hat{x}\mathbf{i} - \hat{z}\mathbf{k})],\end{aligned} \tag{2.32}$$

$$\begin{aligned}\frac{d\widetilde{\mathbf{Q}}}{d\tilde{t}} =& \widetilde{\mathbf{\Omega}} \times [\widetilde{\mathbf{Q}} - 2\epsilon'_{cm}\widetilde{\mathcal{G}}] \\ &+ [\widetilde{\mathbf{\Omega}} \times [\widetilde{\mathbf{Q}} - 2\epsilon'_{cm}\widetilde{\mathcal{G}}]]^{\mathsf{T}} \\ &- \frac{1}{D'}[\widetilde{\mathbf{Q}} - 2\sigma'_{cm}\widetilde{\mathcal{G}}],\end{aligned} \tag{2.33}$$

where

$$D = \frac{\tau_{mw}}{t_{ehd}} = \frac{\epsilon_f E_c^2 \tau_{mw}}{\eta_f}, D' = \frac{\tau'_{mw}}{t_{ehd}} = D\frac{\tau'_{mw}}{\tau_{mw}},$$

and

$$\widetilde{\mathcal{G}} = G \begin{pmatrix} 1 & 0 & 0 \\ 0 & 0 & 0 \\ 0 & 0 & -1 \end{pmatrix}. \tag{2.34}$$

Note that the applied field in Eq. 2.15 and Eq. 2.16 are evaluated at the particle center ($\hat{x} = \hat{y} = 0$), but for a moving particle it should be evaluated at the current particle location. Hence there is a spacial dependence in the electric field in Eq. 2.32.

The dimensionless Eq. 2.19 yields for the particle translation and rotation

$$\begin{aligned}\tilde{\mathbf{U}} &= \frac{2}{3}\widetilde{\mathbf{P}} \cdot \widetilde{\mathcal{G}}, \\ \widetilde{\mathbf{\Omega}} &= \frac{1}{2}[\widetilde{\mathbf{P}} \times G(\tilde{x}\mathbf{i} - \tilde{z}\mathbf{k}) + \widetilde{\mathbf{Q}} \times \widetilde{\mathcal{G}}].\end{aligned} \tag{2.35}$$

For the numerical calculations, we chose the experimental system of Ref. [**44**]: $\epsilon_{cm} = -0.1092$, $\epsilon'_{cm} = -0.0670$, $\sigma_{cm} = -0.5$ and $\sigma'_{cm} = -0.3333$, $E_c = 827.3V/mm$, $\tau_{mw} = 2.94\text{ms}$, $\tau'_{mw} = 3.20\text{ms}$, $D = 5.1520$, $D' = 5.6054$. From Eq. 2.31 we find that to guarantee nonzero electrorotation in the whole plane we need $G \geq G^* = 0.5787$.

Figure 2.1 shows a typical particle trajectory when $G = 0.4000$. The particle undergoes negative dielectrophoresis (DEP) and moves towards the minimum field location. The Quincke rotation and continuous changing DEP force make the trajectory non-straight

The circle in fig. 2.1 indicates the region given by Eq. 2.28. Within this region, the particle does not undergo Quincke rotation. The evolution of particle rotation rate and the components of the dipole and quadrupole moments is shown in fig. 2.2. Upon particle release, the magnitude of its rotation rate increases. Position p1 is a turning point after which the rotation magnitude starts to decrease. Positions p2 and p3 are two intermediate points before particle enters the 'non-Quincke' zone. Position p4 is when the particle arrives at the center axis, where rotation and all multiple moments except the diagonal elements of $\mathbf{Q}$ decay to zero.

Increasing of the field gradient strength shrinks the 'non-Quincke' zone and when $G \geq G^*$ the electro-rotation occurs everywhere in the space. A single particle will eventually stay steady at the equilibrium position with a non-zero rotation rate.

In even stronger fields, particle dynamics becomes more complex. Fig. 2.3 shows particle steady state changing from a stable point (see fig. 2.3(a)), to circular orbit (see fig. 2.3(b)) and finally bounded elliptic orbit (see fig. 2.3(c)) as G increases.

The longtime stationary trajectory can be characterized by the short r_a and the long r_b axes of the elliptical orbit. Fig. 2.4 shows the dependence of r_a and r_b on field strength. Region 1 (no rotation) and 2 indicate steady position in the physical plane ($r_a = r_b = 0$). In region 2, the particle undergoes electro-rotation, however there is no off-center particle motion in this steady state solution(see fig 2.3(a)). The narrow region 3 corresponds to a different scenario(see fig. 2.3(b)). In this region, the origin is no longer a steady position. The particle trajectory converges to a circle centered at the origin. The radius of this circle increases with G. Region 4 shows a transition from the circular trajectory to rotating elliptical trajectories as in fig. 2.3(c). It is interesting to notice that in this

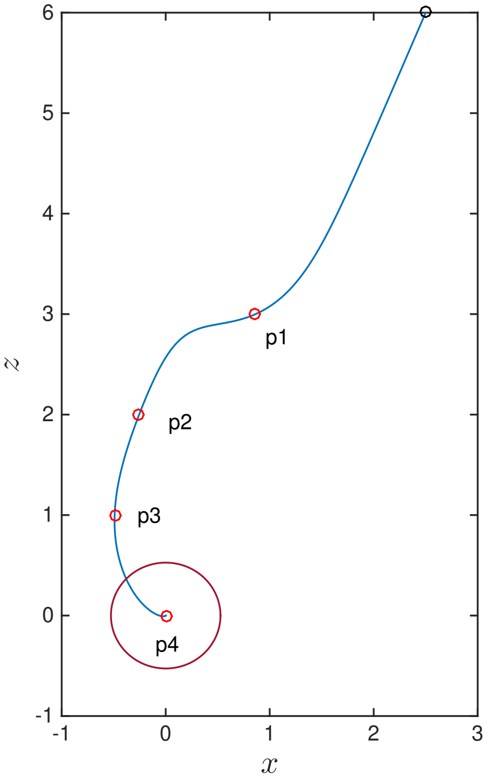

Figure 2.1. One particle trajectory starting at $x = 2.5$, $z = 6.0$. Initial perturbations at the magnitude of $O(10^{-4})$ are randomly generated. The red circle indicates the non-Quincke region satisfying Eq. 2.28. The markers p1 to p4 indicate four positions when z first hits the value of $0.0, 1.0, 2.0, 3.0$. $G = 0.4000$. The particle does not rotate in the equilibrium state.

region, the average radius stays almost unchanged, but the deformation increases with G. Region 5 indicates a simultaneous increase of the deformation and the average orbit radius, while the orbit retains elliptical shape.

2.3. Multi-particle System in Linear Electric Fields

Here we extend Eq. 2.15, Eq. 2.16 and Eq. 2.19 to many particles systems. For convenience, we revert to dimensional variables.

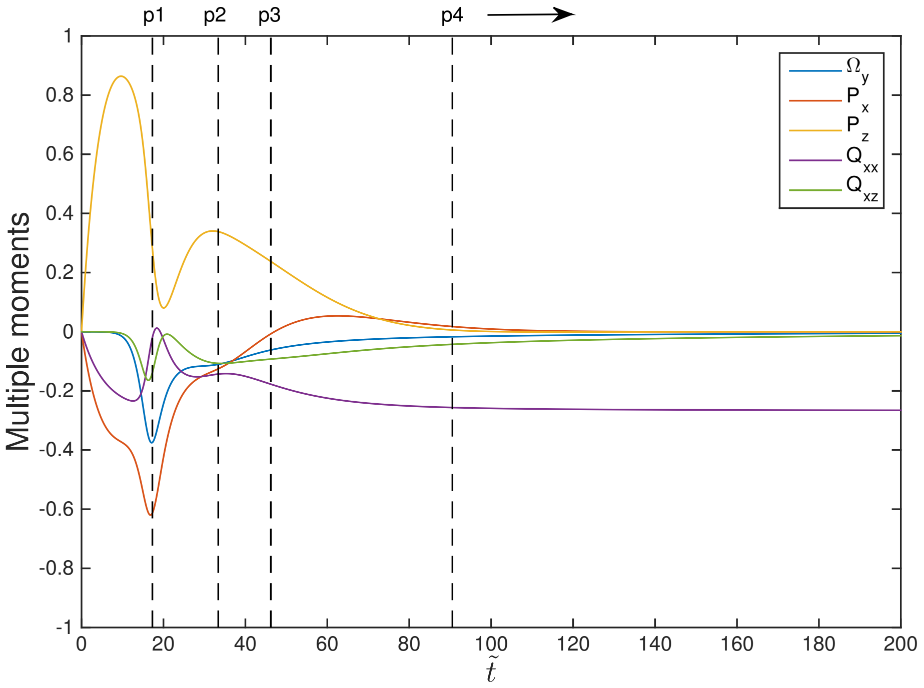

Figure 2.2. The evolution of corresponding multiple moments and rotation rate to the single particle dynamic in Fig 2.1.

2.3.1. General Formulation

Here we generalize the model to describe the dynamics of multiple particles.

The grand mobility formation for particle motion follows as,

$$\begin{pmatrix} \mathbf{u}^{\infty} - \mathbf{u} \\ \\ \mathbf{\Omega}^{\infty} - \mathbf{\Omega} \end{pmatrix} = \mathbf{M} \cdot \begin{pmatrix} \eta_{\mathbf{f}}^{-\mathbf{1}}\mathbf{F} \\ \\ \eta_{\mathbf{f}}^{-\mathbf{1}}\mathbf{T} \end{pmatrix}. \tag{2.36}$$

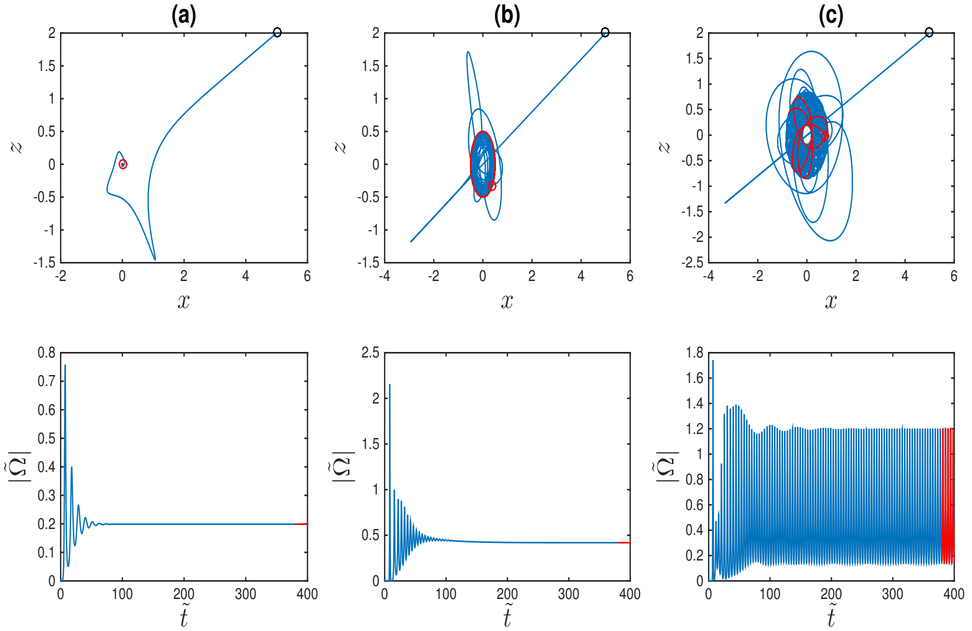

Figure 2.3. Particle trajectories in different field gradient strength. Initial position $x = 5.0$, $z = 2.0$ and a random initial polarization perturbation at $O(10^{-4})$. $D = 5.1520$, $D' = 5.6054$. (a). $G = 1.0$, (b). $G = 2.3$, (c). $G = 3.0$. The final time interval $\tilde{t} = 380 - 400$ is indicated by red color.

For example of a two-particle system, the mobility equations of particle 1 relates the hydrodynamic forces and torques to the particle motion as,

$$\begin{aligned} \mathbf{u}^{\infty} - \mathbf{u}_1 &= \eta_f^{-1}(\mathbf{a_{11}F_1^H} + \mathbf{a_{12}F_2^H} + \tilde{\mathbf{b}}_{\mathbf{11}}\mathbf{T_1^H} + \tilde{\mathbf{b}}_{\mathbf{12}}\mathbf{T_2^H}) \\ \boldsymbol{\Omega}^{\infty} - \boldsymbol{\Omega}_1 &= \eta_f^{-1}(\mathbf{b_{11}F_1^H} + \mathbf{b_{12}F_2^H} + \mathbf{c_{11}T_1^H} + \mathbf{c_{12}T_2^H}), \end{aligned} \tag{2.37}$$

where $\mathbf{T}_i^H$ and $\mathbf{F}_i^H$ are the torques and forces exerted by the fluid on particle i (here $i = 1, 2$). η_f is the viscosity of the external fluid. The coefficient tensors $\mathbf{a}$, $\mathbf{b}$, $\mathbf{c}$ are called mobility functions which are relative to particle separation.

Note that the full grand mobility matrix involves the strain if there is an applied shear flow. The model we present here is directly extendible by adding the applied strain contribution.

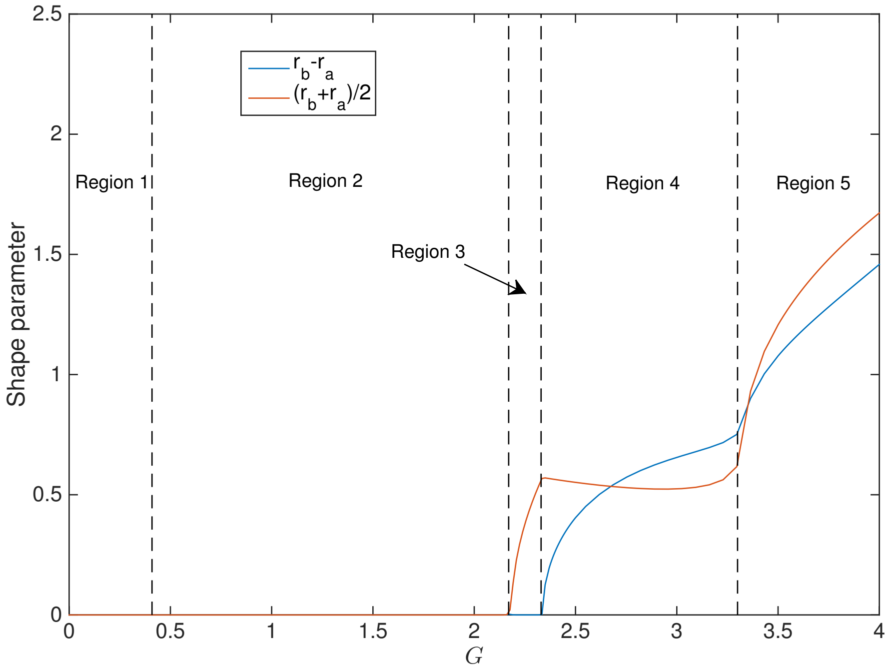

Figure 2.4. Stationary trajectory shape vs G. r_a and r_b are the short and long radius of the steady orbit. When no steady orbit is observed, r_a and r_b are the minimum and maximum distance to the origin in a chosen time frame. $D' = 5.6054$, $\epsilon'_{cm} = -0.0670$, $\sigma'_{cm} = -0.3333$.

Denote the position vector of an arbitrary particle i as $\mathbf{r}_i$ and $\mathbf{R}_{12} = \mathbf{r}_2 - \mathbf{r}_1$.

The components of the coefficient tensors in Eq. 2.37 are expanded as [**52**],

$$
\begin{aligned}
(\mathbf{a}_{11})_{ij} &= x^a_{11} d_i d_j + y^a_{11}(\delta_{ij} - d_i d_j), \\
(\mathbf{a}_{12})_{ij} &= x^a_{12} d_i d_j + y^a_{12}(\delta_{ij} - d_i d_j), \\
(\mathbf{b}_{11})_{ij} &= y^b_{11} \epsilon_{ijk} d_k, \\
(\mathbf{b}_{12})_{ij} &= y^b_{12} \epsilon_{ijk} d_k, \\
(\tilde{\mathbf{b}}_{11})_{ij} &= (\mathbf{b}_{11})_{ji}, \\
(\tilde{\mathbf{b}}_{12})_{ij} &= (\mathbf{b}_{21})_{ji} = -(\mathbf{b}_{12})_{ji}, \\
(\mathbf{c}_{11})_{ij} &= x^c_{11} d_i d_j + y^c_{11}(\delta_{ij} - d_i d_j), \\
(\mathbf{c}_{12})_{ij} &= x^c_{12} d_i d_j + y^c_{12}(\delta_{ij} - d_i d_j),
\end{aligned} \tag{2.38}
$$

where the normalized separation vector $\mathbf{d} = \mathbf{R}_{12}/|\mathbf{R}_{12}|$.

In a far-field approximation, assuming $\frac{a}{|\mathbf{R}_{ij}|} \sim \gamma \ll 1$ $(\forall\ i, j)$. Denoting $R = |\mathbf{R}_{ij}|$, the mobility functions are,

$$
\begin{aligned}
x^a_{11} &= \frac{1}{6\pi a}(1 + \frac{15a^4}{4R^4} + O(\gamma^9)), \\
y^a_{11} &= \frac{1}{6\pi a}(1 + O(\gamma^6)), \\
x^a_{12} &= \frac{1}{6\pi a}(\frac{3a}{2R} - \frac{a^3}{R^3} + O(\gamma^7)), \\
y^a_{12} &= \frac{1}{6\pi a}(\frac{3a}{4R} + \frac{a^3}{2R^3} + O(\gamma^{11})), \\
y^b_{11} &= O(\gamma^7), \\
y^b_{12} &= \frac{1}{4\pi a^2}(-\frac{a^2}{2R^2} + O(\gamma^{10})), \\
x^c_{11} &= \frac{1}{8\pi a^3}(1 + O(\gamma^8)), \\
x^c_{12} &= \frac{1}{8\pi a^3}(-\frac{a^3}{R^3} + O(\gamma^{11})), \\
y^c_{11} &= \frac{1}{8\pi a^3}(1 + O(\gamma^6)), \\
y^c_{12} &= \frac{1}{8\pi a^3}(-\frac{a^3}{2R^3} + O(\gamma^9)),
\end{aligned}
\tag{2.39}
$$

with the indicated leading order errors.

With a similar derivation, for an arbitrary number of particles, the exact equations for particle motion will be (denoting $R_{ij} = |\mathbf{R}_{ij}|$),

$$
\begin{aligned}
\eta_f(\mathbf{u}^{\infty} - \mathbf{u}_i) = {} & \frac{\mathbf{F}_i^H}{6\pi a} + \sum_{j\neq i}[\frac{5a^3}{8\pi R_{ij}^4}(\mathbf{F}_i^H \cdot \widehat{\mathbf{R}}_{ij})\widehat{\mathbf{R}}_{ij} - \frac{\mathbf{T}_j^H \times \widehat{\mathbf{R}}_{ij}}{8\pi R_{ij}^2} \\
& + \frac{1}{8\pi}(\frac{1}{R_{ij}} + \frac{2a^2}{3R_{ij}^3})\mathbf{F}_j^H \\
& + \frac{1}{8\pi}(\frac{1}{R_{ij}} - \frac{2a^2}{R_{ij}^3})(\mathbf{F}_j^H \cdot \widehat{\mathbf{R}}_{ij})\widehat{\mathbf{R}}_{ij}] + O(\gamma^5), \\
\eta_f(\mathbf{\Omega}^{\infty} - \mathbf{\Omega}_i) = {} & \frac{\mathbf{T}_i^H}{8\pi a^3} + \sum_{j\neq i}[-\frac{\mathbf{T}_j^H}{16\pi R_{ij}^3} - \frac{3}{16\pi R_{ij}^3}(\mathbf{T}_j^H \cdot \widehat{\mathbf{R}}_{ij})\widehat{\mathbf{R}}_{ij} \\
& - \frac{\mathbf{F}_j^H \times \widehat{\mathbf{R}}_{ij}}{8\pi R_{ij}^2}] + O(\gamma^6).
\end{aligned}
\tag{2.40}
$$

Assume particles are forced balanced and no inertia effect is considered. The hydrodynamic force $\mathbf{F}^H$ imposed by the fluid on particles should be balanced by the non-hydrodynamic interactions. i.e.

$$
\mathbf{F}^H = -\mathbf{F}^{el} - \mathbf{F}^{rep}. \tag{2.41}
$$

For a given linear electric field, we can get calculate the force and torque exactly as,

$$
\begin{aligned}
\mathbf{F}_i^{el} &= -4\pi\epsilon_f(\mathbf{P}_i \cdot \nabla\nabla\phi_e(\mathbf{r_i}) + \frac{1}{6}\mathbf{Q}_i : \nabla\nabla\nabla\phi_e(\mathbf{r_i})), \\
\mathbf{T}_i^{el} &= -4\pi\epsilon_f(\mathbf{P}_i \times \nabla\phi_e(\mathbf{r_i}) + (\mathbf{Q}_i \cdot \nabla) \times \nabla\phi_e(\mathbf{r_i})),
\end{aligned}
\tag{2.42}
$$

where $\phi_e = \phi_a + \sum \phi_d$ is the total external electric potential which contains the applied potential and the disturbance potentials.

Substitute the exact ϕ_e into the equation, up to the order of $O(\gamma^4)$, we obtain three terms of the force:

$$\begin{aligned}
\mathbf{F}_i^{d1} =& 4\pi\epsilon_f \mathbf{P}_i \cdot \nabla\nabla\phi_a(\mathbf{r_i}),\\
\mathbf{F}_i^{d2} =& -\sum_{j\neq i} \frac{12\pi\epsilon_f}{R_{ij}^4}[(\mathbf{P}_i \cdot \widehat{\mathbf{R}}_{ij})\mathbf{P}_j + (\mathbf{P}_j \cdot \widehat{\mathbf{R}}_{ij})\mathbf{P}_i \\
& + (\mathbf{P}_i \cdot \mathbf{P}_j)\widehat{\mathbf{R}}_{ij} - 5(\mathbf{P}_j \cdot \widehat{\mathbf{R}}_{ij})(\mathbf{P}_i \cdot \widehat{\mathbf{R}}_{ij})\widehat{\mathbf{R}}_{ij}],\\
\mathbf{F}_i^{d3} =& \frac{2\pi\epsilon_f}{3}\mathbf{Q}_i : \nabla\nabla\nabla\phi_a(\mathbf{r_i}).
\end{aligned} \tag{2.43}$$

And the leading error is from truncating the quadrupole contribution in the disturbance potential,

$$\mathbf{F}_i^{el} = \mathbf{F}_i^{d1} + \mathbf{F}_i^{d2} + \mathbf{F}_i^{d3} + O(\gamma^5). \tag{2.44}$$

Then similarly when we deal with the hydrodynamic torque T^H, we assume it is instantly balanced by the electric torque, i.e.

$$\mathbf{T}^H = -\mathbf{T}^{el}. \tag{2.45}$$

Then also from Eq. 2.42,

$$\mathbf{T}_i^{el} = \mathbf{T}_i^{d1} + \mathbf{T}_i^{d2} + \mathbf{T}_i^{d3} + \mathbf{T}_i^{d4} + O(\gamma^5), \tag{2.46}$$

where

$$\begin{aligned}\mathbf{T}_i^{d1} =& 4\pi\epsilon_f(\mathbf{P}_i \times \nabla\phi_a(\mathbf{r_i}) + (\mathbf{Q}_i \cdot \nabla) \times \nabla\phi_a(\mathbf{r}_i)),\\ \mathbf{T}_i^{d2} =& -4\pi\epsilon_f\mathbf{P}_i \times \sum_{j\neq i}(\frac{1}{R_{ij}^3}\Pi \cdot \mathbf{P}_j),\\ \mathbf{T}_i^{d3} =& -4\pi\epsilon_f\mathbf{P}_i \times \sum_{j\neq i}(\frac{1}{2}\nabla_{\mathbf{R}_{ij}}\frac{\mathbf{R}_{ij}\mathbf{R}_{ij} : \mathbf{Q}_j}{R_{ij}^5}),\\ \mathbf{T}_i^{d4} =& -4\pi\epsilon_f(\mathbf{Q}_i \cdot \nabla) \times (\sum_{j\neq i}\frac{1}{R_{ij}^3}\Pi \cdot \mathbf{P}_j).\end{aligned} \tag{2.47}$$

Substitute force and torque balance into the mobility equation Eq. 2.40, we obtain the evolution equation for the particle translational velocity and angular velocity,

$$\begin{aligned}\mathbf{u}_i =& \mathbf{u}_i^\infty + \frac{\mathbf{F}_i^{el}}{6\pi a\eta_f} + \sum_{j\neq i}\frac{\mathbf{F}_{ij}^{rep}}{6\pi a\eta_f} + \sum_{j\neq i}\frac{(5\mathbf{F}_i^{el}\cdot\widehat{\mathbf{R}}_{ij})a^3\widehat{\mathbf{R}}_{ij}}{8\pi\eta_f R_{ij}^4}\\ &+ \frac{1}{\eta_f}\sum_{j\neq i}[-\frac{\mathbf{T}_j^{dep}\times\widehat{\mathbf{R}}_{ij}}{8\pi R_{ij}^2}\\ &+ \frac{1}{8\pi}(\frac{1}{R_{ij}} + \frac{2a^2}{3R_{ij}^3})\mathbf{F}_j^{el}\\ &+ \frac{1}{8\pi}(\frac{1}{R_{ij}} - \frac{2a^2}{R_{ij}^3})(\mathbf{F}_j^{el}\cdot\widehat{\mathbf{R}}_{ij})\widehat{\mathbf{R}}_{ij}] + O(\gamma^5),\\ \mathbf{\Omega}_i =& \mathbf{\Omega}_i^\infty + \frac{\mathbf{T}_i^{el}}{8\pi a^3\eta_f}\\ &+ \frac{1}{\eta_f}\sum_{j\neq i}[-\frac{\mathbf{T}_j^{dep}}{16\pi R_{ij}^3} - \frac{3}{16\pi R_{ij}^3}(\mathbf{T}_j^{dep}\cdot\widehat{\mathbf{R}}_{ij})\widehat{\mathbf{R}}_{ij}\\ &- \frac{(\mathbf{F}_j^{el})\times\widehat{\mathbf{R}}_{ij}}{8\pi R_{ij}^2}] + O(\gamma^5).\end{aligned} \tag{2.48}$$

In Eq. 2.48, we introduce an artificial isotropic repulsion force [**53**] to prevent particle contact,

$$\mathbf{F}_{ij}^{rep} = F_0^r(\frac{r_c^2 - |\mathbf{R}_{ij}^2|}{r_c^2 - 4a^2})^2\widehat{\mathbf{R}}_{ij}, \quad R_{ij} \leq r_c, \tag{2.49}$$

where $r_c = 2.01a$ is a control distance used to simulate surface roughness and F_0^r is a characteristic repulsion force unit. $\mathbf{F}_{ij}^{rep} = \mathbf{0}$ if $R_{ij} > r_c$.

As given above, the accuracy of both $\mathbf{u}$ and $\mathbf{\Omega}$ is kept up to $O(\gamma^4)$. The quadrupole contributes to both the DEP force and torque calculation. However, we need to clarify that while this calculation holds well for any linear electric field, for non linear fields it may not be quite accurate. One reason was explained in the previous section that higher order moments are coupled into the equation when quadratic or higher order field components are non zero. The other reason is that for a rapidly or slowly changing field, the multipole moments have different magnitude scale. Then it is necessary to introduce another asymptotic parameter. Later, we will discuss a slowly varying electric field, which is more commonly seen in practical applications.

Assuming widely separated particles, as discussed earlier from Eq. 2.15 and Eq. 2.16, adding the perturbation field induced by other particles, the evolution equations of the multipole moments of the i^{th} particle are,

$$\begin{aligned} \frac{d\mathbf{P}_i}{dt} =& \mathbf{\Omega}_i \times [\mathbf{P}_i + a^3\epsilon_{cm}(\nabla\phi_a(\mathbf{r}_i) + \sum_{j\neq i}(\frac{1}{R_{ij}^3}\Pi \cdot \mathbf{P}_j + \frac{1}{2}\nabla_{\mathbf{R}_{ij}}\frac{\mathbf{R}_{ij}\mathbf{R}_{ij} : \mathbf{Q}_j}{R_{ij}^5}))] \\ &- \frac{1}{\tau_{mw}}[\mathbf{P}_i + a^3\sigma_{cm}(\nabla\phi_a(\mathbf{r}_i) + \sum_{j\neq i}(\frac{1}{R_{ij}^3}\Pi \cdot \mathbf{P}_j + \frac{1}{2}\nabla_{\mathbf{R}_{ij}}\frac{\mathbf{R}_{ij}\mathbf{R}_{ij} : \mathbf{Q}_j}{R_{ij}^5}))], \end{aligned} \tag{2.50}$$

and

$$\begin{aligned}\frac{d\mathbf{Q}_i}{dt} =&\boldsymbol{\Omega}_i \times [\mathbf{Q}_i + 2a^5\epsilon'_{cm}(\nabla\nabla\phi_a(\mathbf{r}_i) + \sum_{j\neq i}\nabla_{\mathbf{R}_{ij}}(\frac{1}{R_{ij}^3}\Pi\cdot\mathbf{P}_j)] \\ &+ \{\boldsymbol{\Omega}_i \times [\mathbf{Q}_i + 2a^5\epsilon'_{cm}(\nabla\nabla\phi_a(\mathbf{r}_i) + \sum_{j\neq i}\nabla_{\mathbf{R}_{ij}}(\frac{1}{R_{ij}^3}\Pi\cdot\mathbf{P}_j)]\}^{\mathsf{T}} \\ &- \frac{1}{\tau'_{mw}}[\mathbf{Q}_i + 2a^5\sigma'_{cm}(\nabla\nabla\phi_a(\mathbf{r}_i) + \sum_{j\neq i}\nabla_{\mathbf{R}_{ij}}(\frac{1}{R_{ij}^3}\Pi\cdot\mathbf{P}_j)].\end{aligned}\tag{2.51}$$

$$\begin{aligned}\frac{d\mathbf{Q}_i}{dt} =&\{\boldsymbol{\Omega}_i \times [\mathbf{Q}_i + 2a^5\epsilon'_{cm}(\nabla\nabla\phi_a(\mathbf{r}_i) \\ &+ \sum_{j\neq i}\nabla_{\mathbf{R}_{ij}}(\frac{1}{R_{ij}^3}\Pi\cdot\mathbf{P}_j)]\}^{sym} \\ &- \frac{1}{\tau'_{mw}}[\mathbf{Q}_i + 2a^5\sigma'_{cm}(\nabla\nabla\phi_a(\mathbf{r}_i) + \sum_{j\neq i}\nabla_{\mathbf{R}_{ij}}(\frac{1}{R_{ij}^3}\Pi\cdot\mathbf{P}_j)].\end{aligned}\tag{2.52}$$

where $R_{ij} = |\mathbf{R}_{ij}| = |\mathbf{r}_j - \mathbf{r}_i|$, $\Pi = \mathbf{I} - 3\widehat{\mathbf{R}}_{ij}\widehat{\mathbf{R}}_{ij}$, sym denotes $A_{ij}^{sym} = A_{ij} + A_{ij}^{\mathsf{T}}$. The truncation error is $O((a/R_{ij})^5)$ in this approximation. Here it is assumed that the minimum R_{ij} over all $i \neq j$ is used to estimate the error.

For an applied linear electric field, the evolution equations are exact. For a general non-uniform electric field, especially a field which rapidly varies on the particle scale, the truncation of multipole moments as well as the Taylor expansion of the applied field introduce error. However, we are still able to set up a similar model for slowly varying fields by doing a systematic asymptotic analysis and assuming a proper balancing order for the scales of the applied field and the disturbance field, which can be found later.

2.3.2. Two-particle Dynamics

In a field defined as Eq. 2.29 in section 2.2.1, fig. 2.5 shows the interaction of two identical particles at different applied field gradient strenght values G. The spheres move towards the origin (location of minimum field), due to the dielectophoretic (DEP) force, while also executing rotations, due to the Quincke effect. In a uniform field, the spheres would orbit around each other [**33, 35**]. In the non-uniform field, this orbiting motion is superimposed on the DEP translation. The circle which satisfies Eq. 2.28 is drawn in fig. 2.5(a)(b). This circle represents the boundary of the existence of a steady nonzero $\mathbf{\Omega}$, hence within the circle only transient rotation can exist.

In our computations, the two particles are positioned in the electrorotation region and random initial polarizations are applied. Computations from different initial polarizations and different electric field strengths are presented in fig. 2.5. In fig. 2.5.(a), particles start rotating in the same direction, but hydrodynamic interactions drive the particle pair to orbit about each other. Meanwhile they translate towards the 'non-Quincke' region due to DEP force. The rotation decays to zero once they enter it. In fig. 2.5.(b), the spheres are counterrotating and form a translating pair moving quite linearly to the 'non-Quincke' region. In stronger fields, the non-rotation region shrinks. As shown in fig. 2.5.(c)-(d), the DEP force from the external field dominates the pair interactions. However when particles come close to each other, we observe a pairing phenomenon due to their rotation. In the first example, fig. 2.5.(c), the two particles form a co-rotating cluster. In fig. 2.5.(d), we find that the two particles form a stationary counter-rotating pair due to the balance of DEP force and hydrodynamic interaction.

We note that in the previous pair-particle cases, the particles are initially in the $x-z$ plane of the applied electric field and no initial disturbance is given in the y-direction Thus no motion in the y-direction is present. However, if the particle initial alignment is not in the $x-z$ plane of the electric field or there is any orthogonal perturbation (in the

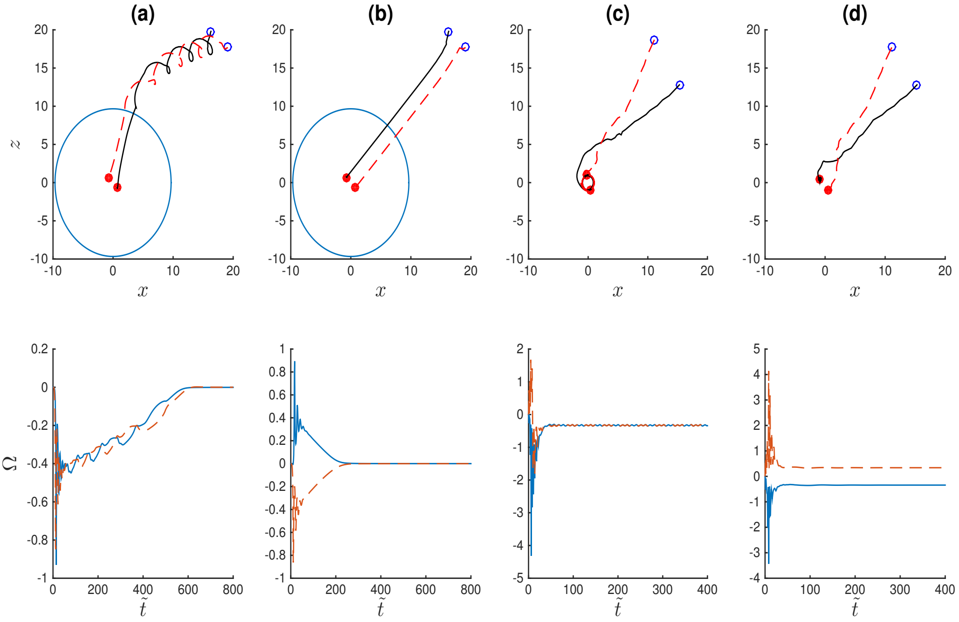

Figure 2.5. Particle dynamic patterns with different field strength parameter G. Initial $\mathbf{P}$ is given randomly at $O(10^{-4})$ The non-electrorotation region is indicated by the circle satisfying Eq. 2.28. $D = 5.1520$, $D' = 5.6054$. (a) co-rotating pair, $G = 0.1$, (b) counter-rotating pair, $G = 0.1$, (c) co-rotating pair, $G = 1.0$, (d) counter-rotating pair, $G = 1.0$.

y-direction), the in-plane motion is not stable. In this case particles eventually form a chain orthogonal to the field plane, i.e. along y-axis in our field set-up. Particles axis of rotation are then orthogonal to the $x - z$ plane.

2.3.3. Simulation of Particle Clustering

The nonuniform electric field can be utilized to assemble structures of spheres, such as clusters.

Fig. 2.6 shows that spheres in a linear field defined in Eq. 2.29 form a chain extending along the y direction , i.e. the direction of rotation. However in stronger fields, no stable assembly exists and the multi-particle dynamics is complex (similar to the single particle scenario).

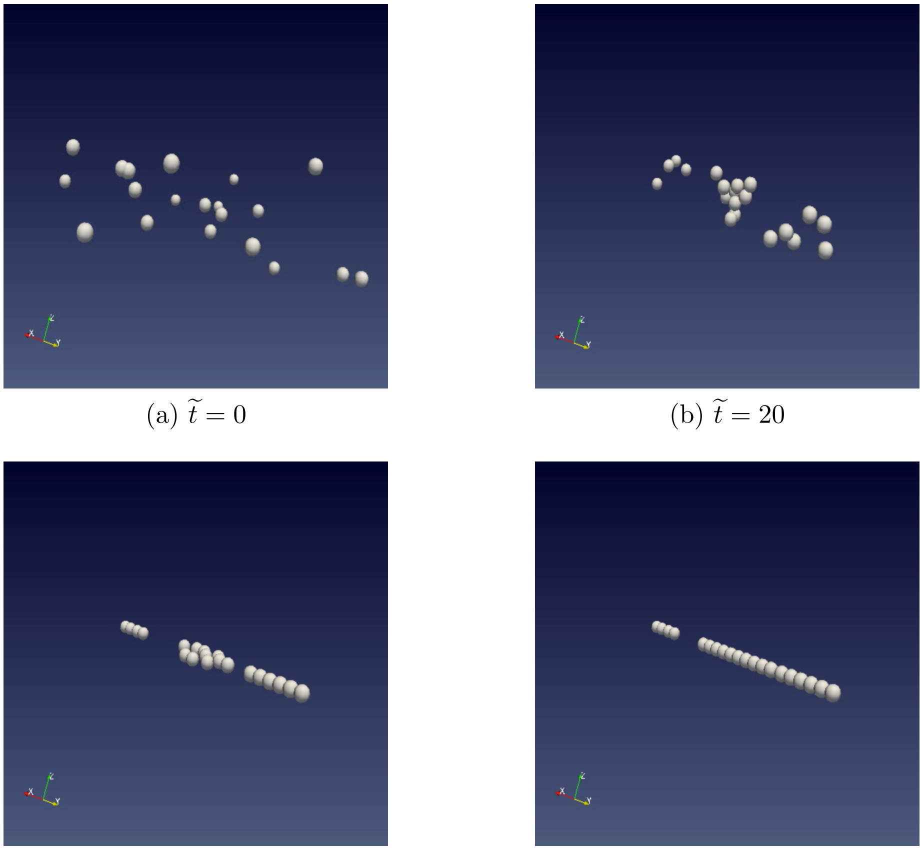

(a) $\widetilde{t} = 0$ (b) $\widetilde{t} = 20$

(c) $\widetilde{t} = 200$ (d) $\widetilde{t} = 2000$

Figure 2.6. Dynamics of 20 particles in linear field with random initial positions. Chaining at Y-axis is observed. $G = 1.0$. $D = 5.1520$. $\tilde{t} = 0, 20, 200, 2000$.

2.4. Multi-particle Dynamics in Slowly Varying Non-uniform Fields

2.4.1. General Formulation

Our model can be applied to study particle dynamics in a more general non-uniform fields. For a single particle suspended in a general slowly varying electric field, we want to look at the asymptotic behavior when the particle radius is much smaller than the non-uniformity. The classic DEP force and torque calculation gives Eq. 2.42 when the exact dipole and quadrupole moments are known. However, we would like to point out that, for a general electric field that induced non-zero octopole and higher moments, the error by truncating octopole moments comes at the same scale of the quadrupole contribution.

Suppose a potential ϕ_a is applied externally in a single particle suspension. The Taylor expansion of the applied electric field at the particle center is,

$$\nabla\phi_a(\mathbf{r}) = \nabla\phi_a(\mathbf{0}) + \nabla\nabla\phi_a(\mathbf{0})\cdot\mathbf{r} + \frac{1}{2}\nabla\nabla\nabla\phi_a(\mathbf{0}) : \mathbf{rr} + \cdots . \tag{2.53}$$

For slowly varying fields, we assume the length scale of the gradient operator is $L \gg a$, where a is the particle radius. Thus we denote

$$-\left(\nabla\right)^n\phi_a \equiv \mathbf{E}_a^{(n-1)} = \frac{E_0}{L^{n-1}}\widetilde{\mathbf{E}}_a^{(n-1)}, \quad n \geq 1, \tag{2.54}$$

where E_0 is a characteristic electric field strength. i.e. $\widetilde{\mathbf{E}}_a^{(0)}$ indicates the leading term of the scaled electric field. All the $|\widetilde{\mathbf{E}}_a^{(n)}|$ are at $O(1)$.

In the following asymptotic analysis, we use the scaling scheme as,

$$\tilde{t} = t/t_{ehd}, \quad \widetilde{\mathbf{\Omega}} = \mathbf{\Omega} t_{ehd}, \quad \tilde{\mathbf{r}} = \mathbf{r}/a,$$
$$\widetilde{\mathbf{P}} = \frac{\mathbf{P}}{E_0 a^3}, \quad \widetilde{\mathbf{Q}} = \frac{\mathbf{Q}}{E_0 a^4},$$

where $t_{ehd} = \frac{\eta_f}{\epsilon_f E_0^2}$ is a characteristic EHD time scale.

Then the dimensionless form of the expansion Eq. 2.53 with the remainder term is,

$$\begin{aligned}\widetilde{\mathbf{E}}_a(\tilde{\mathbf{r}}) =& \widetilde{\mathbf{E}}_a^{(0)}(\mathbf{0}) + \delta\widetilde{\mathbf{E}}_a^{(1)}(\mathbf{0})\cdot\tilde{\mathbf{r}} + \frac{1}{2}\delta^2\widetilde{\mathbf{E}}_a^{(2)}(\mathbf{0}) : \tilde{\mathbf{r}}\tilde{\mathbf{r}} \\ &+ \frac{1}{6}\delta^3\widetilde{\mathbf{E}}_a^{(3)}(\mathbf{0})[\cdot]^3\tilde{\mathbf{r}}\tilde{\mathbf{r}}\tilde{\mathbf{r}} + \cdots ,\end{aligned} \tag{2.55}$$

where $\delta = a/L \ll 1$ is a small asymptotic parameter.

Meanwhile, following Eq. 2.3, the dimensionless form of the induced field in the outer space has the expansion as,

$$\begin{aligned}\widetilde{\mathbf{E}}_d(\tilde{\mathbf{r}}) = &-\frac{\widetilde{\mathbf{P}}}{|\tilde{\mathbf{r}}|^3} + \frac{3\tilde{\mathbf{r}}\cdot\widetilde{\mathbf{P}}}{|\tilde{\mathbf{r}}|^5}\tilde{\mathbf{r}} - \frac{\widetilde{\mathbf{Q}}\cdot\tilde{\mathbf{r}}}{|\tilde{\mathbf{r}}|^5} + \frac{5\tilde{\mathbf{r}}\tilde{\mathbf{r}}:\widetilde{\mathbf{Q}}}{2|\tilde{\mathbf{r}}|^7}\tilde{\mathbf{r}} \\ &- \frac{3\widetilde{\boldsymbol{\mathcal{O}}}:\tilde{\mathbf{r}}\tilde{\mathbf{r}}}{2|\tilde{\mathbf{r}}|^7} + \frac{7\widetilde{\boldsymbol{\mathcal{O}}}[\cdot]^3\tilde{\mathbf{r}}\tilde{\mathbf{r}}\tilde{\mathbf{r}}}{2|\tilde{\mathbf{r}}|^9}\tilde{\mathbf{r}} + \cdots .\end{aligned} \tag{2.56}$$

From Eq. 2.50, when other particles are present, the induced potentials from other particles should be introduced into the total electric field. These disturbance fields contribute to the total external field as,

$$\widetilde{\mathbf{E}}_{e,i} = \widetilde{\mathbf{E}}_{a,i} + \sum_{j\neq i}\widetilde{\mathbf{E}}_{d,j}. \tag{2.57}$$

Assuming the particles are widely separated, $\mathbf{E}_{d,j}$ would be expanded in a far-field form. At the center of particle i, the field is

$$\widetilde{\mathbf{E}}_{d,j} = -\frac{1}{|\widetilde{\mathbf{R}}_{ij}|^3}\Pi_1\widetilde{\mathbf{P}}_j - \frac{1}{|\widetilde{\mathbf{R}}_{ij}|^4}\Pi_2\widetilde{\mathbf{Q}}_j, \tag{2.58}$$

where $\Pi_1\widetilde{\mathbf{P}}_j = \widetilde{\mathbf{P}}_j - 3(\widetilde{\mathbf{P}}_j\cdot\widehat{\mathbf{R}}_{ij})\widehat{\mathbf{R}}_{ij}$ and $\Pi_2\widetilde{\mathbf{Q}}_j = \widetilde{\mathbf{Q}}_j\cdot\widehat{\mathbf{R}}_{ij} - \frac{5}{2}(\widetilde{\mathbf{Q}}_j : \widehat{\mathbf{R}}_{ij}\widehat{\mathbf{R}}_{ij})\widehat{\mathbf{R}}_{ij}$. Here we also have truncated the potential due to octopole and higher moments.

Now we encounter the second length scale, which is the particle separations $|\widetilde{\mathbf{R}}_{ij}|$. Assume a characteristic particle separation $\widetilde{R}_0 \gg 1$. Denote $\gamma = 1/\widetilde{R}_0$, $\overline{\mathbf{R}}_{ij} = \widetilde{\mathbf{R}}_{ij}/\widetilde{R}_0$ and also assume all the particle separations are at the same scale, i.e.

$$\frac{1}{|\widetilde{\mathbf{R}}_{ij}|} = \gamma\frac{1}{|\overline{\mathbf{R}}_{ij}|} \sim O(\gamma). \tag{2.59}$$

Then we need to carefully select an appropriate asymptotic matching for the two small parameters δ and γ.

In order to incorporate particle interactions, we assume the balance as

$$\delta = \gamma^2, \tag{2.60}$$

which indicates an even slower varying applied field than the particle disturbances.

Then we are able to expand the multipole moments in terms of the parameter γ, without causing fractal orders. Still from Eq. 2.50, Eq. 2.51 and their derivation in the previous sections, we obtain the nonzero terms in the multipole moments' expansions are

$$\begin{aligned} \widetilde{\mathbf{P}} &= \widetilde{\mathbf{P}}^{(0)} + \gamma^3 \widetilde{\mathbf{P}}^{(3)} + \gamma^4 \widetilde{\mathbf{P}}^{(4)} + \cdots , \\ \widetilde{\mathbf{Q}} &= \gamma^2 \widetilde{\mathbf{Q}}^{(2)} + \gamma^4 \widetilde{\mathbf{Q}}^{(4)} + \cdots , \\ \widetilde{\boldsymbol{\mathcal{O}}} &= \gamma^4 \widetilde{\boldsymbol{\mathcal{O}}}^{(4)} + \cdots , \\ &\cdots . \end{aligned} \tag{2.61}$$

Assuming $\widetilde{\mathbf{\Omega}}^{\infty} = \mathbf{0}$, the rotation is actually determined by the multiple moments from Eq. 2.48. In our balancing, the leading order nonzero contribution will be $\mathbf{\Omega}^{(0)}$ and the next nonzero orders should be $\mathbf{\Omega}^{(3)}$ and $\mathbf{\Omega}^{(4)}$. Thus we obtain

$$\widetilde{\mathbf{\Omega}} = \widetilde{\mathbf{\Omega}}^{(0)} + \gamma^3 \widetilde{\mathbf{\Omega}}^{(3)} + \gamma^4 \widetilde{\mathbf{\Omega}}^{(4)} + \cdots . \tag{2.62}$$

Besides, each order of dipole moment satisfies the following evolution equations,

$O(1)$:

$$\frac{d\widetilde{\mathbf{P}}^{(0)}}{dt} = \widetilde{\mathbf{\Omega}}^{(0)} \times [\widetilde{\mathbf{P}}^{(0)} - \epsilon_{cm} \widetilde{\mathbf{E}}_a^{(0)}(\mathbf{0})] - \frac{1}{D}[\widetilde{\mathbf{P}}^{(0)} - \sigma_{cm} \widetilde{\mathbf{E}}_a^{(0)}(\mathbf{0})]; \tag{2.63}$$

$O(\gamma^3)$:

$$\begin{aligned}\frac{d\widetilde{\mathbf{P}}^{(3)}}{dt} =&\widetilde{\boldsymbol{\Omega}}^{(0)} \times [\widetilde{\mathbf{P}}^{(3)} + \epsilon_{cm}\frac{1}{|\overline{\mathbf{R}}_{ij}|^3}\Pi_1\widetilde{\mathbf{P}}_j^{(0)}] + \widetilde{\boldsymbol{\Omega}}^{(3)} \times \widetilde{\mathbf{P}}^{(0)} \\ &- \frac{1}{D}[\widetilde{\mathbf{P}}^{(3)} + \sigma_{cm}\frac{1}{|\overline{\mathbf{R}}_{ij}|^3}\Pi_1\widetilde{\mathbf{P}}_j^{(0)}];\end{aligned} \tag{2.64}$$

$O(\gamma^3)$:

$$\begin{aligned}\frac{d\widetilde{\mathbf{P}}^{(4)}}{dt} =&\widetilde{\boldsymbol{\Omega}}^{(4)} \times [\widetilde{\mathbf{P}}^{(0)} - \epsilon_{cm}\widetilde{\mathbf{E}}_a^{(0)}(\mathbf{0})] + \widetilde{\boldsymbol{\Omega}}^{(4)} \times \widetilde{\mathbf{P}}^{(0)} \\ &- \frac{1}{D}\widetilde{\mathbf{P}}^{(4)}.\end{aligned} \tag{2.65}$$

The next correction to the dipole moment will be at $O(\gamma^4)$.

From Eq. 2.16, similarly we obtain, the leading nonzero quadrupole moment comes at the order of $O(\gamma^2)$, satisfying the equation below,

$O(\gamma^2)$:

$$\begin{aligned}\frac{d\widetilde{\mathbf{Q}}^{(2)}}{d\tilde{t}} =&\widetilde{\boldsymbol{\Omega}}^{(0)} \times [\widetilde{\mathbf{Q}}^{(2)} - 2\epsilon'_{cm}\widetilde{\mathbf{E}}_a^{(1)}(\mathbf{0})] \\ &+ [\widetilde{\boldsymbol{\Omega}}^{(0)} \times [\widetilde{\mathbf{Q}}^{(2)} - 2\epsilon'_{cm}\widetilde{\mathbf{E}}_a^{(1)}(\mathbf{0})]]^{\mathsf{T}} \\ &- \frac{1}{D'}[\widetilde{\mathbf{Q}}^{(2)} - 2\sigma'_{cm}\widetilde{\mathbf{E}}_a^{(1)}(\mathbf{0})];\end{aligned} \tag{2.66}$$

$O(\gamma^4)$:

$$\begin{aligned}\frac{d\widetilde{\mathbf{Q}}^{(4)}}{d\tilde{t}} =&\widetilde{\boldsymbol{\Omega}}^{(0)} \times [\widetilde{\mathbf{Q}}^{(4)} + 2\epsilon'_{cm}\widetilde{\nabla}_{\overline{\mathbf{R}}_{ij}}(\frac{1}{|\overline{\mathbf{R}}_{ij}|^3}\Pi_1\widetilde{\mathbf{P}}_j^{(0)})] \\ &+ [\widetilde{\boldsymbol{\Omega}}^{(0)} \times [\widetilde{\mathbf{Q}}^{(4)} + 2\epsilon'_{cm}\widetilde{\nabla}_{\overline{\mathbf{R}}_{ij}}(\frac{1}{|\overline{\mathbf{R}}_{ij}|^3}\Pi_1\widetilde{\mathbf{P}}_j^{(0)})]]^{\mathsf{T}} \\ &- \frac{1}{D'}[\widetilde{\mathbf{Q}}^{(4)} + 2\sigma'_{cm}\widetilde{\nabla}_{\overline{\mathbf{R}}_{ij}}(\frac{1}{|\overline{\mathbf{R}}_{ij}|^3}\Pi_1\widetilde{\mathbf{P}}_j^{(0)})].\end{aligned} \tag{2.67}$$

The next nonzero contribution is $\widetilde{\mathbf{Q}}^{(6)}$ at the order of $O(\gamma^6)$.

Here we continue to look at the expansions of the force and torque. The DEP force and torque are originally calculated directly by integrating the Maxwell stress tensor $\boldsymbol{\Sigma}$,

$$\widetilde{\mathbf{F}} = \frac{1}{4\pi}\iint_{|\tilde{\mathbf{r}}|=1} \widetilde{\boldsymbol{\Sigma}} \cdot \mathbf{n} d\tilde{S}, \quad \widetilde{\mathbf{T}} = \frac{1}{4\pi}\iint_{|\tilde{\mathbf{r}}|=1} \tilde{\mathbf{r}} \times (\widetilde{\boldsymbol{\Sigma}} \cdot \mathbf{n}) d\tilde{S}, \tag{2.68}$$

where

$$\widetilde{\boldsymbol{\Sigma}} = \widetilde{\mathbf{E}}\widetilde{\mathbf{E}} - \frac{1}{2}|\widetilde{\mathbf{E}}|^2\mathbf{I}, \tag{2.69}$$

while $\widetilde{\mathbf{E}}$ is the total field.

For a spherical particle which has the standard multipole potential and exposed to a slowly varying external field, the force and torque equations are given in the exact forms as,

$$\begin{aligned} \widetilde{\mathbf{F}} &= \widetilde{\mathbf{P}} \cdot \widetilde{\nabla}\widetilde{\mathbf{E}}_e(\mathbf{0}) + \frac{1}{6}\widetilde{\mathbf{Q}} : \widetilde{\nabla}\widetilde{\nabla}\widetilde{\mathbf{E}}_e(\mathbf{0}) + \cdots , \\ \widetilde{\mathbf{T}} &= \widetilde{\mathbf{P}} \times \widetilde{\mathbf{E}}_e(\mathbf{0}) + (\widetilde{\mathbf{Q}} \cdot \widetilde{\nabla}) \times \widetilde{\mathbf{E}}_e(\mathbf{0}) + \cdots , \end{aligned} \tag{2.70}$$

By substituting Eq. 2.57,Eq. 2.58 and the expansion Eq. 2.61, we obtain the force and torque in each order of γ.

$$\begin{aligned} \widetilde{\mathbf{F}}_i =& \gamma^2\widetilde{\mathbf{P}}_i^{(0)} \cdot \widetilde{\mathbf{E}}_{a,i}^{(1)}(\mathbf{0}) + \gamma^5\widetilde{\mathbf{P}}_i^{(3)} \cdot \widetilde{\mathbf{E}}_{a,i}^{(1)}(\mathbf{0}) + \gamma^6\widetilde{\mathbf{P}}_i^{(4)} \cdot \widetilde{\mathbf{E}}_{a,i}^{(1)}(\mathbf{0}) \\ &+ \frac{1}{6}\gamma^6\widetilde{\mathbf{Q}}_i^{(2)} : \widetilde{\mathbf{E}}_a^{(2)}(\mathbf{0}) \\ &- \gamma^4\sum_{j\neq i}\widetilde{\mathbf{P}}_i^{(0)} \cdot \widetilde{\nabla}_{\overline{\mathbf{R}}_{ij}}\left(\frac{1}{|\overline{\mathbf{R}}_{ij}|^3}\Pi_1\widetilde{\mathbf{P}}_j^{(0)}\right) \\ &+ O(\gamma^7). \end{aligned} \tag{2.71}$$

$$\begin{aligned}\widetilde{\mathbf{T}}_i =& \widetilde{\mathbf{P}}_i^{(0)} \times \widetilde{\mathbf{E}}_{a,i}^{(0)}(\mathbf{0}) + \gamma^3 \widetilde{\mathbf{P}}_i^{(3)} \times \widetilde{\mathbf{E}}_{a,i}^{(0)}(\mathbf{0}) + \gamma^4 \widetilde{\mathbf{P}}_i^{(4)} \times \widetilde{\mathbf{E}}_{a,i}^{(0)}(\mathbf{0}) \\ & + \gamma^4 \widetilde{\mathbf{Q}}_i^{(2)} \times \widetilde{\mathbf{E}}_{a,i}^{(1)}(\mathbf{0}) \\ & - \gamma^3 \sum_{j\neq i} \widetilde{\mathbf{P}}_i^{(0)} \times \frac{1}{|\overline{\mathbf{R}}_{ij}|^3} \Pi_1 \widetilde{\mathbf{P}}_j^{(0)} \\ & + O(\gamma^5).\end{aligned} \tag{2.72}$$

The orders of error are kept at $O(\gamma^7)$ and $O(\gamma^5)$ respectively.

Adding up all the required terms in the order of accuracy, the evolution equations of $\widetilde{\mathbf{P}}$ and $\widetilde{\mathbf{Q}}$ are,

$$\begin{aligned}\frac{d\widetilde{\mathbf{P}}_i}{d\tilde{t}} =& \widetilde{\boldsymbol{\Omega}}_i \times [\widetilde{\mathbf{P}}_i - \epsilon_{cm} \widetilde{\mathbf{E}}_a^{(0)}(\tilde{\mathbf{r}}_i) + \sum_{j\neq i} \frac{1}{|\widetilde{\mathbf{R}}_{ij}|^3} \Pi_1 \widetilde{\mathbf{P}}_j] \\ & - \frac{1}{D}[\widetilde{\mathbf{P}}_i - \sigma_{cm} \widetilde{\mathbf{E}}_a^{(0)}(\tilde{\mathbf{r}}_i) + \sum_{j\neq i} \frac{1}{|\widetilde{\mathbf{R}}_{ij}|^3} \Pi_1 \widetilde{\mathbf{P}}_j] + O(\gamma^5),\end{aligned} \tag{2.73}$$

$$\begin{aligned}\frac{d\widetilde{\mathbf{Q}}_i}{d\tilde{t}} =& \widetilde{\boldsymbol{\Omega}}_i \times [\widetilde{\mathbf{Q}}_i - 2\epsilon'_{cm} \delta \widetilde{\mathbf{E}}_a^{(1)}(\tilde{\mathbf{r}}_i)] \\ & + [\widetilde{\boldsymbol{\Omega}}_i \times [\widetilde{\mathbf{Q}}_i - 2\epsilon'_{cm} \delta \widetilde{\mathbf{E}}_a^{(1)}(\tilde{\mathbf{r}}_i)]]^{\mathsf{T}} \\ & - \frac{1}{D'}[\widetilde{\mathbf{Q}}_i - 2\sigma'_{cm} \delta \widetilde{\mathbf{E}}_a^{(1)}(\tilde{\mathbf{r}}_i)] + O(\gamma^4).\end{aligned} \tag{2.74}$$

The rotation and velocity are determined from the grand-mobility matrix as well,

$$\begin{aligned}\widetilde{\boldsymbol{\Omega}}_i = & \frac{\widetilde{\mathbf{T}}_i}{8} - \sum_{j\neq i} [\frac{\widetilde{\mathbf{F}}_j \times \widehat{\mathbf{R}}_{ij}}{8|\widetilde{\mathbf{R}}_{ij}|^2} \\ & + \frac{\widetilde{\mathbf{T}}_j}{16|\widetilde{\mathbf{R}}_{ij}|^3} + \frac{3}{16|\widetilde{\mathbf{R}}_{ij}|^3} (\widetilde{\mathbf{T}}_j \cdot \widehat{\mathbf{R}}_{ij}) \widehat{\mathbf{R}}_{ij}] + O(\gamma^7),\end{aligned} \tag{2.75}$$

$$
\begin{aligned}
\tilde{\mathbf{u}}_i = \tilde{\mathbf{u}}_i^{\infty} &+ \frac{\widetilde{\mathbf{F}}_i}{6} + \sum_{j\neq i} \frac{5}{8|\widetilde{\mathbf{R}}_{ij}|^4}(\widetilde{\mathbf{F}}_i \cdot \widehat{\mathbf{R}}_{ij})\widehat{\mathbf{R}}_{ij} \\
&- \sum_{j\neq i}[\frac{\widetilde{\mathbf{T}}_j \times \widehat{\mathbf{R}}_{ij}}{8|\widetilde{\mathbf{R}}_{ij}|^2} + \frac{1}{8}(\frac{1}{|\widetilde{\mathbf{R}}_{ij}|} + \frac{2}{3|\widetilde{\mathbf{R}}_{ij}|^3})\widetilde{\mathbf{F}}_j \\
&+ \frac{1}{8}(\frac{1}{|\widetilde{\mathbf{R}}_{ij}|} - \frac{2}{|\widetilde{\mathbf{R}}_{ij}|^3})(\widetilde{\mathbf{F}}_j \cdot \widehat{\mathbf{R}}_{ij})\widehat{\mathbf{R}}_{ij}] + O(\gamma^7),
\end{aligned}
\tag{2.76}
$$

where

$$
\begin{aligned}
\widetilde{\mathbf{F}}_i =& 4\delta\widetilde{\mathbf{P}}_i \cdot \widetilde{\mathbf{E}}_a^{(1)}(\tilde{\mathbf{r}}_i) \\
&- \sum_{j\neq i} \frac{12}{|\widetilde{\mathbf{R}}_{ij}|^4}[(\widetilde{\mathbf{P}}_i \cdot \widehat{\mathbf{R}}_{ij})\widetilde{\mathbf{P}}_j + (\widetilde{\mathbf{P}}_j \cdot \widehat{\mathbf{R}}_{ij})\widetilde{\mathbf{P}}_i \\
&+ (\widetilde{\mathbf{P}}_i \cdot \widetilde{\mathbf{P}}_j)\widehat{\mathbf{R}}_{ij} - 5(\widetilde{\mathbf{P}}_j \cdot \widehat{\mathbf{R}}_{ij})(\widetilde{\mathbf{P}}_i \cdot \widehat{\mathbf{R}}_{ij})\widehat{\mathbf{R}}_{ij}] \\
&+ \frac{2}{3}\delta^2\widetilde{\mathbf{Q}}_i : \widetilde{\mathbf{E}}_a^{(2)}(\tilde{\mathbf{r}}_i),
\end{aligned}
\tag{2.77}
$$

and

$$
\begin{aligned}
\widetilde{\mathbf{T}}_i =& 4\widetilde{\mathbf{P}}_i \times \widetilde{\mathbf{E}}_a^{(0)}(\tilde{\mathbf{r}}_i) \\
&- 4\widetilde{\mathbf{P}}_i \times \sum_{j\neq i}(\frac{1}{|\widetilde{\mathbf{R}}_{ij}|^3}\Pi_1 \cdot \widetilde{\mathbf{P}}_j) \\
&+ 4\delta\widetilde{\mathbf{Q}}_i \times \widetilde{\mathbf{E}}_a^{(1)}(\tilde{\mathbf{r}}_i).
\end{aligned}
\tag{2.78}
$$

Thus in the case of a spatially-slowly varying field, equations Eq. 2.73, Eq. 2.74, Eq. 2.75 and Eq. 2.76 are the proper model to simulate particle dynamics., where the error of the particle velocities is kept at $O(\widetilde{R}_0^{-7})$.

2.4.2. Simulation of Particle Clustering

Taking use of the results from last section, we illustrate particles assembly in a slowly varying periodical electric potential which generates a spatially-periodic electric field

$$\widetilde{\mathbf{E}}_a = \frac{E_0}{E_c}[\delta' \sin(\delta'\tilde{x})\sinh(\delta'\tilde{z})\mathbf{i} - \delta' \cos(\delta'\tilde{x})\cosh(\delta'\tilde{z})\mathbf{k}]. \tag{2.79}$$

The field is periodic in x direction and can be generated by two separated plain electrodes with opposite sinusoidal applied potential.

Fig. 2.7 illustrates the simulation result for the case when $E_0 = E_c$ which is calculated in section 2.2.2 and $\delta' = \pi/16$ and 60 particles. The particles are observed to cluster at $x - y$ plane and form chains periodically localized at all zero points of field strength. This is also majorly due to a negative DEP effect. The chains formed at the end are stable while each particle undergoes steady rotation.

2.5. Conclusion

In this chapter a model was developed to investigate the dynamics of spheres in a nonuniform electric field when Quincke rotation has significant effect on the dynamics. Our theory is built on the Taylor-Melcher leaky dielectric model, which assumes ohmic conduction in the bulk and creeping flow. Considering an applied field with spatial variations much larger than the inter-particle spacing and the radius of the spheres, particle polarization is approximated by the dipole and quadrupole moments. This reduces the problem to a system of ordinary differential equations for the particle position, rotation rate, dipole and quadrupole moments. In this chapter we focused on an applied linear electric field in which case the approximation is exact.

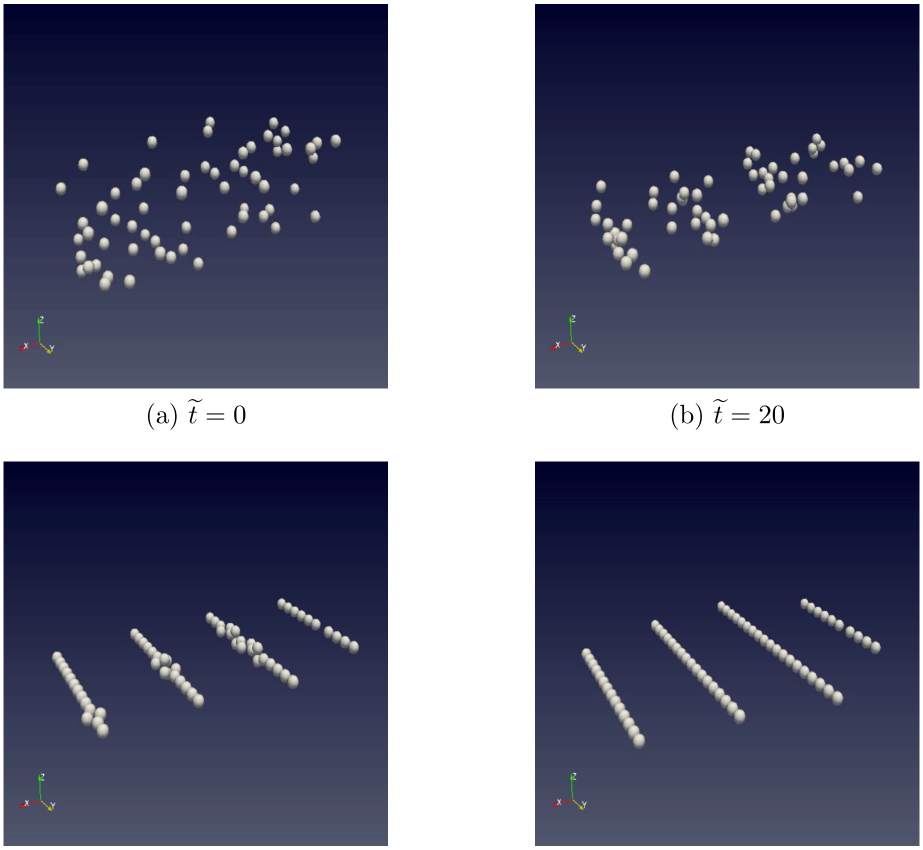

(a) $\widetilde{t} = 0$

(b) $\widetilde{t} = 20$

(c) $\widetilde{t} = 200$

(d) $\widetilde{t} = 2000$

Figure 2.7. Dynamics of 60 particles in periodical field with random initial positions with $\tilde{x} \in [0, 60]$. Clustering at $\tilde{z} = 0$ plane is observed. Four chains are formed at $\tilde{x} = 8, 24, 40, 56$. $E_0/E'_c = 1.0$. $\delta' = \frac{\pi}{16}$. $D = 5.1520$. $\tilde{t} = 0, 20, 200, 2000$.

In the study of the steady state of single sphere, we identified a necessary condition for when the nonuniform field induces Quincke rotation. We found that the threshold for electorotation in a linear field is lower that in the uniform field case. Increasing the electric field strength, makes the particle dynamics more complex: while Quincke electrorotation is characterized by steady spinning around the particle center, in stronger fields time-dependent orbiting motion around the minimum field location is observed.

We generalized the model to consider multi-particle simulations in arbitrary (but spatially slowly varying) applied fields. Hydrodynamic interactions were included via the grand-mobility matrix. In the leading order analysis, we retained terms in the far field expansions up to forth order in the inter particle spacing. The electrostatic interactions between particles include dipole-dipole and dipole-quadrupole interactions which are naturally introduced from the dielecropheritc force calculation. A numerical study of two-particle and multi-particle systems were considered for the special case of a linear applied field. Our calculation show intricate trajectories in the case of pairs, and chain-like assemblies in the case of many particles.

The model provided basis to study the collective dynamics of many particles in a general electric field. The model can also be extended to include ambient flow, and thus can be applied to study problems in electrorheology.

CHAPTER 3

Colloidal Particle at A Fluid-fluid Interface

3.1. Introduction

Micron-sized (colloidal) particles trapped at a two-phase interface are often encountered in natural and industrial processes, e.g., oil recovery, and employed in variety of applications, e.g., to stabilize emulsions [**1, 2**]. These so-called Pickering emulsions are finding increasing use in the pharmaceutical, petroleum, food and personal care industries [**3**], in part because novel and more exotic emulsion properties become available as materials technology creates greater and greater variety of particles. The rational design of these novel emulsions requires understanding of the dynamics of particle-coated interfaces, which is currently lacking.

The interface greatly affects particle motion. For example, the drag coefficient of an interface-trapped sphere differs from the Stokes drag in a homogeneous fluid and depends of the properties of both liquids and the contact angle of the interface with the particle [**15, 54, 55, 56**]. Electrostatic effects due to particle charge or applied electric fields further complicate the problem, but remain largely unexplored despite their importance in phenomena such as particle clustering, chaining or dynamic patterning at a flat fluid interface [**57, 58**] or a liquid drop surface [**59, 60, 61**]. The force on a particle at a water-nonpolar planar interface due to particle charge or an applied uniform normal electric field was analyzed theoretically in [**22, 23, 62**]. These works assumed that the electric field does not penetrate into the water phase, i.e., the water phase is a perfect conductor. This simplification limits the applicability of the results. The work here considers the general case of three material phases of arbitrary conductivity, as well as the non-symmetric case of an applied electric field tangential to the planar interface. We analyze both the case of perfect dielectric materials, where the displacement field is continuous at the interface, and the case of leaky dielectric(weakly conducting) materials, where the electric current is continuous across the interface [**27**].

Paralleling the approach of [**22**], we reformulate the original electrostatic problem, described by a set of partial differential equations, into integral equations for the electric potential. This is done by transforming into toroidal coordinates and then applying the Mehler-Fock integral transform. The resulting equations are solved numerically and asymptotically. Computational results are presented for the electric potential and for the force on a single particle under a normal and tangential applied field. It is found that the particle experiences only a normal force in both cases. The analysis of the local field in the neighborhood of the contact line shows that the same integrable singularity occurs in both cases. In order to determine the interaction force between two particles resting on the interface, the limit of widely separated particle is considered, i.e., the distance between them is much larger than their radii. As a first step, we identify the far field asymptotic behavior of the electric potential in the neighborhood of the particle is determined. The leading order behavior includes both dipole and quadrupole contributions. Once the dipole and quadrupole terms are known, the far field interaction force between two particles is foundand shown to depend on the interparticle distance as R_0^{-4}. The force coefficients can be found analytically in the perfect dielectric case, but must the be calculated numerically for the leaky dielectric case. It is shown that the leading order force between particles is always repulsive for perfect dielectrics and governed by dipole-dipole interactions. It is also shown that for leaky dielectric particles the force can be attractive when the quadrupole terms are significant. However, in many cases when the force between leaky dielectric particles is repulsive, we show that it can be well-approximated by only dipole-dipole interactions. The results of this analysis can be generalized to the case multiple particles interacting on an interface.

3.2. Problem Formulation

Here we formulate the problem of a spherical particle of radius a at the interface between two fluids in an applied uniform electric field. We consider a planar fluid-fluid interface. The three-phase line (contact line) where the three phases meet is assumed to be axisymmetric about the particle and makes a constant contact angle, α, with the fluid-fluid interface, see fig. 3.1. Introducing the cylindrical coordinate system (r, θ, z), the particle interface is given by $r^2 + (z + a\cos\alpha)^2 = a^2$. With these assumptions, the contact angle determines the height $a(1 - \cos\alpha)$ of the particle above the planar interface which is located at $z = 0$. In particular, for $\alpha = 0$, the particle is completely submerged in the the lower fluid, while for $\alpha = \pi$, the particle is completely immersed in the upper fluid. Our objective is to determine the electric field in each phase, to calculate the electric force on the particle, and to determine the applied force on a second identical particle resting on the interface in the presence of the first particle.

We study two cases: normal and tangential (to the planar interface) applied electric field. The solution of the tangential case is non-symmetric but since it parallels the general approach of the symmetric applied normal field case we will only outline it. Fields applied at other angles can be derived by a straight-forward generalization of our approach.

As noted in fig. 3.1, the upper, lower and particle regions will be denoted by Ω_k, with $k = u, l, p$, respectively, and we will use subscripts to denoted variables in each of these regions. We also write the particle interface as $S = S_u \cup S_l$, where S_u is the particle interface touching the upper fluid, while S_l touches the lower region.

3.2.1. Applied Normal Field

Let us consider the case where a uniform applied electric field is applied normal to the fluid-fluid interface, see fig. 3.1, and as z tends to negative infinity, the electric field tends to $\vec{E} = -E_0\hat{z}$. The problem is axisymmetric about the z axis. We seek to determine the electric field in the whole domain, including the particle.

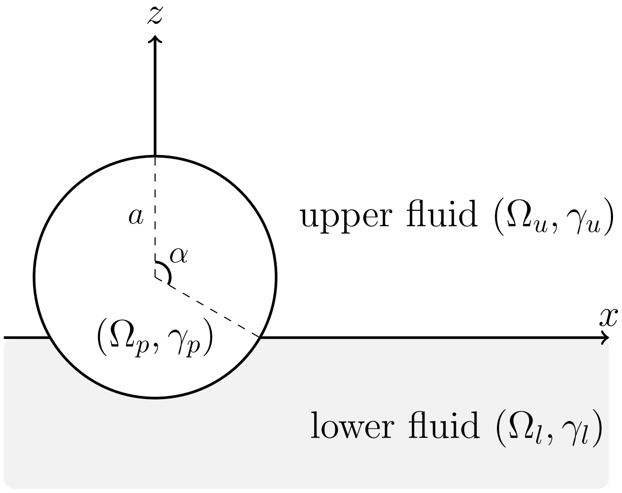

Figure 3.1. Spherical particle trapped at fluid-fluid interface. The x-axis of a cartesian system (x, y, z) is noted in the figure.

Introducing the electric potential, $\vec{E}_k = -\nabla\varphi_k$, in each region Ω_k with $k = u, l, p$, the potential problem is described as,

$$\nabla^2\varphi_k = 0, \quad \text{in} \quad \Omega_k, \quad \text{k=u,l,p.} \tag{3.1}$$

$$[\varphi] = 0, \quad \mathbf{n} \cdot [\gamma \vec{E}] = 0 \quad \text{at all interfaces.} \tag{3.2}$$

Eq. (3.1) expresses the fact that the electric field is divergence free. In (3.2) we use the notation that $[f]$ represents the jump in f across the interface. The first boundary condition in Eq. (3.2) is the continuity of the tangential electric field. The physical interpretation of our problem rests with the definition of γ_k in the second boundary condition in Eq. (3.2). If all phases were perfect dielectrics and γ_k is defined as the dielectric constant, ϵ_k, then Eq. (3.2) states the continuity of the normal displacement field and that there is zero induced charge along all interfaces, see e.g., the special two-phase case considered in [**22, 23, 62**]. If γ_k is the electrical conductivity, σ_k, of each of the phases, then the second boundary condition in Eq. (3.2) states that the electric current in continuous across the interface. This is the appropriate boundary condition when studying a weakly conducting (leaky dielectric) material such as considered in [**25, 26, 63**]. In this model, there would be induced charge along the interfaces. The charge q is defined as the jump in the normal displacement field across the interface. In general, balancing all stresses across the interface requires the interface to be determined as part of the problem. We will assume that the interface in our case remains planar. Henceforth, we nondimensionlize all variables using the particle radius a is the unit of length, $E_0 a$ is the unit of potential and γ_l as the unit of the material parameter. Accordingly, we introduce the ratios $\gamma_{ul} = \gamma_u/\gamma_l > 1$ and $\gamma_{pl} = \gamma_p/\gamma_l$.. Without loss of generality, we assume $\gamma_u > \gamma_l$.

If the particle were not there, then the solution to (3.1)-(3.2) is simply $\phi_u = z/\gamma_{ul}$ and $\phi_l = z$. But because of the presence of the particle, there is a nonzero perturbation potential Φ_k to the applied uniform electric field in each region that needs to be determined.

Hence we define

$$\varphi_u = z/\gamma_{ul} + \Phi_u, \tag{3.3}$$

$$\varphi_l = z + \Phi_l, \tag{3.4}$$

$$\varphi_p = z + \Phi_p. \tag{3.5}$$

Assuming a uniform applied field, Φ_u and Φ_l decays to 0 as $r^2 + z^2$ tends to infinity. Note that when $\gamma_{ul} \to \infty$, then $\phi_u \to 0$ which corresponds to the water-nonpolar scenario studied in [**62**].

To solve for the perturbation potential in this complicated geometry we utilize a toroidal coordinate system [**22**],

$$z = \frac{r_0 \sin\xi}{\cosh\eta - \cos\xi}, \quad r = \frac{r_0 \sinh\eta}{\cosh\eta - \cos\xi}. \tag{3.6}$$

Figure 3.2 illustrates the relation between the cylindrical and toroidal coordinate systems. The contact line is located at $(r, z) = (r_0, 0)$, where $r_0 = \sin\alpha$, which from Equation (3.6) implies $\eta = \infty$. The z-axis is $\eta = 0$ while the r-axis is $\xi = 0$ outside of the particle, and $\xi = \pi$ inside of the particle. The spherical surface when $z > 0$ is $\xi = \xi_0 = \pi - \alpha$, and it is $\xi = \xi_0 + \pi$ for $z < 0$.

Inserting Eqs. (3.3)-(3.5) into Eq. (3.1), the Laplace equation in toroidal coordinates becomes,

$$\frac{\partial}{\partial\xi}\left(\frac{\sinh\eta}{\cosh\eta - \cos\xi}\frac{\partial\Phi_k}{\partial\xi}\right) + \frac{\partial}{\partial\eta}\left(\frac{\sinh\eta}{\cosh\eta - \cos\xi}\frac{\partial\Phi_k}{\partial\eta}\right) = 0, \tag{3.7}$$

where k=u,l,p. From the boundary conditions in Eq. (3.2), we obtain,

$$\Phi_u\big|_{\xi=0} = \Phi_l\big|_{\xi=2\pi}, \tag{3.8}$$

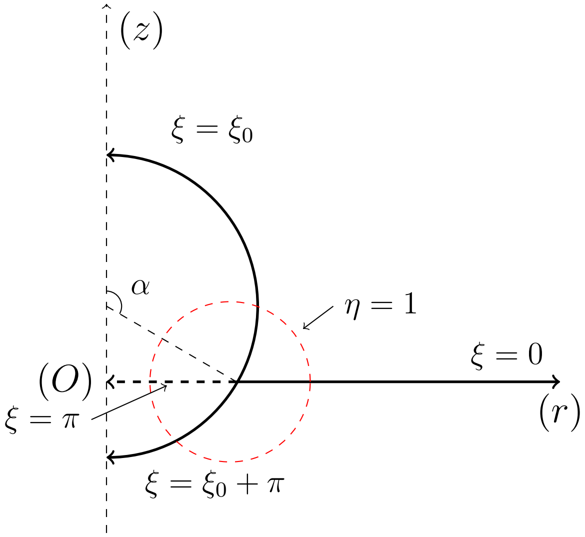

Figure 3.2. Toroidal coordinates system.

$$\Phi_u = \Phi_p + (1 - 1/\gamma_{ul})z \quad \text{at } \xi = \xi_0, \tag{3.9}$$

$$\Phi_l = \Phi_p \quad \text{at } \xi = \xi_0 + \pi. \tag{3.10}$$

And,

$$\gamma_{ul} \frac{\partial \Phi_u}{\partial \xi}\Big|_{\xi=0} = \frac{\partial \Phi_l}{\partial \xi}\Big|_{\xi=2\pi}, \tag{3.11}$$

$$\gamma_{pl} \frac{\partial \Phi_p}{\partial \xi} - \gamma_{ul} \frac{\partial \Phi_u}{\partial \xi} = (1 - \gamma_{pl}) \frac{\partial z}{\partial \xi} \quad \text{at } \xi = \xi_0, \tag{3.12}$$

$$\gamma_{pl} \frac{\partial \Phi_p}{\partial \xi} - \frac{\partial \Phi_l}{\partial \xi} = (1 - \gamma_{pl}) \frac{\partial z}{\partial \xi} \quad \text{at } \xi = \xi_0 + \pi. \tag{3.13}$$

Our solution approach is to apply the Mehler-Fock integral transform (see Appendix B). Let us introduce the solution ansatz,

$$\Phi_k(\eta, \xi) = \sqrt{\cosh \eta - \cos \xi} \int_0^\infty B_k(\xi, \tau) K^0(\eta, \tau) d\tau, \tag{3.14}$$

where $K^0(\eta, \tau) = P^0_{-1/2+i\tau}(\cosh \eta)$ is the associated Legendre function of the first kind of order zero, with complex index $-1/2 + i\tau$. If the square root function were not in Eq.

(3.14), the coefficients $B_k(\xi,\tau)$ would be the Melher-Fock transform of the perturbation potential Φ_k in η.

Using (3.14) in Eq. (3.7), and noting that the Laplace equation is separable, we find that $B_k(\xi,\tau)$ must satisfy,

$$\frac{\partial^2 B_k(\xi,\tau)}{\partial\xi^2} = \tau^2 B_k(\xi,\tau). \tag{3.15}$$

Substitution of (3.14) into the continuity Eqs. (3.8)-(3.10) yields,

$$\int_0^\infty B_u(\xi,\tau)K^o(\eta,\tau)d\tau = \int_0^\infty B_l(\xi,\tau)K^0(\eta,\tau)d\tau \quad \text{at } z=0, \tag{3.16}$$

$$\begin{aligned}\int_0^\infty B_u(\xi,\tau)K^0(\eta,\tau)d\tau = \int_0^\infty & B_p(\xi,\tau)K^0(\eta,\tau)d\tau \\ & + (1-1/\gamma_{ul})\frac{\sin\alpha\sin\xi_0}{(\cosh\eta-\cos\xi_0)^{3/2}} \quad \text{at } \xi=\xi_0,\end{aligned} \tag{3.17}$$

$$\int_0^\infty B_l(\xi,\tau)K^0(\eta,\tau)d\tau = \int_0^\infty B_p(\xi,\tau)K^0(\eta,\tau)d\tau \quad \text{at } \xi=\xi_0+\pi. \tag{3.18}$$

Using the Lebedev formula (Eqn 3.8 in Danov and Kralchevsky [**22**]), the inhomogeneous term in (3.17) can be written in integral form as,

$$\frac{\sin\xi_0}{(\cosh\eta-\cos\xi_0)^{3/2}} = 2^{3/2}\int_0^\infty \tau\frac{\sinh{(\pi-\xi_0)\tau}}{\cosh\pi\tau}K^0(\eta,\tau)d\tau. \tag{3.19}$$

Then Eqs. (3.16)-(3.18) yield,

$$B_u\big|_{\xi=0} = B_l\big|_{\xi=2\pi}, \tag{3.20}$$

$$B_u = B_p + (1-1/\gamma_{ul})2^{3/2}\tau\sin\alpha\frac{\sinh{(\pi-\xi_0)\tau}}{\cosh\pi\tau} \quad \text{at } \xi=\xi_0, \tag{3.21}$$

$$B_l = B_p \quad \text{at } \xi=\xi_0+\pi. \tag{3.22}$$

We can look for a solution to Eq.(3.15) in the general form,

$$B_u = \mathcal{C}_1(\tau)\frac{\sinh(\xi_0-\xi)\tau}{\sinh\xi_0\tau} + \mathcal{C}_2(\tau)\frac{\sinh\xi\tau}{\sinh\xi_0\tau} + f(\xi,\tau), \tag{3.23}$$

$$B_l = \mathcal{C}_1(\tau)\frac{\sinh(\xi_0+\pi-\xi)\tau}{\sinh(\xi_0-\pi)\tau} + \mathcal{C}_3(\tau)\frac{\sinh(\xi-2\pi)\tau}{\sinh(\xi_0-\pi)\tau}, \tag{3.24}$$

$$B_p = \mathcal{C}_2(\tau)\frac{\sinh(\xi_0+\pi-\xi)\tau}{\sinh\pi\tau} - \mathcal{C}_3(\tau)\frac{\sinh(\xi_0-\xi)\tau}{\sinh\pi\tau}, \tag{3.25}$$

where $\mathcal{C}_1(\tau)$, $\mathcal{C}_2(\tau)$ and $\mathcal{C}_3(\tau)$ are undetermined coefficient functions of τ. Substituting back we obtain a problem for $f(\xi,\tau)$, We substitute Eqs.(3.23)-(3.25) back into Eqs. (3.16) and (3.20)-(3.22) to solve the unknown function f. The f problem reduces to,

$$\frac{\partial^2 f(\xi,\tau)}{\partial\xi^2} = \tau^2 f, \tag{3.26}$$

$$f(0,\tau) = 0, \tag{3.27}$$

$$f(\xi_0,\tau) = (1-1/\gamma_{ul})2^{3/2}\tau\sin\alpha\frac{\sinh(\pi-\xi_0)\tau}{\cosh\pi\tau}. \tag{3.28}$$

We can easily obtain the solution of this second order boundary condition problem,

$$f(\xi,\tau) = (1-1/\gamma_{ul})2^{3/2}\tau\sin\alpha\frac{\sinh(\pi-\xi_0)\tau}{\cosh\pi\tau}\frac{\sinh\xi\tau}{\sinh\xi_0\tau}. \tag{3.29}$$

To determine $\mathcal{C}_1(\tau)$, $\mathcal{C}_2(\tau)$ and $\mathcal{C}_3(\tau)$, we substitute Eqs. (3.23)-(3.25) into the other three boundary conditions (3.11)-(3.13). The result is,

$$\begin{aligned}\mathcal{C}_1(\tau)[\gamma_{ul}\coth\xi_0\tau - \coth(\xi_0-\pi)\tau] &= \mathcal{C}_2(\tau)\frac{\gamma_{ul}}{\sinh\xi_0\tau}\\ &- \mathcal{C}_3(\tau)\frac{1}{\sinh(\xi_0-\pi)\tau} + (\gamma_{ul}-1)2^{3/2}\tau\frac{\sinh(\pi-\xi_0)\tau}{\cosh\pi\tau\sinh(\xi_0\tau)}\sin\alpha,\end{aligned} \tag{3.30}$$

$$\gamma_{ul}\int_0^\infty \tau\mathcal{C}_1(\tau)\frac{K^0(\eta,\tau)}{\sinh\xi_0\tau}d\tau - \int_0^\infty \tau\mathcal{C}_2(\tau)[\gamma_{pl}\frac{\cosh\pi\tau}{\sinh\pi\tau} + \gamma_{ul}\frac{\cosh\xi_0\tau}{\sinh\xi_0\tau}]K^0(\eta,\tau)d\tau$$

$$+ \gamma_{pl}\int_0^\infty \tau\mathcal{C}_3(\tau)\frac{K^0(\eta,\tau)}{\sinh\pi\tau}d\tau + (\gamma_{pl}-\gamma_{ul})\frac{\sin\xi_0}{2(\cosh\eta-\cos\xi_0)}\int_0^\infty \mathcal{C}_2(\tau)K^0(\eta,\tau)d\tau$$

$$- \frac{\sin\xi_0}{2(\cosh\eta-\cos\xi_0)}\int_0^\infty (\gamma_{ul}-1)2^{3/2}\tau\sin\alpha\frac{\sinh(\pi-\xi_0)\tau}{\cosh\pi\tau}K^0(\eta,\tau)d\tau$$

$$= \int_0^\infty (\gamma_{ul}-1)2^{3/2}\tau^2\sin\alpha\frac{\sinh(\pi-\xi_0)\tau}{\cosh\pi\tau}\frac{\cosh\xi_0\tau}{\sinh\xi_0\tau}K^0(\eta,\tau)d\tau$$

$$+ \frac{2^{3/2}}{3}(1-\gamma_{pl})\sin\alpha\int_0^\infty [\tau\cot\xi_0\frac{\sinh(\pi-\xi_0)\tau}{\cosh\pi\tau} - 2\tau^2\frac{\cosh(\pi-\xi_0)\tau}{\cosh\pi\tau}]K^0(\eta,\tau)d\tau, \tag{3.31}$$

$$\int_0^\infty \tau\mathcal{C}_1(\tau)\frac{K^0(\eta,\tau)}{\sinh(\xi_0-\pi)\tau}d\tau - \int_0^\infty \tau\mathcal{C}_3(\tau)[-\gamma_{pl}\frac{\cosh\pi\tau}{\sinh\pi\tau} + \frac{\cosh(\xi_0-\pi)\tau}{\sinh(\xi_0-\pi)\tau}]K^0(\eta,\tau)d\tau$$

$$- \gamma_{pl}\int_0^\infty \tau\mathcal{C}_2(\tau)\frac{K^0(\eta,\tau)}{\sinh\pi\tau}d\tau + (\gamma_{pl}-1)\frac{\sin(\xi_0+\pi)}{2(\cosh\eta-\cos(\xi_0+\pi))}\int_0^\infty \mathcal{C}_3(\tau)K^0(\eta,\tau)d\tau$$

(3.32)

$$= \frac{2^{3/2}}{3}(1-\gamma_{pl})\sin\alpha\int_0^\infty [-\tau\cot(\xi_0+\pi)\frac{\sinh\xi_0\tau}{\cosh\pi\tau} - 2\tau^2\frac{\cosh\xi_0\tau}{\cosh\pi\tau}]K^0(\eta,\tau)d\tau.$$

If equations (3.30)-3.32) were solved numerically, the results could be substituted back in (3.14),(3.23)-(3.25) and then integrated to find the electric field. But there is a difficulty. Although equations (3.30)-(3.32) are three equations for the three unknowns $\mathcal{C}_k(k = 1,2,3)$ with equation (3.30) algebraic, equation (3.31)-(3.32) only contain the unknowns in the integrand, similar to a Fredholm integral system of the first kind. Such systems are difficult to solve, and often ill-posed. To identify a system that behaves better under numerical solution, we apply the generalized inverse Mehler Transformation to (3.30)-(3.32) (see Section 3.2.3) resulting in a Fredholm-like system of the second kind.

3.2.2. Applied Tangential Field

Her let us consider the case where a uniform electric field is applied tangentially to the planar interface between Ω_l and Ω_u in the x direction. In the absence of a particle, the solution is $\vec{E} = -E_0\hat{x}$ in both phases, i.e., a uniform constant field in the x direction. The presence of the particle perturbs this solution. Paralleling the argument for the normal applied field and again introducing dimensionless variables, we look for a solution in cylindrical coordinates of Eqs. (3.1)-(3.2) in the form,

$$\varphi_k = r\cos\theta + \Phi_k, \tag{3.33}$$

where k denotes u, l, p respectively.

Our solution approach will again be to introduce the toroidal coordinate system (3.6). The difference is that now our solution is not axisymmetric and we must account for the θ dependence of the solution.

The Laplace equation for the perturbed potential Φ in toroidal coordinates (ξ, η, θ) with θ as the azimuthal angle, becomes,

$$\begin{aligned}\frac{\partial}{\partial\xi}\left(\frac{\sinh\eta}{\cosh\eta-\cos\xi}\frac{\partial\Phi_k}{\partial\xi}\right)+\frac{\partial}{\partial\eta}\left(\frac{\sinh\eta}{\cosh\eta-\cos\xi}\frac{\partial\Phi_k}{\partial\eta}\right)\\ +\frac{1}{\sinh\eta(\cosh\eta-\cos\xi)}\frac{\partial^2\Phi_k}{\partial\theta^2}=0.\end{aligned} \tag{3.34}$$

The boundary conditions (3.2) can be written as

$$\Phi_u = \Phi_l \quad \text{at } z = 0, \tag{3.35}$$

$$\Phi_u = \Phi_p \quad \text{at } \xi = \xi_0, \tag{3.36}$$

$$\Phi_l = \Phi_p \quad \text{at } \xi = \xi_0 + \pi, \tag{3.37}$$

$$\gamma_{ul}\frac{\partial \Phi_u}{\partial \xi} = \frac{\partial \Phi_l}{\partial \xi} \quad \text{at } z = 0, \tag{3.38}$$

$$\gamma_{ul}\frac{\partial \Phi_u}{\partial \xi} - \gamma_{pl}\frac{\partial \Phi_p}{\partial \xi} = (\gamma_{ul} - \gamma_{pl})\frac{\sin\alpha \sinh\eta \sin\xi_0}{(\cosh\eta - \cos\xi_0)^2}\cos\theta \quad \text{at } \xi = \xi_0, \tag{3.39}$$

$$\frac{\partial \Phi_l}{\partial \xi} - \gamma_{pl}\frac{\partial \Phi_p}{\partial \xi} = (1 - \gamma_{pl})\frac{-\sin\alpha \sinh\eta \sin\xi_0}{(\cosh\eta + \cos\xi_0)^2}\cos\theta \quad \text{at } \xi = \xi_0 + \pi. \tag{3.40}$$

Paralleling the argument in the previous section, and noting that our solution must be symmetric about the x-axis, we can look for a solution in the form

$$\Phi_k(\eta, \xi, \theta) = \sqrt{\cosh\eta - \cos\xi}\,\Psi_k(\eta, \xi)\cos(\theta). \tag{3.41}$$

Substituting (3.41) into Eq. (3.34) we find that Ψ satisfies the equation

$$\frac{1}{\sinh\eta}\frac{\partial}{\partial\eta}(\sinh\eta\frac{\partial \Psi_k}{\partial \eta}) + \Psi_k(\frac{1}{4} - \frac{1}{\sinh^2\eta}) + \frac{\partial^2 \Psi_k}{\partial \xi^2} = 0. \tag{3.42}$$

This is the first order associate Legendre equation of the first kind. Thus Ψ_k can be expressed by,

$$\Psi_k(\eta, \xi) = \int_0^\infty B_k(\xi, \tau)P^1_{-1/2+i\tau}(\cosh\eta)d\tau, \tag{3.43}$$

where $P^1_{-1/2+i\tau}$ is the first order associate Legendre function of the first kind. B_k satisfy,

$$\frac{\partial^2 B_k(\xi, \tau)}{\partial \xi^2} = \tau^2 B_k. \tag{3.44}$$

We can look for a solution in the form,

$$B_u = \mathcal{C}_1(\tau)\frac{\sinh{(\xi_0 - \xi)\tau}}{\sinh\xi_0\tau} + \mathcal{C}_2(\tau)\frac{\sinh\xi\tau}{\sinh\xi_0\tau} \tag{3.45}$$

$$B_l = \mathcal{C}_1(\tau)\frac{\sinh{(\xi_0 + \pi - \xi)\tau}}{\sinh{(\xi_0 - \pi)\tau}} + \mathcal{C}_3(\tau)\frac{\sinh{(\xi - 2\pi)\tau}}{\sinh{(\xi_0 - \pi)\tau}} \tag{3.46}$$

$$B_p = \mathcal{C}_2(\tau)\frac{\sinh{(\xi_0 + \pi - \xi)\tau}}{\sinh\pi\tau} - \mathcal{C}_3(\tau)\frac{\sinh{(\xi_0 - \xi)\tau}}{\sinh\pi\tau}. \tag{3.47}$$

This will naturally satisfy the continuity of Φ_k conditions. Paralleling the derivations of equations (3.30)-3.32), we substitute the above equations for B_k into the second boundary condition in Eqs. (3.38)-(3.40) and find that the three coefficients $\mathcal{C}_k$ must satisfy the three equations,

$$\mathcal{C}_1(\tau)[\gamma_{ul}\coth\xi_0\tau-\coth{(\xi_0-\pi)\tau}]=\mathcal{C}_2(\tau)\frac{\gamma_{ul}}{\sinh\xi_0\tau}-\mathcal{C}_3(\tau)\frac{1}{\sinh{(\xi_0-\pi)\tau}}, \tag{3.48}$$

$$\begin{aligned}&\gamma_{ul}\int_0^\infty\tau\mathcal{C}_1(\tau)\frac{K^1(\eta,\tau)}{\sinh\xi_0\tau}d\tau-\int_0^\infty\tau\mathcal{C}_2(\tau)[\gamma_{pl}\frac{\cosh\pi\tau}{\sinh\pi\tau}+\gamma_{ul}\frac{\cosh\xi_0\tau}{\sinh\xi_0\tau}]K^1(\eta,\tau)d\tau\\&+\gamma_{pl}\int_0^\infty\tau\mathcal{C}_3(\tau)\frac{K^1(\eta,\tau)}{\sinh\pi\tau}d\tau+(\gamma_{pl}-\gamma_{ul})\frac{\sin\xi_0}{2(\cosh\eta-\cos\xi_0)}\int_0^\infty\mathcal{C}_2(\tau)K^1(\eta,\tau)d\tau\\&=\frac{2^{5/2}}{3}(\gamma_{ul}-\gamma_{pl})\int_0^\infty\tau\sin\alpha\frac{\sinh{(\pi-\xi_0)\tau}}{\cosh\pi\tau}K^1(\eta,\tau)d\tau,\end{aligned} \tag{3.49}$$

$$\begin{aligned}&\int_0^\infty\tau\mathcal{C}_1(\tau)\frac{K^1(\eta,\tau)}{\sinh{(\xi_0-\pi)\tau}}d\tau-\int_0^\infty\tau\mathcal{C}_3(\tau)[-\gamma_{pl}\frac{\cosh\pi\tau}{\sinh\pi\tau}+\frac{\cosh{(\xi_0-\pi)\tau}}{\sinh{(\xi_0-\pi)\tau}}]K^1(\eta,\tau)d\tau\\&-\gamma_{pl}\int_0^\infty\tau\mathcal{C}_2(\tau)\frac{K^1(\eta,\tau)}{\sinh\pi\tau}d\tau+(\gamma_{pl}-1)\frac{\sin{(\xi_0+\pi)}}{2(\cosh\eta-\cos{(\xi_0+\pi)})}\int_0^\infty\mathcal{C}_3(\tau)K^1(\eta,\tau)d\tau\\&=\frac{2^{5/2}}{3}(\gamma_{pl}-1)\int_0^\infty\tau\sin\alpha\frac{\sinh\xi_0\tau}{\cosh\pi\tau}K^1(\eta,\tau)d\tau,\end{aligned} \tag{3.50}$$

where $K^1(\eta,\tau)=P^1_{-1/2+i\tau}(\cosh\eta)$. Here we have used the identity,

$$\frac{\sinh\eta\sin\xi_0}{(\cosh\eta-\cos\xi_0)^{5/2}}=-\frac{2^{5/2}}{3}\int_0^\infty\tau\frac{\sinh{(\pi-\xi_0)\tau}}{\cosh\pi\tau}K^1(\eta,\tau)d\tau. \tag{3.51}$$

This identity can be easily derived by taking the derivative with respect to η of the Lebedev formula (3.19). As with the normal field case, we solve the above systems of equations for $\mathcal{C}_k$ numerically. Note that we have retained similar notation in solving the applied normal field and tangential field case and we expect that the context of the discussion will eliminate any potential confusion (between normal and tangential field).

3.2.3. Solving integral equations

To solve the integral equations for both the normal and tangential field cases above, we apply the generalized inverse Mehler transform in Appendix B.

For the normal field case the inverse transform is applied to equations (3.31)-(3.32). From the resulting equations, eliminating $\mathcal{C}_1$ by using (3.30) and with some algebraic manipulation, we obtain the coupled system of integral equations,

$$\mathcal{C}_2 A_{21}(\tau) + \mathcal{C}_3 A_{31}(\tau) = S_1(\tau) + (\gamma_{ul} - \gamma_{pl}) \int_0^\infty \mathcal{C}_2(\tilde{\tau}) V_1(\tilde{\tau}, \tau) d\tilde{\tau}, \tag{3.52}$$

$$\mathcal{C}_2 A_{22}(\tau) + \mathcal{C}_3 A_{32}(\tau) = S_2(\tau) + (1 - \gamma_{pl}) \int_0^\infty \mathcal{C}_3(\tilde{\tau}) V_2(\tilde{\tau}, \tau) d\tilde{\tau}. \tag{3.53}$$

See Appendix C for the detailed results including the definitions of V_k and S_k.

Equations (3.52)-(3.53) are a system of two linear Fredholm integral equations of the second kind for the unknown coefficients $\mathcal{C}_2$ and $\mathcal{C}_3$. A solution is found computationally by discretizing the integrals using the trapezoidal rule and solving the resulting discretized system of equations. Let T_τ be the truncation point of τ and $\tilde{\tau} \gg 1$, and T_η be the truncation point of η. The term in righthand side is a triple integral in the first quadrant. Since we require the functions $\mathcal{C}_1, \mathcal{C}_2$ and $\mathcal{C}_3$ decays sufficiently fast and the fact that Legendre function $K^0(\eta, \tau) = P^0_{-1/2+i\tau}(\cosh \eta)$ also decays exponentially when $\eta \to \infty$, the truncation error is small at large enough T_τ and T_η. Numerical checks are done to ensure convergence (see Appendix D). The unknown coefficient $\mathcal{C}_1$ can be found from Eq. (3.48) after $\mathcal{C}_2$ and $\mathcal{C}_3$ are found. The perturbation potentials Φ_k are then determined by using Eqs. (3.14), (3.23)-(3.25).

The tangential field problem is solved in a similar way by applying the transform Eq. (B.4) to Eq. (3.49)-(3.50),

$$\begin{aligned}
&\gamma_{ul}\mathcal{C}_1(\tau)\frac{1}{\sinh\xi_0\tau} - \mathcal{C}_2(\tau)[\gamma_{pl}\coth\pi\tau + \gamma_{ul}\coth\xi_0\tau] \\
&\quad + \gamma_{pl}\mathcal{C}_3(\tau)\frac{1}{\sinh\pi\tau} \\
&\quad =(\gamma_{ul}-\gamma_{pl})\frac{2^{5/2}}{3}\frac{\sinh{(\pi-\xi_0)\tau}}{\cosh\pi\tau} \\
&\quad + (\gamma_{ul}-\gamma_{pl})\frac{2\tanh\pi\tau}{4\tau^2+1}\sin\xi_0\int_0^\infty \mathcal{C}_2(\tilde{\tau})U_1^1(\tilde{\tau},\tau)d\tilde{\tau}, \qquad (3.54)
\end{aligned}$$

and

$$\begin{aligned}
&\mathcal{C}_1(\tau)\frac{1}{\sinh{(\xi_0-\pi)\tau}} - \mathcal{C}_3(\tau)[-\gamma_{pl}\coth\pi\tau + \coth{(\xi_0-\pi)\tau}] \\
&\quad - \gamma_{pl}\mathcal{C}_2(\tau)\frac{1}{\sinh\pi\tau} \\
&\quad =\frac{2^{5/2}}{3}(\gamma_{pl}-1)\frac{\sinh\xi_0\tau}{\cosh\pi\tau} \\
&\quad + (1-\gamma_{pl})\frac{2\tanh\pi\tau}{4\tau^2+1}\sin{(\xi_0+\pi)}\int_0^\infty \mathcal{C}_3(\tilde{\tau})U_2^1(\tilde{\tau},\tau)d\tilde{\tau}, \qquad (3.55)
\end{aligned}$$

where

$$U_1^1(\tilde{\tau}, \tau) = \int_0^\infty \frac{K^1(\eta, \tau)K^1(\eta, \tilde{\tau})}{\cosh \eta - \cos \xi_0} \sinh \eta d\eta, \tag{3.56}$$

$$U_2^1(\tilde{\tau}, \tau) = \int_0^\infty \frac{K^1(\eta, \tau)K^1(\eta, \tilde{\tau})}{\cosh \eta + \cos \xi_0} \sinh \eta d\eta. \tag{3.57}$$

Combinding Eqs. (3.48), (3.54) and (3.55), the tangential field problem can be solved in a numerical manner similar to the normal field problem.

3.3. Computational Results: Induced Potential Lines

Computation results for the applied normal and tangential field cases are presented here. The parameters which affect the potential solution are the contact angle α, and the ratios γ_{pl} and γ_{ul}.

Figure 3.3 and fig. 3.4 show the equipotential lines of several different scenarios under a given parameter set. For $\alpha = \pi/2$, $\gamma_{ul} = 4$ and $\gamma_{pu} = 1/2$, we see in Figure 3.3a that a particle in an applied normal field behaves like a dipole, while for $\gamma_{pu} = 2$, in Figure 3.3b, the quadrupole nature of the perturbation field is apparent. Results for the same parameters are given for the applied tangential field case in fig. 3.4 as γ_{pu} is increased. In fig. 3.4 the potential in Eq. (3.41) is plotted without the $\cos\theta$ dependence. This quadrupole contribution is explicitly derived in Section 3.6 where we calculate the far field behavior of the potential.

3.4. Electric Field Near the Contact Line

To study the local behavior of the electric field near the contact line $(r_0, 0)$, we consider the limit $\eta \to \infty$. Here we only provide deatils for the case of the applied normal field.

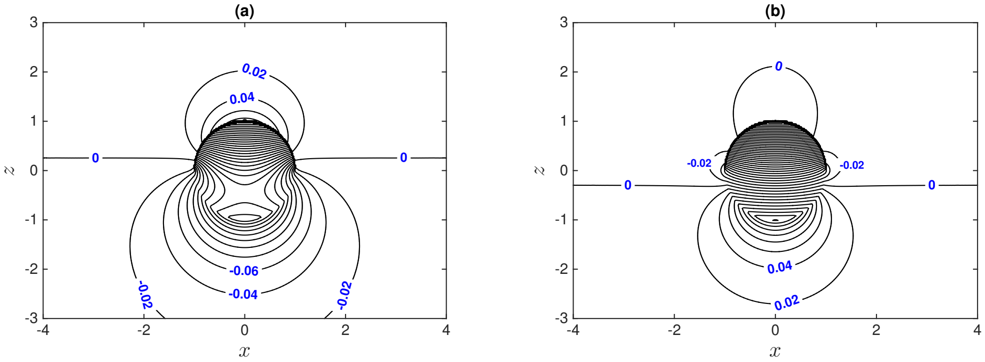

Figure 3.3. Applied normal electric field. Equal potential lines of Φ_k, $\alpha = \pi/2$, $\gamma_{ul} = 4$. (a) $\gamma_{pl} = 1/2$. (b) $\gamma_{pl} = 2$, for better demonstration, smaller potential level is used. Select values of the potential are noted on each figure.

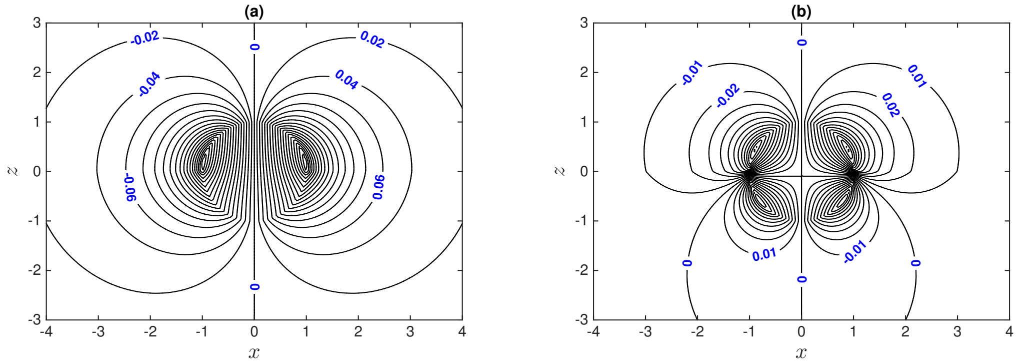

Figure 3.4. Applied tangential electric field. Equal potential lines of Φ_k, $\alpha = \pi/2$, $\gamma_{ul} = 4$. (a) $\gamma_{pl} = 1/2$. (b) $\gamma_{pl} = 2$, for better demonstration, smaller potential level is used. Select values of the potential are noted on each figure.

Denote the solution to system Eqs. (3.7)-(3.13) as,

$$\Phi_k(\eta, \xi) = \sqrt{\cosh\eta - \cos\xi}\,\Psi_k(\eta, \xi). \tag{3.58}$$

Since the potential is finite at the contact line, it follows that as $\eta \to \infty$, $\Psi_k(\eta, \xi)$ satisfies following equation and boundary conditions,

$$\frac{\partial^2 \Psi_k}{\partial \eta^2} + \frac{\partial \Psi_k}{\partial \eta} + \frac{\Psi_k}{4} + \frac{\partial^2 \Psi_k}{\partial \xi^2} = 0, \tag{3.59}$$

where $k = u, l, p$. And,

$$\Psi_u = \Psi_l \quad \text{at } z = 0, \tag{3.60}$$

$$\Psi_u = \Psi_p \quad \text{at } \xi = \xi_0, \tag{3.61}$$

$$\Psi_l = \Psi_p \quad \text{at } \xi = \xi_0 + \pi, \tag{3.62}$$

and,

$$\gamma_{ul}\frac{\partial \Psi_u}{\partial \xi} = \frac{\partial \Psi_l}{\partial \xi} \quad \text{at } z = 0, \tag{3.63}$$

$$\gamma_{pl}\frac{\partial \Psi_p}{\partial \xi} = \gamma_{ul}\frac{\partial \Psi_u}{\partial \xi} \quad \text{at } \xi = \xi_0, \tag{3.64}$$

$$\gamma_{pl}\frac{\partial \Psi_p}{\partial \xi} = \frac{\partial \Psi_l}{\partial \xi} \quad \text{at } \xi = \xi_0 + \pi. \tag{3.65}$$

This suggests a solution near the contact line in the form $\Psi_k = D_0 e^{-\eta/2} + \psi_k(\eta, \xi)$. We look for $\psi_k(\eta, \xi)$ as a separable function of η and ξ. The result which satisfies the continuity of potential Eq.(3.60)-(3.62) is

$$\psi_u = e^{(-1/2-\nu)\eta}[D_1\frac{\sin{(\xi_0 - \xi)\nu}}{\sin{\xi_0\nu}} + D_2\frac{\sin{\xi\nu}}{\sin{\xi_0\nu}}], \tag{3.66}$$

$$\psi_l = e^{(-1/2-\nu)\eta}[D_1\frac{\sin{(\xi_0 + \pi - \xi)\nu}}{\sin{(\xi_0 - \pi)\nu}} + D_3\frac{\sin{(\xi - 2\pi)\nu}}{\sin{(\xi_0 - \pi)\nu}}], \tag{3.67}$$

$$\psi_p = e^{(-1/2-\nu)\eta}[D_2\frac{\sin{(\xi_0 + \pi - \xi)\nu}}{\sin{\pi\nu}} + D_3\frac{\sin{(\xi - \xi_0)\nu}}{\sin{\pi\nu}}]. \tag{3.68}$$

Recall that $\xi = 0$ on the Ω_u side of the planar interface while $\xi = 2\pi$ on the Ω_l side of the planar interface.

The separation parameter $\nu > 0$ is determined by the other three boundary conditions. Substituting the local solution Eq. (3.66)-(3.68) into Eqs. (3.63)-(3.65), we obtain three homogeneous linear equations for the coefficients D_1, D_2, D_3. A non-trivial solution of the

3×3 linear system requires the following determinant must be zero,

(3.69)

$$\begin{vmatrix} -\gamma_{ul}\cot\xi_0\nu + \cot(\xi_0-\pi)\nu & \gamma_{ul}\csc\xi_0\nu & -\csc(\xi_0-\pi)\nu \\ -\gamma_{ul}\csc\xi_0\nu & \gamma_{ul}\cot\xi_0\nu + \gamma_{pl}\cot\pi\nu & -\gamma_{pl}\csc\pi\nu \\ -\csc(\xi_0-\pi)\nu & \gamma_{pl}\csc\pi\nu & \cot(\xi_0-\pi)\nu - \gamma_{pl}\cot\pi\nu \end{vmatrix} = 0.$$

Eq. (3.69) determines the separation parameter ν, and therefore the singular behavior of the electric field as a function of the γ ratios and $\alpha = \pi - \xi_0$. There are multiple real solutions of Eq. (3.69) but the smallest solution is always in the interval $[\frac{1}{2}, 1]$. This implies an integrable singularity of the normal electric field (see Eq. (3.73)). Figure 3.5 shows the behavior of the smallest ν from Eq. (3.69) as a function of the contact angle α for different values of γ_{ul} when $\gamma_{pl} = 1$. It is interesting to note that as α increases from 0, the value of ν first decreases from $\nu = 1$, reaches a minimum, and finally approaches one as α tends to 180°.

First let us consider the limit where $\gamma_{ul} \to \infty$, e.g., when the upper fluid is a perfect conductor. In this limiting case the determinant (3.69) reduces to

$$\cot(\xi_0 - \pi)\nu - \gamma_{pl}\cot\pi\nu = 0. \tag{3.70}$$

This is consistent with the results of [**62**] and the monotonically decreasing behavior of ν shown in Figure 3.5. Note this asymptotic result implies that ν tends to 1 as $\alpha = \pi - \xi_0$ tends to zero, and it implies that ν tends to $1/2$ as α tends to 180°, indicating a singular limit as illustrated in Figure 3.5.

We note when $\xi_0 = \pi/2$, the solution of ν becomes identical to the solution in checkerboard geometry [**64, 65**] when the conductivities in the left half plane are the same, where

ν satisfies,

$$\cos\pi(1-\nu) = 1 - 2\Delta^2, \quad \Delta^2 = \frac{\gamma_p(\gamma_l-\gamma_u)^2}{2(\gamma_u+\gamma_l)(\gamma_u+\gamma_p)(\gamma_p+\gamma_l)}. \tag{3.71}$$

Once the potential in the neighborhood of the contact line is known, we find the electric field by taking the gradient of the potential and then letting η tend to infinity. We need to only consider the electric field in the upper fluid, and for ease of presentation we only look for the singular behavior of $\vec{E}_u$ along $z=0$. Suppose we write $\vec{E}_u = E_z\vec{z} + E_r\vec{r}$ along $z=0$.

$$E_z|_{z=0} = -\frac{1}{\gamma_{ul}} - \frac{\partial\Phi_u}{\partial z}|_{z=0} = -\frac{1}{\gamma_{ul}} - (\cosh\eta-1)^{3/2}\frac{\partial\Psi_u}{\partial\xi}|_{\xi=0}, \tag{3.72}$$

using Eq. (3.66) with only the smallest $\nu \in [\frac{1}{2}, 1]$, and the definition of the toroidal coordinate system Eq. (3.6), we obtain at leading order for large η

$$E_z|_{z=0} \sim c_n(\nu)e^{(1-\nu)\eta} \sim \tilde{c}_n(\nu)(r/r_0-1)^{\nu-1}. \tag{3.73}$$

Here $c_n(\nu)$ and $\tilde{c}_n(\nu)$ are coefficients which do not depend on η, and note that from Eq. (3.6) that as $\eta\to\infty$, then $r\to r_0$. Since ν is between 1/2 and 1, the singularity in the normal electric field is integrable.

The above asymptotic analysis allows us to also find the local behavior of the electric field E_r at the contact line as $\eta\to\infty$,

$$E_r|_{z=0} \sim \frac{D_0}{2} - \nu D_1 e^{(1-\nu)\eta} \sim \frac{D_0}{2} - \nu D_1\left(\frac{r/r_0-1}{2}\right)^{\nu-1} \tag{3.74}$$

Unlike the studies done by Danov and Kralchevsky [**22, 62, 66**] which are in the limit where $\gamma_{ul}\to\infty$, i.e., the upper fluid is a perfect conductor with $E_r = 0$ along the interface, we find here that the tangential electric field is nonzero along the interface and it is singular at the contact line.

The local behavior of the electric field along $z = 0$ at the contact line can also be investigated in the applied tangential field case by a similar analysis. Although the solution in this case does depend on the azimuthal angle θ, the singular behavior does not and the local dependence on r at the contact line is exactly the same as the results above. The assumption of setting $z = 0$ can be relaxed and the functional dependence on position $(r/r_0 - 1)^{\nu-1}$ in Eq. (3.72)-(3.74) can be shown to simply change to $[(z/r_0)^2 + (r/r_0 - 1)^2/4]^{(\nu-1)/2}$.

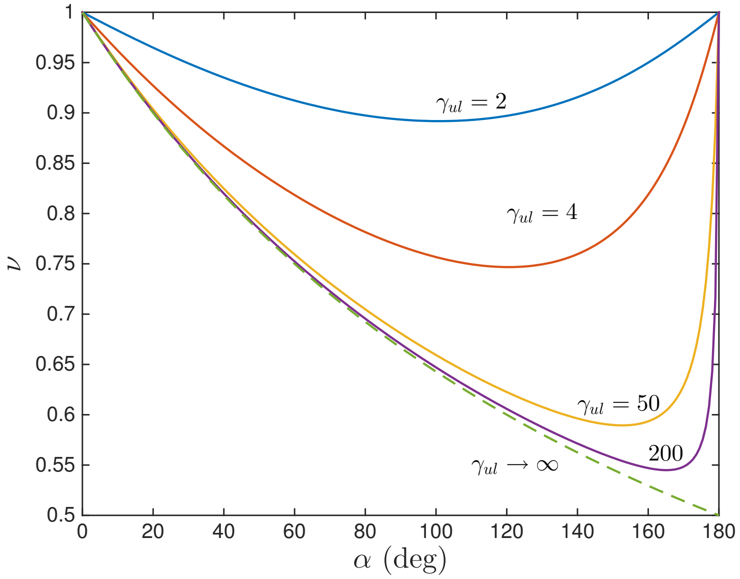

Figure 3.5. ν vs. α for different values of γ_{ul} with $\gamma_{pl} = 1$. Here α is given in degrees. The $\gamma_{ul} \to \infty$ limit recovers the case considered in the study done by Danov and Kralchevsky.

3.5. Electric Force on An Isolated Particle

Here we calculate the total force exerted on the particle by the electric field. Details are only given for the applied normal field case. The applied tangential field case is similar in derivation. The calculation involves integration of the Maxwell stress tensor over the surface of the particle. This tensor depends on the dielectric constants, $\epsilon_k(k = u, l)$, and the electric field on the particle surface. For the sake of brevity, we illustrate the approach on the case of perfect dielectric media, $\gamma_k \equiv \epsilon_k$. The derivation for the leaky dielectrics is similar..

It should be noted that an alternative approach in finding the force on the particle was used by Danov & Kralchevsky [**22**] for the special case of a nonpolar/water (perfect conductor) interface. In that work, the integral of the Maxwell Stress tensor over the particle surface was replaced by an integral along the fluid interface by using the Divergence theorem. This approach could be used in the case of perfect dielectrics, $\gamma = \epsilon$. However, the approach is inapplicable in the case of leaky dielectric, $\gamma = \sigma$ because of nonzero induced charge at the fluid interface.

3.5.1. Applied Normal Electric Field

From symmetry, the net force on the particle is only in the vertical direction. The total force on the particle, $\mathbf{F} = \mathbf{F}^l + \mathbf{F}^u$, is calculated by integrating the total pressure on the particle surface $S = S_u \cup S_l$.

$$\mathbf{F}^k = -\iint_{S_k} \mathbf{P}^k d\mathbf{S}, \tag{3.75}$$

where $k = l, u$. The pressures $\mathbf{P}^k$ in each fluid media is given by the sum of the Maxwell stress tensor $\mathbf{\Sigma}^k$ and the base pressure $p_{k\infty}$,

$$\mathbf{P}^k = p_{k\infty}\mathbf{I} - \mathbf{\Sigma}^k = (p_{k\infty} + \frac{\epsilon_k}{8\pi}|\nabla\varphi_k|^2)\mathbf{I} - \frac{\epsilon_k}{4\pi}\nabla\varphi_k\nabla\varphi_k. \tag{3.76}$$

The force $\mathbf{F}^k$ is assumed to be dimensionless and the unit of force is $\epsilon_0 E_0^2 a^2$, where ϵ_0 is the vacuum permittivity. The constant dimensionless pressure is derived by balancing the pressure at the flat (and particle-free) fluid-fluid interface and is given by

$$p_{u\infty} = p_{l\infty} + \frac{\epsilon_u}{8\pi\gamma_{ul}^2} - \frac{\epsilon_l}{8\pi} = p_{l\infty} + \delta p, \tag{3.77}$$

where $p_{k\infty}$ are constants and δp is the pressure jump from the lower to the upper surface due to the presence of the electric field. Since the constant pressure contribution integrates to zero over S, the total force on the particle can be written as just an integral of δp over S_u plus the Maxwell stress tensor over the particle interfaces,

$$\mathbf{F} = -\iint_{S_u}\{\delta p + \frac{\epsilon_u}{8\pi}|\nabla\varphi_u|^2\mathbf{I} - \frac{\epsilon_u}{4\pi}\nabla\varphi_u\nabla\varphi_u\}d\mathbf{S} - \iint_{S_l}\{\frac{\epsilon_l}{8\pi}|\nabla\varphi_l|^2\mathbf{I} - \frac{\epsilon_l}{4\pi}\nabla\varphi_l\nabla\varphi_l\}d\mathbf{S}. \tag{3.78}$$

The surface integrals on the right hand side of (3.78) will be calculated numerically on the particle interfaces(trapezoidal rule for $\xi = \xi_0$, and $\xi_0 + \pi$) using the solution from Section 4. Since there is only a component of force in the z-direction, introduce $\epsilon_l \mathcal{F}^{\mathcal{S}} = \mathbf{F}\cdot\mathbf{e_z}$ as the z component of the force, where $\mathbf{e_z}$ is the unit vector in the z direction.

Figure 3.6(a) shows the force coefficients $\mathcal{F}^{\mathcal{S}}$ varying with ϵ_{pl} when α is 90 degrees. We find that $\mathcal{F}^{\mathcal{S}}$ is monotonically decreasing with ϵ_{pl}. The force is positive (upward) for small ϵ_{pl}, while it becomes negative as ϵ_{pl} increases. This force is usually referred to as electro-dipping if it is directed to the region of larger dielectric constant. As expected, for

$\epsilon_{ul} = 1$, the net force on the particle is zero independent of the value of ϵ_{pl}. Figure 3.6(b) illustrates the dependence of the force on the contact angle. Note the non-monotonic behavior and also note that both a positive and negative force can be found.

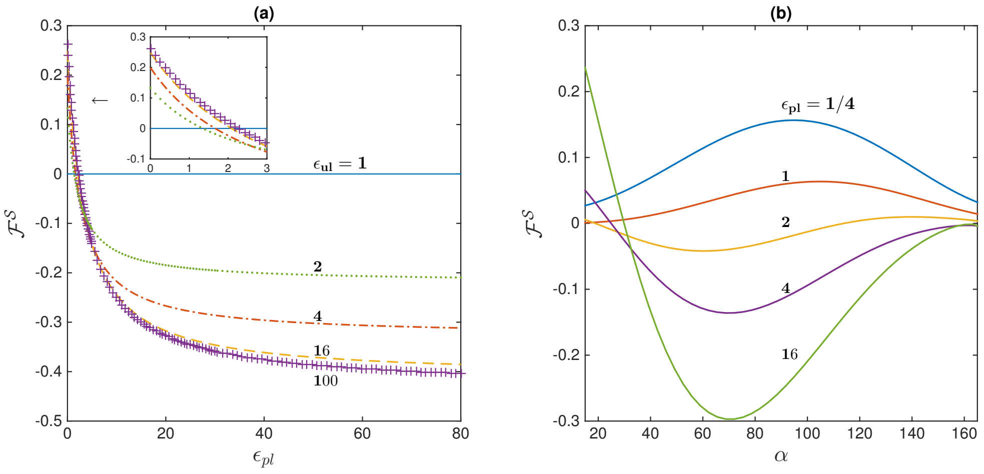

Figure 3.6. In applied normal field. Here $\gamma = \epsilon$. (a) $\mathcal{F}^{\mathcal{S}}$ vs. ϵ_{pl}, when $\epsilon_{ul} = 1, 2, 4, 16, 100$. $\alpha = \pi/2$. (b) $\mathcal{F}^{\mathcal{S}}$ vs. α. $\epsilon_{ul} = 4$, $\epsilon_{pl} = 1/4, 1, 2, 4, 16$.

3.5.2. Applied Tangential Electric Field

While it is obvious from symmetry considerations that there is no net tangential force on a particle in an applied normal electric field, a tangential force might appear to be possible in the tangentially applied field case. Given the tangential field in x direction as in (section 3.2.2), it is straightforward to show that there is no force effect in the tangential direction for a single particle, no matter what materials are chosen or the contact angle. This is due to the symmetry of the field and the particle geometry.

When an applied tangential field in in the x direction, the electric potential is given by (3.33). The force on the particle is given by (3.75) along with (3.76). By symmetry, the next force in the y direction must be zero. The force in the x direction on the upper part of the particle, F_x^u can be written as

$$F_x^u = \iint_{S_u} \mathbf{P}^u d\mathbf{S} \cdot \hat{x} = \iint_{S_u} [P_{11}^u n_1 + P_{12}^u n_2 + P_{13}^u n_3]\, dA, \tag{3.79}$$

where the unit normal to the particle interface is $\mathbf{n} = (n_1, n_2, n_3)$ and $d\mathbf{S} = \mathbf{n}dA$ is the area element. From (3.76) the components of the tensor $\mathbf{P}^u$ are given by

$$P_{11}^u = p_{u\infty} + \frac{\epsilon_u}{8\pi}[-(1 + \frac{\partial \Phi_u}{\partial x})^2 + (\frac{\partial \Phi_u}{\partial y})^2 + (\frac{\partial \Phi_u}{\partial z})^2], \tag{3.80}$$

$$P_{12}^u = \frac{\epsilon_u}{4\pi}(1 + \frac{\partial \Phi_u}{\partial x})\frac{\partial \Phi_u}{\partial y}, \tag{3.81}$$

$$P_{13}^u = \frac{\epsilon_u}{4\pi}(1 + \frac{\partial \Phi_u}{\partial x})\frac{\partial \Phi_u}{\partial z}. \tag{3.82}$$

Notice from Eqs. (3.33) and (3.41) that ϕ_u and Φ_u are odd about the x-axis, i.e., $\Phi_k(x, y, z) = -\Phi_k(-x, y, z)$. This implies that P_{11} is even, while P_{12} and P_{13} are odd. Since the particle is a sphere, n_1 is odd about the x-axis, while n_2 and n_3 are even. Together these imply that $F_x^u = 0$, and a similar derivation gives $F_x^l = 0$.

However, there is a nonzero force in the normal direction which is calculated by using eq. (3.78), note that now $\delta p = 0$. The normal force coefficient $\mathcal{F}^{\mathcal{S}}$ is plotted in Figure 3.7 for some typical values of the parameters. Note in Figure 3.7a that now, for small ϵ_{pl} the force in downward, and increases to a net positive force as ϵ_{pl} increases. The behavior of the force as a function of α is plotted in Figure 3.7b and we see that the qualitative behavior is similar to the applied normal field case, except now the mean values of $\mathcal{F}^{\mathcal{S}}$ will increase with ϵ_{pl} as opposed to the mean decreasing of $\mathcal{F}^{\mathcal{S}}$ observed in the applied normal field case of Figure 3.6a.

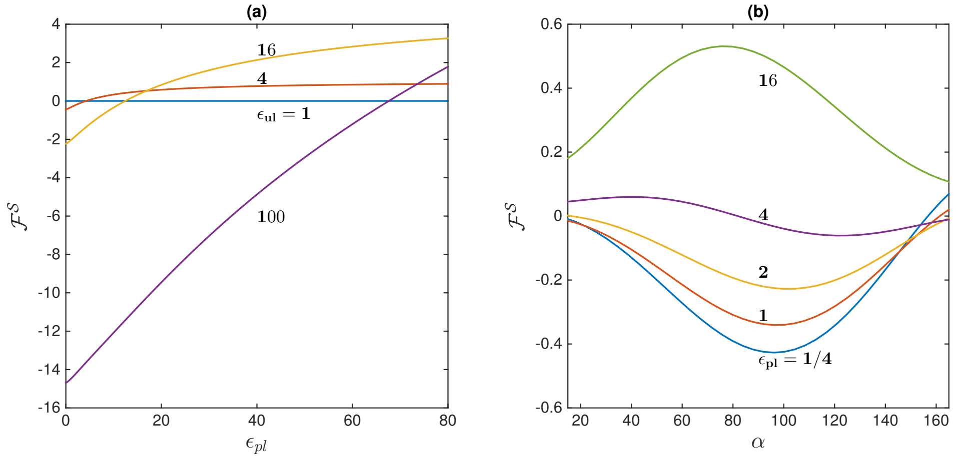

Figure 3.7. In applied tangential field with $\gamma = \epsilon$. (a) $\mathcal{F}^{\mathcal{S}}$ vs. ϵ_{pl}, when $\epsilon_{ul} = 1, 4, 16, 100$. $\alpha = \pi/2$. (b) $\mathcal{F}^{\mathcal{S}}$ vs. α. $\epsilon_{ul} = 4$, $\epsilon_{pl} = 1/4, 1, 2, 4, 16$.

3.6. Far-field Asymptotic Expansion of Potentials

In order to study the collective dynamics of many particles on an interface under an applied electric field, the electric interaction between the particles must be understood. Computationally, we could extend the results of the previous section to the many particle case but this would be a challenging numerical computation. A more common approach is to assume that the particles are far apart, and then to use the far-field asymptotic expansion of the potentials of each particle to calculate the force on a particular particle. This many body force approximation is typically calculated in the far-field approximation by determining the two-particle interaction force and then using this to determine the total force on the particle. The two-body force is calculated in the next section. Here we first calculate the far-field asymptotic expansion for the electric potential of a single particle on an interface.

For a particle located near the origin of the cylindrical coordinate system, our interest is to find the asymptotic behavior of the potential as $r \to \infty$ with z order one, i.e., close to the particle. In terms of the toroidal coordinate system, this implies that both ξ and η tend to zero (see Eq. 3.6).

3.6.1. Applied Normal field

Consider first the applied normal field case. Our aim is to find the far field expansion ($0 < \eta \ll 1$ and $0 \leq \xi \ll 1$) of the perturbed potential Φ. Here we give the details only for the upper potential Φ_u as defined by Eq. (3.3). In terms of our transformed toroidal coordinate system, this potential is given by the integral (3.14) along with (3.23) where the coefficients $\mathcal{C}_1$ and $\mathcal{C}_2$ are determined numerically as outlined in Section 2.

Begin by expanding $K^0(\eta, \tau)$ as $\eta \to 0$. This is done by finding a power series solution about $\eta = 0$ of the associated Legendre differential equation in terms of η . The result is

$$K^0(\eta, \tau) \sim 1 - (1/16 + \tau^2/4)\eta^2 + O(\eta^4), \quad \eta \to 0. \tag{3.83}$$

The expansion is valid for any fixed τ. Using (3.83) in Eq. (3.14) we find that Φ_u can be approximated as,

$$\Phi_u \sim \sqrt{\cosh \eta - \cos \xi} \int_0^{\tau_0} B_u(\xi, \tau)[1 - (1/16 + \tau^2/4)\eta^2] d\tau. \tag{3.84}$$

The truncated part of the integral decays exponentially with τ_0.

For fixed τ we can also expand B_u in Eq. (3.23) as $\xi \to 0$ (i.e. near interface $z = 0$)

(3.85)

$$B_u \sim \mathcal{C}_1 + \xi \left[-\mathcal{C}_1 \tau \coth \xi_0 \tau + (\mathcal{C}_2 + (1 - 1/\gamma_{ul}) 2^{3/2} \tau \sin \alpha \frac{\sinh (\pi - \xi_0)\tau}{\cosh \pi \tau}) \tau \operatorname{csch} \xi_0 \tau \right],$$

with truncation error at $O(\xi^2)$. Substitute Eq. (3.85) into (3.84) and using the inverse of the toroidal coordinates,

$$\xi = \frac{i}{2}\ln\frac{r^2+(z-i\sin\alpha)^2}{r^2+(z+i\sin\alpha)^2}, \quad \eta = \frac{1}{2}\ln\frac{z^2+(r+\sin\alpha)^2}{z^2+(r-\sin\alpha)^2}, \tag{3.86}$$

we obtain the far field expansion of Φ_u when $R=\sqrt{r^2+z^2}\to\infty$ and $z\sim O(1)$:

$$\Phi_u \sim C_2^u\frac{z}{R^3} + C_4^u\frac{1}{R^3} + O(R^{-5}). \tag{3.87}$$

Notice here that we write the answer in terms of R and z, not r. The coefficients C_i^u are calculated as below,

$$\begin{aligned} C_2^u &= 2\sqrt{2}\sin^2\alpha\int_0^\infty[-\mathcal{C}_1\tau\coth\xi_0\tau \\ &\quad + (\mathcal{C}_2+(1-1/\gamma_{ul})2^{3/2}\tau\sin\alpha\frac{\sinh{(\pi-\xi_0)\tau}}{\cosh\pi\tau})\tau\,\mathrm{csch}\,\xi_0\tau]d\tau \qquad (3.88) \\ C_4^u &= \sqrt{2}\sin^3\alpha\int_0^\infty(\frac{1}{4}-\tau^2)\mathcal{C}_1(\tau)d\tau. \qquad (3.89) \end{aligned}$$

These coefficients are found numerically.

Paralleling the above analysis in the lower fluid, we obtain,

$$\Phi_l \sim C_2^l\frac{z}{R^3} + C_4^l\frac{1}{R^3} + O(R^{-5}). \tag{3.90}$$

Using the boundary condition (3.2) it is straightforward to show that $C_2^u = C_2^l/\gamma_{ul}$ and $C_4^u = C_4^l$. Note that because there is no net charge on the particle the $O(R^{-1})$ terms do not contribute in the above expansions.

Eqs. (3.87) and (3.90) show that in the far-field, the leading order potential has two contributions: a dipole aligned with the applied electric field, given by the C_2^k term, and a quadrupole contribution, given by the C_4^k term.

In fig. 3.8(a)(b) we plot C_2^l as a function of the γ ratios. In fig. 3.8(a) we plot C_2^l as a function of γ_{pl} for several values of γ_{ul}. Notice that C_2^l decreases monotonically with γ_{pl}. When γ_{pl} is small, e.g., in a leaky dielectric this implies that the particle is less conductive than the surrounding fluids, we find that the effective far field dipole coefficient is positive, which indicates that the induced dipole is antiparallel to the applied field. With increasing γ_{pl}, the induced dipole flips sign and becomes parallel to the applied field. Here C_2^l is often referred to the excess dipole moment which is induced by the external field on the particle. This changing behavior of the dipole is illustrated for both of these cases in fig. 3.3, i.e. the induced dipolar fields in the lower fluid in fig. 3.3(b) are in the opposite direction of fig. 3.3(a). Finally note that as $\gamma_{pl} \to \infty$, the dimensionless dipole coefficient in the lower fluid asymptotes to a finite limit, similar to the behavior when $\gamma_{ul} = 1$. Also we find that $C_2^l = 0.5$ for $\gamma_{pl} = 0$ for all γ_{ul} when $\alpha = \pi/2$. In fig. 3.8(b) we plot C_2^l vs. γ_{ul} for fixed values of γ_{pl}. There we see the non-monotonic behavior of C_2^l with γ_{ul} implied in fig. 3.8(a), plus the asymptotic behavior with increasing γ_{ul} implied in fig. 3.8(a).

In fig. 3.8(c)(d), we plot C_4^l as a function of γ. Recall, $C_4^l = C_4^u$ corresponds to the quadrupole moment contribution at the same order as the dipole. When $\gamma_{ul} = 1$, the solution can be exactly found and there is no quadrupole, the potential is purely dipolar, otherwise C_4 is non-monotonic with γ_{pl} and γ_{ul}. Note that the magnitude of the quadrupole effect is much less than the dipolar effect for $\alpha = \pi/2$, implying that it will have only a small effect on the interaction force between particles when the particle is centered at the fluid interface.

In fig. 3.9 we plot C_2^l and C_4^l as a function of the contact angle α. Notice that when $1 < \gamma_{pl} < \gamma_{ul}$, i.e. from the curve of $\gamma_{pl} = 2$ in fig. 3.9(a), we observe that the far field

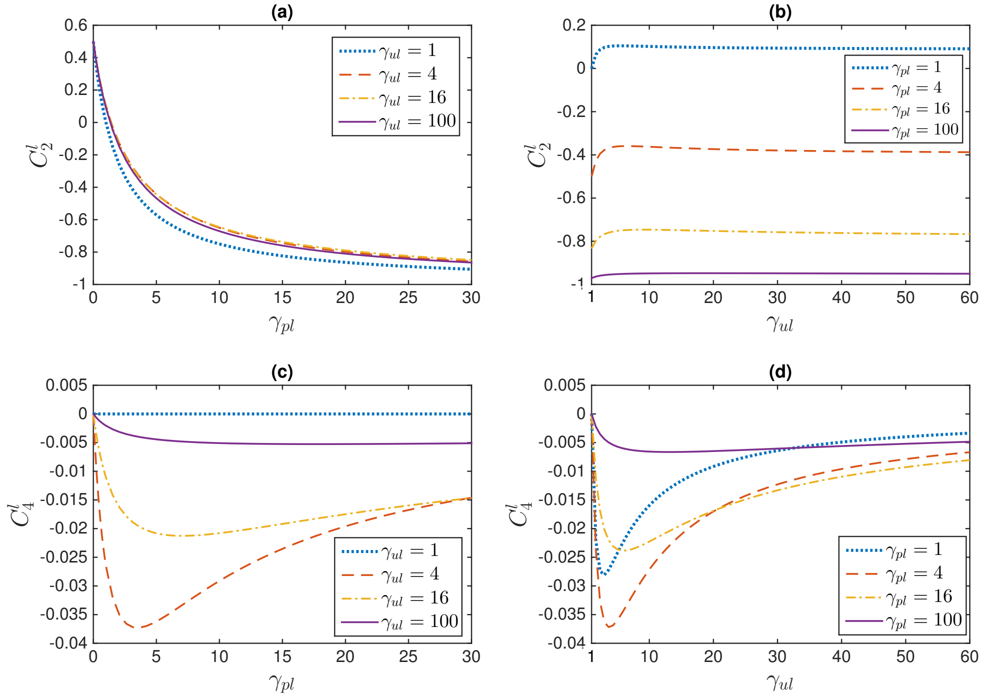

Figure 3.8. (Normal field) C_2^l and C_4^l when $\alpha = \pi/2$. (a) C_2^l vs. γ_{pl}, when $\gamma_{ul} = 1, 4, 16, 100$, (b) C_2^l vs. γ_{ul}, when $\gamma_{pl} = 1, 4, 16, 100$, (c) C_4^l vs. γ_{pl}, when $\gamma_{ul} = 1, 4, 16, 100$, (d) C_4^l vs. γ_{ul}, when $\gamma_{pl} = 1, 4, 16, 100$.

potential dipole coefficient C_2^l will flip sign when the particle emerges from the lower fluid into the upper fluid. This phenomenon was observed previously in a limiting case [**22**] where $\gamma_{ul} \to \infty$. In fig. 3.9(a) the dashed lines are the approximating function $C_{2A}^l(\alpha) = m_0 + (m_\pi - m_0)V(\alpha)$ where m_0 is the value of C_2^l at $\alpha = 0$, m_π is the value C_2^l at $\alpha = 180^\circ$, and $V(\alpha) = \sin^4(\alpha/2)(3 - 2\sin^2(\alpha/2))$ is proportional to the volume of the particle in the lower fluid as a function of α. Note that for the plots shown, this approximation does well in approximating the α dependence of C_2^l. The approximation works well for a wide range of parameters but will beging to fail when the behavior of C_2^l is no longer monotonic, e.g., see the $\gamma_{pl} = 16$ plot in fig. 3.9. Our computations imply this is true for large values of γ_{pl} and γ_{ul}. In fig. 3.9(b) the quadrupole coefficient C_4^l is generally small compared to C_2^l when $\alpha = \pi/2$. However away from $\pi/2$ (off-centered), the magnitude of quadrupole moment increases and becomes nonnegligible.

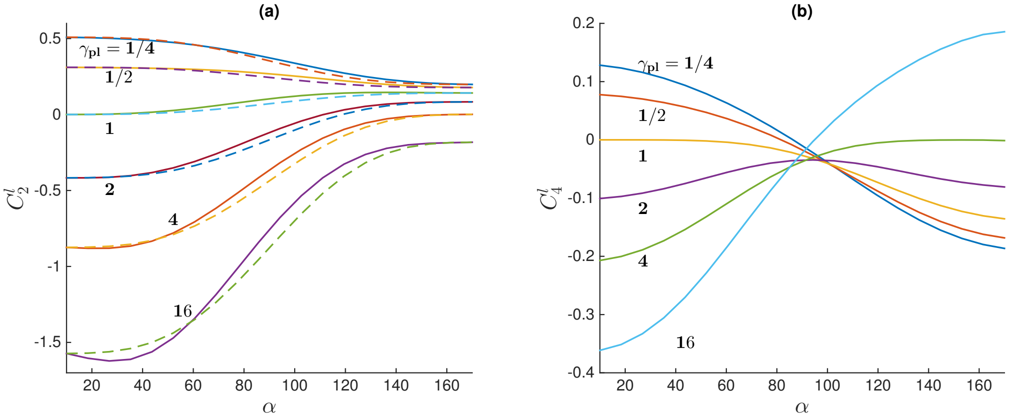

Figure 3.9. (Normal field) (a) C_2^l vs. α in degrees, when $\gamma_{pl} = 1/4, 1/2, 1, 2, 4, 16$, $\gamma_{ul} = 4$. The solid lines are numerical results while the broken lines at the approximate solutions C_{2A}^l. (b) C_4^l vs. α in degrees, when $\gamma_{pl} = 1/4, 1/2, 1, 2, 4, 16$, $\gamma_{ul} = 4$.

3.6.2. Applied Tangential Field

Paralleling the derivation of the previous subsection but now identifying the power series expansion of K^1 , the far-field asymptotic expansion for the induced potential in an applied tangential field has the general form:

$$\Phi_k \sim \bar{C}_2^k \frac{x}{R^3} + \bar{C}_4^k \frac{xz}{R^5} + \bar{C}_8^k \frac{x}{R^5} + O(R^{-7}). \tag{3.91}$$

The coefficients $\bar{C}_i^u$ and $\bar{C}_i^l$ are given by,

(3.92)

$$\bar{C}_2^l = \bar{C}_2^u = -\sqrt{2}\sin^2\alpha \int_0^\infty (\frac{1}{4} + \tau^2)\mathcal{C}_1(\tau)d\tau$$

(3.93)

$$\bar{C}_8^l = \bar{C}_8^u = \sqrt{2}\sin^4\alpha \int_0^\infty [\frac{5}{6}(\frac{1}{4}+\tau^2) + \frac{1}{2}(\frac{1}{4}+\tau^2)^2]\mathcal{C}_1(\tau)d\tau$$

(3.94)

$$\bar{C}_4^l = \gamma_{ul}\bar{C}_4^u = -2\sqrt{2}\sin^3\alpha \int_0^\infty (\frac{1}{4}+\tau^2)[-\mathcal{C}_1\tau\coth{(\xi_0-\pi)\tau} + \mathcal{C}_3\tau\,\mathrm{csch}\,(\xi_0-\pi)\tau]d\tau.$$

The first term in Eq. (3.91) is a tangential dipole potential, i.e. a dipole aligned horizontally with a higher order decaying effect. Since $\bar{C}_2^u = \bar{C}_2^l$, the far-field expansions in both the upper and lower fluid are identical at leading order and the particle can be regard as a single dipole. The $\bar{C}_4^k$ term is a quadrupole term. From the boundary condition Eq. (3.2) it must satisfy $\bar{C}_4^l = \gamma_{ul}\bar{C}_4^u$. The $\bar{C}_8^k$ term is from the octupole contribution. The quadrupole and octupole contributions both come at the same order in our far field expansion because of our assumptions on R and z.

3.7. Interaction of Widely Separated Particles

In the previous section we calculated the far-field behavior of the electric potential. Here we use these results to determine the force between two widely spaced identical particles resting on a fluid interface. Assume that particle 1 is centered at $(0, 0, -\cos\alpha)$ as shown in fig. 3.10 and that an identical particle2 is located a distance R_0 (dimensionless units) along the interface with $R_0 \gg 1$, see fig. 3.10. We seek to determine the applied horizontal force on particle 1 due to the presence of particle 2 by integrating the total Maxwell stress $\mathbf{\Sigma}$ over the particle 1 interface S^1. We are only interested in the components of the force in the direction horizontal to the interface, i.e., $F^x\mathbf{e_x} + \mathbf{F^y}\mathbf{e_y}$, where $\mathbf{e_x}$ and

$\mathbf{e_y}$ are unit vectors in the x and y directions, respectively. This allows us to write

$$F^m = \mathbf{F}\cdot\mathbf{e_m} = \iint_{S^1} \mathbf{\Sigma} d\mathbf{S}\cdot\mathbf{e_m}, \tag{3.95}$$

for $m = x, y$. Set $F^m = F^m_u + F^m_l$ were F^m_k only includes the integration of eq. (3.95) along the S^1_k, $k = u, l$, portion of the S^1 interface.

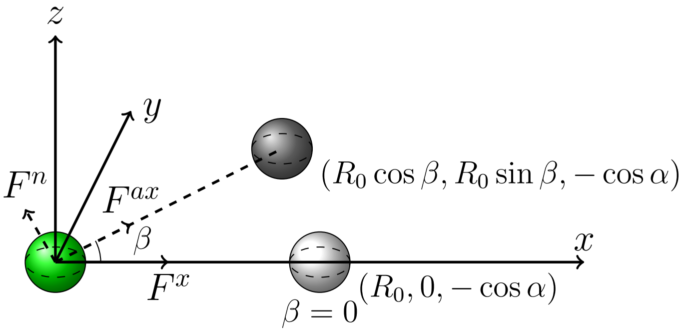

Figure 3.10. Particle locations in inter-particle force calculation. Normal field: assume the second particle centered at $(R_0, 0, -\cos\alpha)$, without losing any generality. Tangential field: assume the second particle centered at $(R_0\cos\beta, R_0\sin\beta, -\cos\alpha)$.

There is no contribution to the horizontal force from the constant pressure $p_{k\infty}$ in Eq. (3.76). The total electric stress in Eq. (3.95) accounts for the presence of both particles along the interface. In the widely spaced situation considered here ($R_0 \gg 1$), at leading order, the potential used to calculate the stress is simply the sum of the applied field on particle 1 (Section 3.2) plus the perturbation field from particle 2 (Section 3.6).

3.7.1. Applied Normal Field

Without loss of generality, assume that the center of particle 2 is located at $(R_0, 0, -\cos\alpha)$, see fig. 3.10. By symmetry we need only consider the x component of the force as given by eq. (3.95).

From Eq. (3.95), the force components in the x direction on particle 1 can be written as

$$F_k^x = (-1)^n \int_0^{2\pi} \int_0^{\infty} (-r\cos\theta \frac{\partial z}{\partial \eta}\Sigma_{11}^k - r\sin\theta \frac{\partial z}{\partial \eta}\Sigma_{12}^k + r\frac{\partial r}{\partial \eta}\Sigma_{13}^k) d\eta d\theta, \tag{3.96}$$

where $\xi = \xi_0$ and $n = 0$ for $k = u$ on the upper surface of particle 1, and $\xi = \xi_0 + \pi$ and $n = 1$ for $k = l$ on the lower surface in the above integral. The components of the Maxwell stress tensor $\mathbf{\Sigma}^k$ for $k = u, l$ in Eq.(3.96) are given by Eq.(3.76) where the potentials on the upper and lower surface of particle 1 are given by

$$\varphi_u = z/\gamma_{ul} + \Phi_{u,1} + \frac{C_4^u + C_2^u z}{R^3}, \tag{3.97}$$

$$\varphi_l = z + \Phi_{l,1} + \frac{C_4^l + C_2^l z}{R^3}. \tag{3.98}$$

Here $\Phi_{k,1}$ is the electric perturbation potential on particle 1 given by Eq. (3.14), and we have used the leading order contribution at $O(R^{-3})$ of the potential from particle 2 on particle 1 as given by eq. (3.87) and eq. (3.90),

$$\Phi_k \sim C_2^k \frac{z}{R^3} + C_4^k \frac{1}{R^3}, \quad k = u, l, \tag{3.99}$$

where now $R = \sqrt{(x - R_0)^2 + y^2 + z^2} >> 1$.

With this information, we can now compute the horizontal force F_k^x for $k = u, l$. At this point we find it convenient to expand R in Eqs. (3.97) and (3.98) for large R_0 and then substitute into Eq. (3.96). This allows us to write $\Sigma_{ij}^k = \Sigma_{0,ij}^k + \Sigma_{1,ij}^k R_0^{-3} + \Sigma_{2,ij}^k R_0^{-4} + \cdots$. The $O(1)$ in R_0 term in (3.96) integrates to zero as noted in Section 5, i.e., a particle in an applied normal field does not feel any horizontal force on the interface. We also find that the $O(R_0^{-3})$ term integrates to zero. The first nonzero contribution to (3.96) occurs at $O(R_0^{-4})$. At this order, the $\Sigma_{2,ij}^k$ contributions to the stress tensor in the upper fluid are:

$$\Sigma^u_{2,11} = -\frac{3\epsilon_u}{4\pi}\left\{C^u_2(1/\gamma_{ul} + \frac{\partial\Phi_{u,1}}{\partial z})x - C^u_2\frac{\partial\Phi_{u,1}}{\partial x}z - C^u_4\frac{\partial\Phi_{u,1}}{\partial x}\right\}, \tag{3.100}$$

$$\Sigma^u_{2,12} = \frac{3\epsilon_u}{4\pi}\left\{C^u_2\frac{\partial\Phi_{u,1}}{\partial y}z + C^u_4\frac{\partial\Phi_{u,1}}{\partial y}\right\}, \tag{3.101}$$

$$\Sigma^u_{2,13} = \frac{3\epsilon_u}{4\pi}\left\{C^u_2\frac{\partial\Phi_{u,1}}{\partial x}x + C^u_2(\frac{\partial\Phi_{u,1}}{\partial z} + 1/\gamma_{ul})z + C^u_4(\frac{\partial\Phi_{u,1}}{\partial z} + 1/\gamma_{ul})\right\}. \tag{3.102}$$

The components of the horizontal force on the upper part of the particle 1 interface can be found by plugging eqs. (3.100) to (3.102) into eq. (3.96), and integrating. A similar calculation can also be done for the lower part of particle 1.

A non-dimensional inter-particle force coefficient $\mathcal{F}^{\mathcal{I}}$ can now be defined by summing the upper and lower forces on particle 1,

$$F^x = F^x_u + F^x_l = \frac{\epsilon_l}{4R_0^4}\mathcal{F}^{\mathcal{I}}. \tag{3.103}$$

Figure 3.11 shows the force coefficients $\mathcal{F}^{\mathcal{I}}$ with fixed γ_{lu} values and increasing γ_{pu}, when $\alpha = 2\pi/3$. In Figure 3.11a we consider the dielectric case where $\gamma = \epsilon$. We find that $\mathcal{F}^{\mathcal{I}}$ remains negative (repulsive) for all values considered. The force decreases in magnitude with increasing γ_{pl}, reaches zero, and then continues increasing in magnitude. Notice that $\mathcal{F}^{\mathcal{I}} = 0$ for $\epsilon_{ul} = \epsilon_{pl} = 1$, i.e., where you have a homogeneous material. Also note that it is also possible for $\mathcal{F}^{\mathcal{I}} = 0$ when $\gamma_{ul} \neq 1$, since as noted in Figure 3.8a, C^l_2 will vanish for finite values of γ_{pl}. In this case the quadrupole terms determine the leading order behavior of the force and the contribution will occur at $O(R_0^{-8})$, this will not be discussed further here.

In Figure 3.11b we consider the leakly dielectric case where $\gamma = \sigma$ is varied but the dielectric constants appearing in the force definition in Eq. (3.78) are set as $\epsilon_u/\epsilon_l = 1$.

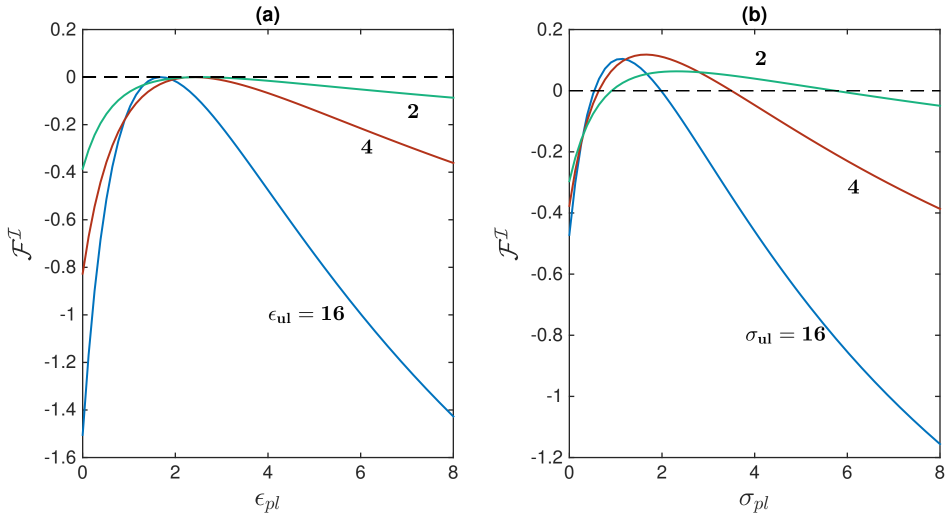

Figure 3.11. (Normal field) $\mathcal{F}^{\mathcal{I}}$ vs. γ_{pl}, $\alpha = 2\pi/3$. (a) $\gamma = \epsilon$, $\epsilon_{ul} = 2, 4, 16$. (b) $\gamma = \sigma$, $\sigma_{ul} = 2, 4, 16$ and $\epsilon_{ul} = 1$ is used for all cases.

Note that in the leakly dielectric case of Figure 3.11b we can find reasonable values of σ_{ul} which makes the total force attractive, $\mathcal{F}^{\mathcal{I}} > 0$ at order $O(R_0^{-4})$. This happens when the quadrupole contribution occurring in the potential of eq. (3.99) becomes dominant.

When $\gamma = \epsilon$, here we prive that the C_4^k terms in eq. (3.99) do not contribute to the inter-particle force F_k^x. This follows because there is zero net charge on the interface of a dielectric.

The contribution of C_4 terms in eqs. (3.100) to (3.102) substituted back to eq. (3.96) can be written as

$$F^x = \epsilon_u \iint_{S_u} \mathcal{E}_4^u \mathbf{n}_u dS + \epsilon_l \iint_{S_l} \mathcal{E}_4^l \mathbf{n}_l dS$$

,

where $\mathcal{E}_4^u = \frac{3C_4^u}{4\pi}(\frac{\partial \Phi_{u,1}}{\partial x}, \frac{\partial \Phi_{u,1}}{\partial y}, \frac{\partial \Phi_{u,1}}{\partial z} + 1/\gamma_{ul})$ and $\mathcal{E}_4^l = \frac{3C_4^l}{4\pi}(\frac{\partial \Phi_{l,1}}{\partial x}, \frac{\partial \Phi_{l,1}}{\partial y}, \frac{\partial \Phi_{l,1}}{\partial z} + 1)$.

Because $\nabla \cdot \mathcal{E}_4^k = 0$, by using divergence theorem, we obtain

$$F^x = -\epsilon_u \iint_{I_u} \mathcal{E}_4^u \mathbf{n}_u dS - \epsilon_l \iint_{I_l} \mathcal{E}_4^l \mathbf{n}_l dS,$$

where I_u and I_l are actually the same fluid-fluid interface from the three-phase contact line to infinite far away, with $\mathbf{n}_u = -\mathbf{n}_l = \mathbf{e_z}$. Thus,

$$F^x = -\epsilon_u C_4^u \iint_{I_u} (\frac{\partial \Phi_{u,1}}{\partial z} + 1/\gamma_{ul}) dS + \epsilon_l C_4^l \iint_{I_l} (\frac{\partial \Phi_{l,1}}{\partial z} + 1)\mathbf{n}_l dS.$$

We know that $C_4^u = C_4^l$ and $\frac{\partial \Phi_{u,1}}{\partial z} = \frac{\partial \Phi_{l,1}}{\partial z}/\gamma_{ul}$ at $z = 0$. Thus when $\gamma = \epsilon$, we get $F^x = 0$.

In this case, paralleling the calculation in [**22**], it can be found analytically that the leading order force between a pair of wide-separated particles is a dipole-dipole interaction and the inter-particle force can now be identified as

$$F^x = -3\frac{\epsilon_l (C_2^l)^2 + \epsilon_u (C_2^u)^2}{2R_0^4}. \tag{3.104}$$

Note that this result is independent of ϵ_{pl} and α since these parameters will only change the total force by influencing the effective induced dipole moments, i.e. C_2^k. Equation (3.104) is consistent with the special case considered in [**22**]. In should be noted that even in the leakly dielectric case where $\gamma = \sigma$, eq. (3.104) is a good approximation when the quadrupole coefficients are much smaller than dipole coefficients, such as when $\alpha = \pi/2$ shown in fig. 3.9.

3.7.2. Applied Tangential Field

When the electric field is applied tangential to the fluid interface and parallel to the x-axis, the force on particle 1 depends not only on the distance between the two particles, R, but on the location of particle 2 relative to the direction of the applied field. The interaction force will have components in both the x and y direction (an electric torque will also exist in this case). To make this more definite, assume that particle 1 is again centered at $(0, 0, -\cos\alpha)$, while particle 2 is centered at $(R_0 \cos\beta, R_0 \sin\beta, -\cos\alpha)$, where β is the angle in the $x-y$ plane measured from the x-axis and to the plane through the particle centers and perpendicular to the $x-y$ plane, see fig. 3.10, with $\beta > 0$ if both x and y are positive.

The interaction force F^x in the x-direction is again calculated from eq. (3.96) but now using in the Maxwell stress a potential which is the sum of the far field potential of particle 2 given by eq. (3.91) plus the potential eq. (3.33) of a single particle in an applied tangential field. To get the leading order behavior in R_0 of F^x both the R^{-3} and R^{-5} terms in eq. (3.91) need to be retained in the approximation. Note that here we set $R = \sqrt{(x - R_0 \cos\beta)^2 + (y - R_0 \sin\beta)^2 + z^2} >> 1$. The constant offset in z-direction will not affect the result.

The force in y direction is

$$F_k^y = (-1)^n \int_0^{2\pi} \int_0^{\infty} (-r\cos\theta \frac{\partial z}{\partial \eta} \Sigma_{21}^k - r\sin\theta \frac{\partial z}{\partial \eta} \Sigma_{22}^k + r\frac{\partial r}{\partial \eta} \Sigma_{23}^k) d\eta d\theta, \tag{3.105}$$

where again $\xi = \xi_0$ and $n = 0$ for $k = u$ on the upper surface of particle 1, and $\xi = \xi_0 + \pi$ and $n = 1$ for $k = l$ on the lower surface in the above integral.

As in the previous section, the Maxwell tensor can be expanded in R_0 and we find that the leading order nonzero contribution to the interaction force from particle 2 is given by,

$$\begin{aligned}\Sigma^k_{2,11} = &-\frac{3\epsilon_k\bar{C}^k_2}{16\pi}\big\{[3(1+\frac{\partial\Phi_{k,1}}{\partial x})x-\frac{\partial\Phi_{k,1}}{\partial y}y+4\frac{\partial\Phi_{k,1}}{\partial z}z]\cos\beta+5(x+\frac{\partial\Phi_{k,1}}{\partial x}x+\frac{\partial\Phi_{k,1}}{\partial y}y)\cos 3\beta\\ &-[\frac{\partial\Phi_{k,1}}{\partial y}x-(1+\frac{\partial\Phi_{k,1}}{\partial x})y](\sin\beta+5\sin 3\beta)\big\}+\frac{\epsilon_k\bar{C}^k_4}{4\pi}\frac{\partial\Phi_{k,1}}{\partial z}\cos\beta,\end{aligned}\tag{3.106}$$

$$\begin{aligned}\Sigma^k_{2,12} = &-\frac{3\epsilon_k\bar{C}^k_2}{16\pi}\big\{[(1+\frac{\partial\Phi_{k,1}}{\partial x})y+3\frac{\partial\Phi_{k,1}}{\partial y}x]\cos\beta+5[\frac{\partial\Phi_{k,1}}{\partial y}x-(1+\frac{\partial\Phi_{k,1}}{\partial x})y]\cos 3\beta\\ &+[(1+\frac{\partial\Phi_{k,1}}{\partial x})x+\frac{\partial\Phi_{k,1}}{\partial y}y](\sin\beta+5\sin 3\beta)\big\},\end{aligned}\tag{3.107}$$

$$\begin{aligned}\Sigma^k_{2,13} = &-\frac{3\epsilon_k\bar{C}^k_2}{16\pi}\big\{[-4(1+\frac{\partial\Phi_{k,1}}{\partial x})z+3\frac{\partial\Phi_{k,1}}{\partial z}x]\cos\beta+5\frac{\partial\Phi_{k,1}}{\partial z}x\cos 3\beta\\ &+\frac{\partial\Phi_{k,1}}{\partial z}y(\sin\beta+5\sin 3\beta)\big\}-\frac{\epsilon_k\bar{C}^k_4}{4\pi}(1+\frac{\partial\Phi_{k,1}}{\partial x})\cos\beta,\end{aligned}\tag{3.108}$$

$$\begin{aligned}\Sigma^k_{2,22} = &\frac{3\epsilon_k\bar{C}^k_2}{16\pi}\big\{[3(1+\frac{\partial\Phi_{k,1}}{\partial x})x-\frac{\partial\Phi_{k,1}}{\partial y}y+4\frac{\partial\Phi_{k,1}}{\partial z}z]\cos\beta+5(x+\frac{\partial\Phi_{k,1}}{\partial x}x+\frac{\partial\Phi_{k,1}}{\partial y}y)\cos 3\beta\\ &-[\frac{\partial\Phi_{k,1}}{\partial y}x-(1+\frac{\partial\Phi_{k,1}}{\partial x})y](\sin\beta+5\sin 3\beta)\big\}+\frac{\epsilon_k\bar{C}^k_4}{4\pi}\frac{\partial\Phi_{k,1}}{\partial z}\cos\beta,\end{aligned}\tag{3.109}$$

$$\begin{aligned}\Sigma^k_{2,23} = &-\frac{3\epsilon_k\bar{C}^k_2}{16\pi}\big\{(\frac{\partial\Phi_{k,1}}{\partial z}y-4\frac{\partial\Phi_{k,1}}{\partial y}z)\cos\beta-5\frac{\partial\Phi_{k,1}}{\partial z}y\cos 3\beta+\frac{\partial\Phi_{k,1}}{\partial z}x(\sin\beta+5\sin 3\beta)\big\}\\ &-\frac{\epsilon_k\bar{C}^k_4}{4\pi}\frac{\partial\Phi_{k,1}}{\partial y}\cos\beta.\end{aligned}\tag{3.110}$$

From eqs. (3.106) to (3.110), we see that only the dipole ($\bar{C}^k_2$) and quadrupole ($\bar{C}^k_4$) terms contribute to the integration of the forces at the leading order of $O(R_0^{-4})$.

Substitute eqs. (3.106) to (3.110) into eq. (3.96) and eq. (3.105) and sum up the forces on the upper and lower surface. Consider only the total force due to the dipole-dipole interactions, i.e., the $\bar{C}_2^k$ terms in the above. Write the x and y components of this dipole-dipole force as F_d^x and F_d^y, respectively. This allows us to write,

$$F_d^x = \frac{\epsilon_l}{4R_0^4}(\mathcal{F}_{c,d}^{\mathcal{I}} \cos\beta + \mathcal{F}_{c3,d}^{\mathcal{I}} \cos 3\beta), \quad F_d^y = \frac{\epsilon_l}{4R_0^4}(\mathcal{F}_{s,d}^{\mathcal{I}} \sin\beta + \mathcal{F}_{s3,d}^{\mathcal{I}} \sin 3\beta), \tag{3.111}$$

where we have factored out the β dependence. Specifically, $\mathcal{F}_{c,d}^{\mathcal{I}}, \mathcal{F}_{c3,d}^{\mathcal{I}}$, $\mathcal{F}_{s,d}^{\mathcal{I}}$, and $\mathcal{F}_{s3,d}^{\mathcal{I}}$ are dipolar force coefficients independent of the particle align angle β. From eqs. (3.106) to (3.110), it can be proved in Appendix F that $\mathcal{F}_{c3,d}^{\mathcal{I}} = \frac{5}{3}\mathcal{F}_{c,d}^{\mathcal{I}}$, $\mathcal{F}_{s3,d}^{\mathcal{I}} = \frac{5}{3}\mathcal{F}_{c,d}^{\mathcal{I}}$ and $\mathcal{F}_{s,d}^{\mathcal{I}} = \frac{1}{3}\mathcal{F}_{c,d}^{\mathcal{I}}$. Rewriting the force components in the axial direction with respect to the particle centers, we obtain,

$$F_d^{ax} = \frac{\epsilon_l \mathcal{F}_{c,d}^{\mathcal{I}}}{4R_0^4}(\frac{2}{3} + 2\cos 2\beta), \quad F_d^n = \frac{\epsilon_l \mathcal{F}_{c,d}^{\mathcal{I}}}{4R_0^4}(\frac{4}{3}\sin 2\beta), \tag{3.112}$$

Thus the maximum dipole interaction F_d^{ax} in axial direction direction with respect to β is obtained when $\beta = 0$ or π. The maximum in the perpendicular direction F_d^n is obtained at $\beta = \frac{\pi}{4}$ or $\frac{3\pi}{4}$.

As with the applied normal field case of Section 7.1, the quadrupole does not contribute to the leading order inter-particle force when we set $\gamma = \epsilon$. Only the dipole-dipole interaction at the leading order occurs with the force exponents as,

$$F_d^{ax} = \bar{\epsilon}\frac{3\bar{C}_2^2}{2R_0^4}(1 + 3\cos 2\beta), \quad F_d^n = \bar{\epsilon}\frac{3\bar{C}_2^2}{R_0^4}\sin 2\beta, \tag{3.113}$$

where $\bar{\epsilon} = (\epsilon_u + \epsilon_l)/2$ is the average dielectric constants of the two fluid material and $\bar{C}_2 = \bar{C}_2^l = \bar{C}_2^u$. This result is equivalent to the classical result for a general dipole-dipole interaction [**33, 67**]. We have another proving of 3.113 using an analogy of the method in [**23**], in Appendix E.

In the leaky dielectric case there is a non-zero quadrupole contribution at leading order in the force, i.e., $O(R_0^{-4})$. From Equations (3.106) to (3.110), we observe that the quadrupole interaction terms (i.e., those with $\bar{C}_4^k$) are all proportional to $\cos\beta$. These terms do not contribute to the force in the y direction but there is a force contribution in the x direction. Denote this quadrupole contribution to the force as F_q^x and write

$$F_q^x = \frac{\epsilon_l}{4R_0^4}\mathcal{F}_{c,q}^{\mathcal{I}}\cos\beta. \tag{3.114}$$

Note that here when $\gamma = \epsilon$ and with $\mathcal{E}_4^k = \frac{\bar{C}_4^k}{4\pi}(\frac{\partial\Phi_{k,1}}{\partial z}, 0, -\frac{\partial\Phi_{k,1}}{\partial x}+1)$, because $\frac{\partial\Phi_{u,1}}{\partial x} = \frac{\partial\Phi_{l,1}}{\partial x}$ at $z = 0$ and $\bar{C}_4^u = \bar{C}_4^l/\gamma_{ul}$, we still obtain $F_q^x = 0$.

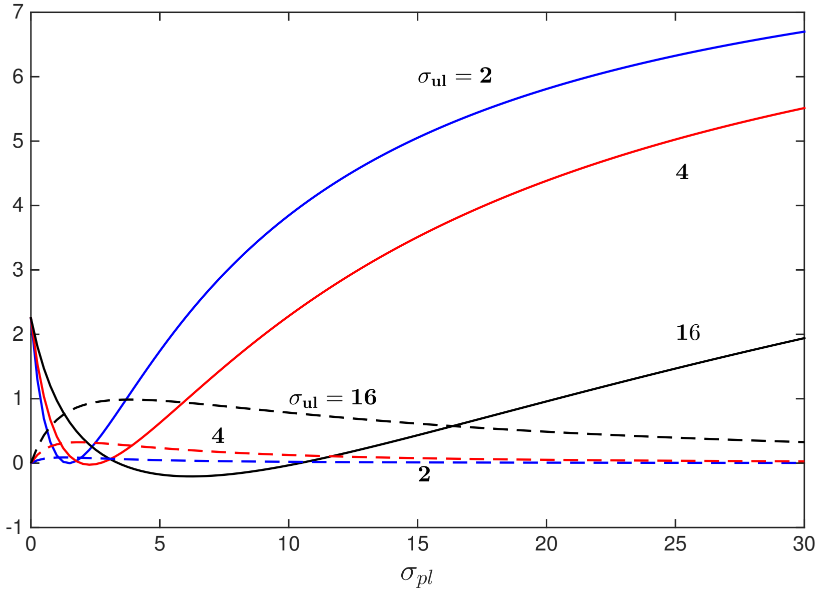

Figure 3.12. (Tangential field) $\mathcal{F}_{c,d}$ (solid lines) and $\mathcal{F}_{c,q}$ (dashed lines) vs. σ_{pl} when $\sigma_{ul} = 2, 4, 16$. $\alpha = \pi/2$ and $\epsilon_{ul} = 1$ is used.

Combinding this result with eq. (3.111) the total force in the x-direction can be written as $F^x = F^x_d + F^x_q = \epsilon_l \left[3(\mathcal{F}^{\mathcal{I}}{}_{c,d} + \mathcal{F}^{\mathcal{I}}{}_{c,q}) \cos\beta + 5\mathcal{F}^{\mathcal{I}}{}_{c,d} \cos 3\beta \right] / 12R_0^4$. Figure 3.12 plots the two force coefficients $\mathcal{F}_{c,d}$ and $\mathcal{F}_{c,q}$ as a function of σ_{pl} for several values of σ_{ul}, when $\alpha = \pi/2$ in the leaky dielectric case, i.e., when $\gamma = \sigma$. Notice that the magnitude of the dipole force contribution and quadrupole force contribution can be of the same order for small values of σ_{pl}, but when the particle becomes more conductive, i.e. $\sigma_{pl} >> \sigma_{ul}$, the dipolar interaction becomes dominant, and estimates of the inter-particle force using only dipole interactions becomes a reasonable approximation. But for less conductive particles, the quadrupole contribution to the force cannot be ignored.

CHAPTER 4

Electrohydrodynamic assembly of colloidal particles on a drop interface

4.1. Introduction

Emulsions of particle-coated drops (so called Pickering emulsions [**1, 2**]) are widely used in the pharmaceutical, food, personal care and many other industries [**3**]. Colloidosomes, which are microcapsules with shells made of colloid particles [**4**], are used for drug delivery due to the great degree of control of the shell permeability [**5**]. Colloidal particles get trapped at interfaces between immiscible (e.g., oil/water) fluids [**6**] (since the energy to detach a particle adsorbed at an interface exceeds the thermal energy by the thousands) and at high packing density form a shell enapsulating the drop that stabilizes emulsions against coalescence and enables selective permeability [**4, 7, 8, 9, 10**]. Colloids at low surface coverage, however, do not form static structures, but instead assemble dynamically [**11, 12, 13, 14**]. For example, a uniform electric field was found to induce various patterns such as an equatorial belt, pole-to-pole chains or a band of dynamic vortices [**11, 12**]. The latter intriguing phenomenon has not been explained thus far and motivates our study.

The collective dynamics of colloidal particles adsorbed at the interface of a drop in the presence of an electric field presents a challenging problem. The presence of the interface strongly modifies the electrostatic and hydrodynamic interactions between the particles, and introduces new interactions such as the classic capillary attraction (Cheerios effect)[**15**]. The latter arises from local deformation of the interface (e.g., if the particle has weight) [**16, 17, 18, 19, 20**]. The interfacial distortions increase the interfacial area and thus raise the interfacial free energy; one way of minimizing this effect is to bring the particles together so that their menisci overlap. The electrostatic interaction between charged particles in the absence of electric field [**21**] or in the presence of electric field [**22, 23**] can significantly differ from the particle interactions in a homogeneous medium. Our previous work showed that depending on the particles and suspending fluid conductivities, the far-field interaction between interface-trapped particles may get significant contribution from the electric-field induced particle quadrupole and overcome the dipole-dipole interaction. Particle hydrodynamics at interfaces is also highly nontrivial as shown by studies of the motion of an isolated particle [**54, 55, 68, 69, 70, 71**] or simulations of many particles [**72, 73, 74**].

In previous work we used the effective moment method to study the dynamics of particles in a homogeneous fluid but in an applied non-uniform electric field. Here we generalize this approach to determine the collective motion and assembly of colloidal spheres trapped at a drop interface in a uniform applied electric field. Our aim is to use this model to simulate the dynamics seen in recent experiments on particle covered drops [**11, 12**] and to systematically show the impact of particle concentration and field strength on the dynamics. The model presented here accounts for the electric field driven flow within the drop and suspending fluid, particle-particle electrostatic interaction, and the particle motion and rotation due to the induced flow and the applied electric field. The impact of particle concentration and electric field strength on the collective motions of the particles is investigated. We also present simulations illustrating the effect of changing particle coverage and applied field strength to the observed clustering phenomenon near the equator of the drop.

4.2. Problem Formulation

A drop placed in an electric field polarizes if its permittivity ε_d and conductivity σ_d are different than the suspending fluid permittivity ε_f and conductivity σ_f. Finite conductivity, even if very low, enables the passage of electric current and electrical charge accumulates at the drop interface. The electric field acting on this induced surface charge creates shear electric stress that drag the fluids into motion. In the case of a uniform DC electric field of strength E_0, the fluid undergoes axisymmetric straining flow about the drop. For a spherical drop of radius R_0, the surface velocity is [**25**]

$$\mathbf{u}_\theta^\infty = \frac{9E_0^2 R_0 \epsilon_d \left(1 - \frac{\epsilon_f \sigma_d}{\epsilon_d \sigma_f}\right)}{10\left(2 + \frac{\sigma_d}{\sigma_f}\right)^2 (\mu_f + \mu_d)} \sin 2\theta \hat{\mathbf{t}}. \tag{4.1}$$

where θ is the spherical polar angle measured from the direction of the applied uniform electric field (see Fig. 4.1). Here μ_f and μ_d are the viscosity of the suspending fluid and drop, respectively. This flow field is directed either from pole to equator or equator to pole depending on the relative magnitude of the drop and suspending fluid charge relaxation time, $\frac{\sigma_d}{\epsilon_d}$ and $\frac{\sigma_f}{\epsilon_f}$.

Particles adsorbed at the drop interface are advected by the flow and if the flow is from pole to equator, i.e., $\frac{\sigma_d}{\epsilon_d} < \frac{\sigma_f}{\epsilon_f}$, particles are expected to accumulate at the drop equator. Hence, the band formation observed in the experiments [**11, 12**] is likely driven by the electrohydrodynamic flow. However, particles also polarize in the electric field and interact electrostatically, which typically results in chaining [**11, 12, 75, 76**].

To study the complex interplay of flow advection and dielectrophoretic motion on the collective dynamics of particles, we develop a model under several assumptions. Drop shape remains spherical, i.e., the electric capillary number $Ca = \varepsilon_f E_0^2 R_0/\gamma \ll 1$, where γ the surface tension. We only consider particle motions tangential to the drop surface, i.e., in the normal direction all forces exerted on a particle are balanced. This is a reasonable assumption given the large surface energy needed to remove a particle from the interface, $\sim \gamma\pi a^2 \sin^2\Theta$, where Θ is the contact angle at the interface of the three-phase line between the two fluids and the particle, and a is the particle radius. Since the particles are small, interfacial deformation due to particle weight is negligible (Bond number $Bo = a^2\Delta\rho g/\gamma \ll 1$, where $\Delta\rho$ is the density difference, and g the acceleration due to gravity). The problem geometry is sketched in Figure 4.1.

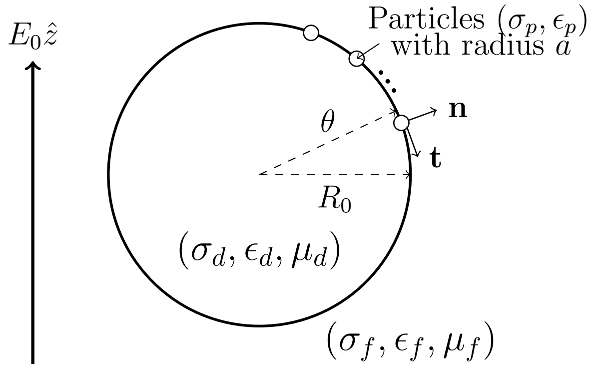

Figure 4.1. Sketch of the problem: Colloidal spheres with radius a are trapped at the interface of a drop with radius R_0, $a/R_0 << 1$. The dielectric constants of the particles, drop, and suspending fluid are ϵ_p, ϵ_d, and ϵ_f, conductivities are σ_p, σ_d, and σ_f, and the viscosities of the drop and suspending fluids are μ_d, μ_f, respectively. A uniform DC electric field **E** is applied globally. **n** and **t** are unit normal and tangential vectors on the drop surface.

Hereafter, all variables are nondimensionalized (noted by a tilde) using the radius of the drop R_0, the field strength E_0, a characteristic applied stress $\tau_c = \varepsilon_f E_0^2$, and the properties of the suspending fluid. Accordingly, the time scale for the electrohydrodynamic flow is $t_{\mathrm{hd}} = \mu_f/\tau_c$. The flow velocity scale is $u_c = R_0\tau_c/\mu_f$.

We utilize the model of N neutral particles subjected to an applied electric field in a homogeneous medium developed in chapter 2. The evolution of the induced electric dipole and quadrupole of particle i ($i = 1, ..., N$) are

$$\begin{aligned}\frac{d\widetilde{\mathbf{P}}_i}{dt} =& \widetilde{\boldsymbol{\Omega}}_i \times \left[\widetilde{\mathbf{P}}_i + \epsilon_{cm}\left(-\widetilde{\mathbf{E}}_{ap} + \sum_{j\neq i}\left(\frac{1}{\widetilde{\mathbf{R}}_{ij}^3}\Pi\cdot\widetilde{\mathbf{P}}_j + \frac{1}{2}\nabla\frac{\widetilde{\mathbf{R}}_{ij}\widetilde{\mathbf{R}}_{ij} : \widetilde{\mathbf{Q}}_j}{\mid \widetilde{\mathbf{R}}_{ij}\mid^5}\right)\right)\right] \\ & - D\left[\widetilde{\mathbf{P}}_i + \sigma_{cm}\left(-\widetilde{\mathbf{E}}_{ap} + \sum_{j\neq i}\left(\frac{1}{\widetilde{\mathbf{R}}_{ij}^3}\Pi\cdot\widetilde{\mathbf{P}}_j + \frac{1}{2}\nabla\frac{\widetilde{\mathbf{R}}_{ij}\widetilde{\mathbf{R}}_{ij} : \widetilde{\mathbf{Q}}_j}{\mid \widetilde{\mathbf{R}}_{ij}\mid^5}\right)\right)\right],\end{aligned} \tag{4.2}$$

and

$$\begin{aligned}\frac{d\widetilde{\mathbf{Q}}_i}{dt} =& \left\{\widetilde{\boldsymbol{\Omega}}_i \times \left[\widetilde{\mathbf{Q}}_i + 2\epsilon'_{cm}\nabla\left(-\widetilde{\mathbf{E}}_{ap} + \sum_{j\neq i}\frac{1}{\widetilde{\mathbf{R}}_{ij}^3}\Pi\cdot\widetilde{\mathbf{P}}_j\right)\right]\right\}^{sym} \\ & - D'\left[\widetilde{\mathbf{Q}}_i + 2\sigma'_{cm}\nabla\left(-\widetilde{\mathbf{E}}_{ap} + \sum_{j\neq i}\frac{1}{\widetilde{\mathbf{R}}_{ij}^3}\Pi\cdot\widetilde{\mathbf{P}}_j\right)\right],\end{aligned} \tag{4.3}$$

where

$$\Pi\cdot\widetilde{\mathbf{P}}_j = \widetilde{\mathbf{P}}_j - 3(\widetilde{\mathbf{P}}_j\cdot\widehat{\mathbf{R}}_{ij})\widehat{\mathbf{R}}_{ij} \quad . \tag{4.4}$$

Here sym denotes $A_{ij}^{sym} = A_{ij} + A_{ij}^{\mathsf{T}}$ and superscript T denotes transpose. The interparticle distance vector from particle i to particle j is defined as $\widetilde{\mathbf{R}}_{ij} = \mathbf{x}_i - \mathbf{x}_j$ where $\mathbf{x}_i$ is the position of the i^{th} particle. The vector $\boldsymbol{\Omega}_i$ is the rotation rate of particle i. The constants in the above equation are defined by

$$\epsilon_{cm} = \frac{\epsilon_p - \epsilon_m}{\epsilon_p + 2\epsilon_m}, \quad \sigma_{cm} = \frac{\sigma_p - \sigma_m}{\sigma_p + 2\sigma_m}, \quad \tau_{mw} = \frac{\epsilon_p + 2\epsilon_m}{\sigma_p + 2\sigma_m},$$

and

$$\epsilon'_{cm} = \frac{\epsilon_p - \epsilon_m}{2\epsilon_p + 3\epsilon_m}, \quad \sigma'_{cm} = \frac{\sigma_p - \sigma_m}{2\sigma_p + 3\sigma_m}, \quad \tau'_{mw} = \frac{2\epsilon_p + 3\epsilon_m}{2\sigma_p + 3\sigma_m}.$$

The interface at which the particles are trapped separates fluids with different properties. We assume that the particles are instead in a homogeneous medium with effective properties $\mu_m = (\mu_d + \mu_f)/2$, $\sigma_m = (\sigma_d + \sigma_f)/2$ and $\varepsilon_m = (\varepsilon_d + \varepsilon_f)/2$. The parameters with the subscripts *cm* are sometimes referred to as the Clausius-Mossotti factors while the parameters with the subscripts *mw* are the Maxwell-Wagner times which measure in the absence of rotation the times for the dipole and quadrupole moments to relax toward a steady state. Note here the evolution of higher order moments can be obtained in a similar way. This analysis assumed that the ratio $\gamma = a/d$ of the particle radius a to mean inter-particle distance d is small and of the same order as the ratio d/R_0 of the mean inter-particle distance to the drop radius R_0. In chapter 2 we used this assumption to ensure that the accuracy of the above electrostatic force model for the particle dynamics entered at the same order of accuracy as the hydrodynamic model below. This requires the assumption that the length scale over which changes in the local electric field strength varies along the particle is given by R_0. The latter assumption is certainly reasonable given the the local electric field varies from being tangent to the drop interface near the equator to normal to the interface at the poles of the drop.

Particle i translates with velocity $\mathbf{u}_i$ and rotates with rate $\widetilde{\mathbf{\Omega}}_i$ in response to the electrostatic forces, the global flows, and the flows generated by neighboring particles.

$$\mathbf{u}_i = \mathbf{u}_i^{\infty} + \widetilde{\mathbf{F}}_i^{d1} + \widetilde{\mathbf{F}}_i^{d2} + \widetilde{\mathbf{F}}_i^{d3} + \sum_{j\neq i} \widetilde{\mathbf{F}}_{ij}^{rep} + \sum_{j\neq i} \frac{6(5(\widetilde{\mathbf{F}}_j^{d1} + \widetilde{\mathbf{F}}_j^{d3}) \cdot \widehat{\mathbf{R}}_{ij})\widehat{\mathbf{R}}_{ij}}{8R_{ij}^4}$$

$$+\sum_{j\neq i}[-\frac{(\widetilde{\mathbf{T}}^E_j\cdot\hat{\mathbf{n}}_j)\hat{\mathbf{n}}_j\times\widehat{\mathbf{R}}_{ij}}{R_{ij}^2}+\frac{6}{8}(\frac{1}{R_{ij}}+\frac{2}{3R_{ij}^3})(\widetilde{\mathbf{F}}^{d1}_j+\widetilde{\mathbf{F}}^{d2}_j+\widetilde{\mathbf{F}}^{d3}_j)$$

$$+\frac{6}{8}(\frac{1}{R_{ij}}-\frac{2}{R_{ij}^3})((\widetilde{\mathbf{F}}^{d1}_j+\widetilde{\mathbf{F}}^{d2}_j+\widetilde{\mathbf{F}}^{d3}_j)\cdot\widehat{\mathbf{R}}_{ij})\widehat{\mathbf{R}}_{ij}], \tag{4.5}$$

where $\widehat{\mathbf{R}}_{ij}$ is the unit vector in the $\widetilde{\mathbf{R}}_{ij}$ direction and from Equation (4.1), $\mathbf{u}_i^{\infty}=B\sin(2\theta_i)\vec{t_\theta}$ is the electrohydrodynamic flow induced about the drop. The rotation vector is given by

$$\widetilde{\mathbf{\Omega}}_i=\widetilde{\mathbf{T}}^E_i+\sum_{j\neq i}\left[-\frac{\widetilde{\mathbf{T}}^E_j}{2R_{ij}^3}-\frac{3}{2R_{ij}^3}(\widetilde{\mathbf{T}}^E_j\cdot\widehat{\mathbf{R}}_{ij})\widehat{\mathbf{R}}_{ij}-\frac{6(\widetilde{\mathbf{F}}^{d1}_j+\widetilde{\mathbf{F}}^{d2}_j+\widetilde{\mathbf{F}}^{d3}_j)\times\widehat{\mathbf{R}}_{ij}}{8R_{ij}^2}\right], \tag{4.6}$$

with

(4.7)

$$\widetilde{\mathbf{F}}^{d1}_i=\frac{2}{3}\widetilde{\mathbf{P}}_i\cdot\nabla\widetilde{\mathbf{E}}_{ap}(\tilde{\mathbf{x}}_i),$$

$$\widetilde{\mathbf{F}}^{d2}_i=-\sum_{j\neq i}\frac{2}{R_{ij}^4}[(\widetilde{\mathbf{P}}_i\cdot\widehat{\mathbf{R}}_{ij})\widetilde{\mathbf{P}}_j+(\widetilde{\mathbf{P}}_j\cdot\widehat{\mathbf{R}}_{ij})\widetilde{\mathbf{P}}_i+(\widetilde{\mathbf{P}}_i\cdot\widetilde{\mathbf{P}}_j)\widehat{\mathbf{R}}_{ij}-5(\widetilde{\mathbf{P}}_j\cdot\widehat{\mathbf{R}}_{ij})(\widetilde{\mathbf{P}}_i\cdot\widehat{\mathbf{R}}_{ij})\widehat{\mathbf{R}}_{ij}],$$

$$\widetilde{\mathbf{F}}^{d3}_i=\frac{1}{9}\widetilde{\mathbf{Q}}_i:\nabla\nabla\widetilde{\mathbf{E}}_{ap}(\mathbf{x}_i),\quad \widetilde{\mathbf{F}}^{rep}_{ij}=-Ce^{-20(R_{ij}-2)}\widehat{\mathbf{R}}_{ij}.$$

The dimensionless electric torque is

(4.8)

$$\widetilde{\mathbf{T}}^E_i=\frac{1}{2}\left(\widetilde{\mathbf{P}}_i\times\widetilde{\mathbf{E}}_{ap}(\mathbf{x}_i)+(\widetilde{\mathbf{Q}}_i\cdot\nabla)\times\widetilde{\mathbf{E}}_{ap}\right)-\frac{1}{2}\widetilde{\mathbf{P}}_i\times\sum_{j\neq i}\left(\frac{1}{|\widetilde{\mathbf{R}}_{ij}|^3}\mathbf{\Pi}\cdot\widetilde{\mathbf{P}}_j+\nabla\frac{\widetilde{\mathbf{R}}_{ij}\widetilde{\mathbf{R}}_{ij}:\widetilde{\mathbf{Q}}_j}{|\widetilde{\mathbf{R}}_{ij}|^5}\right)$$

$$+\frac{1}{2}(\widetilde{\mathbf{Q}}_i\cdot\nabla)\times\sum_{j\neq i}\frac{1}{|\widetilde{\mathbf{R}}_{ij}|^3}\mathbf{\Pi}\cdot\widetilde{\mathbf{P}}_j,$$

and $\widetilde{\mathbf{F}}^{rep}_{ij}$ is the assumed interparticle replusive force. Chapter 2 assumed a polynomial in the separation distance between particles with a sharp cut off for large separations. Here we have chosen a continuous form of the repulsive force which is easier to program and accomplishes the same task. The non-dimensional coefficients in the above equations are

$$\begin{aligned} B &= \chi \frac{9R_0\epsilon_d}{10a\epsilon_m(2+\frac{\sigma_d}{\sigma_f})^2}\left[\mu_m \frac{1-\frac{\epsilon_f\sigma_d}{\epsilon_d\sigma_f}}{\mu_d+\mu_f}\right], \quad C = \frac{\beta}{6\pi a^2\epsilon_m E_R^2}\left(\frac{E_R^2}{E_0^2}\right) = \beta_R\left(\frac{E_R^2}{E_0^2}\right), \\ D &= \frac{t_{ehd}}{\tau_{MW}} = \frac{\mu_m}{\epsilon_m E_0^2\tau_{MW}}, \quad D' = \frac{t_{ehd}}{\tau'_{MW}} = \frac{\mu_m}{\epsilon_m E_0^2\tau'_{MW}}. \end{aligned}$$

Here E_R is a reference applied electric field.

Particle rotation is induced by the flow and electric field. In a uniform applied electric field, particles in a homogeneous fluid can rotate above a threshold electric field due to the Quincke effect [**28**]. The critical field strength for an isolated particle as been calculated for both uniform [**33, 47**] and nonuniform electric field strengths in chapter 2. For a uniform field it is given by

$$E_c = \sqrt{\frac{2\mu_m}{\epsilon_m\tau_{mw}(\epsilon_{cm}-\sigma_{cm})}}. \tag{4.9}$$

Our aim is to simulate the experimental results of Ouriemi and Vlahovska [**12, 77**] and to make more general statements about the effects of particle number and electric field on a partially coated drop. To this end, we focus on polyethylene particles on a silicon oil drop in castor oil. With this in mind, we set $\epsilon_p = 2.25\epsilon_0$, $\epsilon_d = 2.8\epsilon_0$, and $\epsilon_f = 4.7\epsilon_0$, where ϵ_0 is the permittivity of free space. In addition we set $\mu_d = 0.05$ $Pa\,s$, $\mu_f = 0.69$ $Pa\,s$, $\sigma_d = 3.6\times10^{-12}\,S/m$, $\sigma_f = 3.8\times10^{-11}\,S/m$, and we set $\sigma_p \sim 0$. This allows us to set $\sigma_{cm} = -1/2$ and $\sigma'_{cm} = -1/3$. If more conductive metals (silver or aluminum) are considered we set $\sigma_{cm} = 1$ and $\sigma'_{cm} = 1/2$. In addition, we have set $E_R = 200$ V/mm, $a = 50\mu$m, $R_0 = 2.5mm$, and $\beta_R = 1$. We have introduced the damping factor χ into the definition of the parameter B. One can think of this as representing the effect of the applied flow on the particle dynamics for our complex problem beyond what can be expected for a single particle in a homogeneous flow. In our calculations we have set $\chi = 1/20$, more will be said later about this choice.

Since the particle motions are restricted to a spherical surface, we need to finally project the translational vector velocity in the tangential direction. Using spherical coordinates θ (polar angle measured from the z axis) and ϕ (azimuthal angle), the trajectory equation (in dimensionless coordinates) is given by,

$$\begin{aligned} \frac{d\theta_i}{dt} &= (\mathbf{u}_i \cdot \hat{\theta}) \\ \frac{d\phi_i}{dt} &= \frac{1}{\sin\theta_i}(\mathbf{u}_i \cdot \hat{\phi}), \end{aligned}$$

where $\hat{\theta}$ and $\hat{\phi}$ are unit vectors in the θ and ϕ directions, respectively. This completes the description of our model.

4.3. Simulation Results

The model proposed in the previous section consists of a system of $2N$ ordinary differential equations for the particle positions along the spherical drop interface, θ_i, ϕ_i, $i = 1, ..., N$, the $3N$ ODE's for the components for each particle dipole moment $\mathbf{P_i}$, and $5N$ ODE's for the independent components of the quadrupole moment $\mathbf{Q_i}$, giving a total of $10N$ ODE's to solve. Note that $\mathbf{Q_i}$ is symmetric with zero trace. In addition, the rotation vector $\mathbf{\Omega_i}$ and the electric torque $\mathbf{\Gamma_i}$ must be calculated for each particle. Each ODE at particle i includes a contribution from each of the other particles. Our solution approach was to solve this system using the Runge-Kutta-Fehlberg (RKF) adaptive time stepping method on a GPU parallel computing system. This proved to be a very efficient approach which allowed for shared memory, and the simultaneous solution of the ODEs on each of the GPU's cores. The error tolerance was set to 10^{-4} with an initial time step of 10^{-4}.

The low conductive particle case will be considered in Sections 4.3.1-4.3.3. In this case Qunicke motion is possible since $\epsilon_{cm} - \sigma_{cm} = -0.154 + 0.5 = 0.346 > 0$. In Section 4.3.4 we consider the high particle conductivity case where $\epsilon_{cm} - \sigma_{cm} = -0.154 - 1.0 = -1.154$ and by equation 4.9 there is no critical electric field strength for Quincke motion.

4.3.1. Introductory Examples

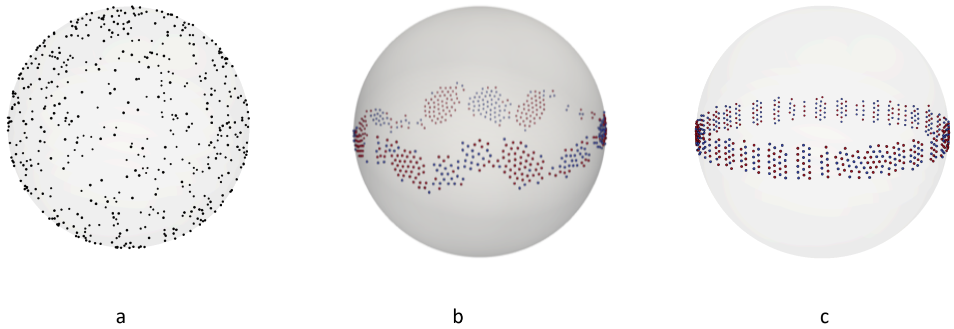

Figure 4.2. 512 particles on a spherical drop. The particle size is for illustrative purposed. Large particle are on the near face of the 3D sphere while small particles are projections from the rear of the sphere. a. Initial random distribution. b. Particle distribution at $t = t_f$ with $E_0 = 200V/mm$. Red particles are rotating clockwise, blue particles are rotating counter-clockwise.c .Particle distribution at $t = t_f$ with $E_0 = 100V/mm$

All parameter values are given in the above sections except for the strength of the applied electric field E_0 and N the number of particles. Solutions as a function of each of these parameters will be given below. E_0 will be given in dimensional units of $Volts/mm$. Initially the particles are randomly distributed on the surface of the spherical drop. An example of an initial distribution is given in Fig. 4.2a. Different initial data give slight differences in the overall quantitive dynamics but not in the qualitative dynamics, e.g., how a solution with a given set of parameter values will look at an instant in time. Besides the particle positions the initial values of the dipole and quadrupole moments were set to zero. All runs were ran out to $t_f = 15000$ dimensionless time units. Other times were tested but this dimensionless time appeared to give reasonable and consistent predictions for the range of parameters considered here. Note that the scaling implies that the dimensional time is proportional to t divided by the applied electric field strength squared, i.e., E_0^2. Hence results presented below for $E_0 = 400V/mm$ are presented at a dimensional time four times earlier than results for $E_0 = 200V/mm$. Our choice of t_f was taken so that the results presented for the largest applied fields appeared to have stabilized into a quasi-steady state (there are still random fluctuations) at the time the results are presented.

Figure 4.2b shows the particle positions on the drop surface at time t_f for $N = 512$ particles and an applied field of $E_0 = 200V/mm$. Since the strength of the applied field is greater than the critical field for Quincke rotation, i.e., $E_0 > E_c$, we expect the particles to rotate. The sign of the scalar $\zeta = \widetilde{\mathbf{\Omega}}_i \cdot \hat{\mathbf{n}}_i$ indicates the rotation of each particle relative to the normal of the interface. To represent this rotation we color each particle either red ($\zeta > 0$) for a clockwise rotation or blue ($\zeta < 0$) for a counter-clockwise rotation. Note that the particles have evolved into a oscillatory belt like structure around the equator of the drop. Although particles with different rotations are scattered about the band, there appears to be a clustering of particles with the same rotation about the normal to the drop interface. A time evolution of the initial data evolves in 3 stages: (1) the applied flow field forces all the particles to move towards the equator and form a belt like structure. The initial particle rotation is determined by Equation 4.6. Since the initial dipole and quadrupole moments are assumed to be zero, the initial rotation in this model depends on the random initial location of each particle and the inter-particle repulsive force given in Equation 4.7. Because of this the particle rotations appear to be randomly distributed around the equator; (2) once the uniform belt is formed there is an oscillation of the belt about the equator with a random distribution of particle rotations; (3) the particles begin to cluster into regions with similar rotations as illustrated in Fig. 4.2b. This is a very dynamic belt which is continuously evolving both on the particle scale with particles moving between clusters and changing the sign of ζ, plus evolving on the scale of the drop radius with cluster moving around the diameter of the drop. Different initial data could result in a different specific picture of the particles at a given instant in time, but the qualitative dynamics over long times is similar. The amplitude and period of oscillation is clearly the most striking visual observation for the figure. How the strength of the field and particle number impact these quantities will be investigated below.

Figure 4.2c. shows the particle positions on the drop surface at time t_f for $N = 512$ particles and an applied field of $E_0 = 100V/mm$. The strength of the applied field is below the critical field for Quincke rotation. Because of this the particles appear to form periodic and line structures near the equator in their steady state. The dynamic pictures show some particle motion with particles occasionally moving between neighboring strictures, but the overall shape is retained in time. The particles still have a colored rotation because we apply the color due to the sign of ζ and not its magnitude, but it is small and can be ignored. Notice that where clusters of particles exist there is a hexagonal like packing. The width and the interparticle spacing is dependent of the applied electric field strength E_0 which directly controls the strength of the applied flow field, and the number of particles N. It might be expected that a stronger applied flow field would compress the particles, even if there was significant rotation.

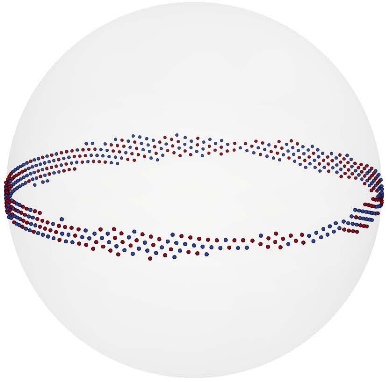

Figure 4.3. Particle distribution at $t = t_f$ for $N = 512$ particles with $E = 200V/mm$. The damping parameter $\chi = 1.0$.

.

In our model the strength of the applied flow field is controlled by the damping factor χ. We have set $\chi = 1/20$ in all reported results because with this value our computational results come closest to reproducing the experimental results reported in the work of Ouriemi and Vlahovska [**12, 77**]. To illustrate this in Figure 4.3 we plot the particle positions on the drop surface at time t_f for $N = 512$ particles and an applied field of $E_0 = 200V/mm$, but with a large damping factor of $\chi = 1$. Notice that unlike the results in Figure 4.2b for $\chi = 1/20$, the particles are now strongly confined to a belt about the equator of width approximately 3 particles in depth. This belt is in a (quasi-) steady state with little particle motion. The particles rotate but because of the strength of the flow there is little spacial motion. This steady shape with a hexagonal particle packing is similar to the low applied field strength case presented in figure 4.2c but unlike that case the particles are forced into a more narrow width belt. Although we admit that the choice of χ is somewhat arbitrary, chosen to reproduce as best as possible the predictions of a given set of experiments, we do claim that with this choice of damping parameter, the overall qualitative behavior of a partially coated drop with E_0 and N is determined. Additional research is needed to relate χ to the experimental parameters.

4.3.2. Impact of Particle Coverage and Electric Field

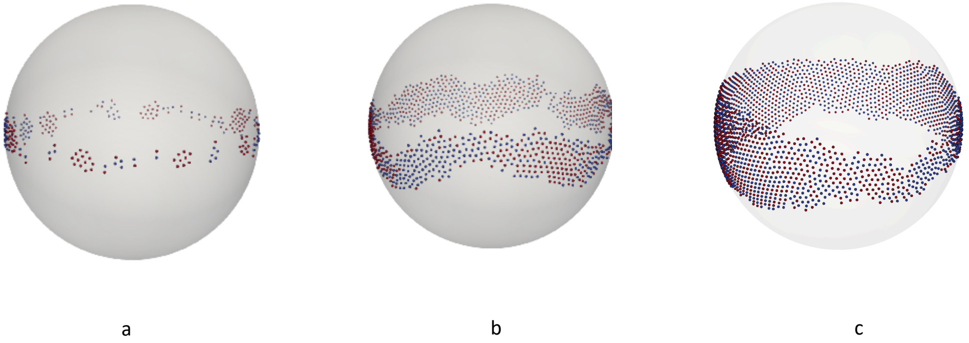

Figure 4.4. $E_0 = 200V/mm$ on a spherical drop. Red particles are rotating clockwise, blue particles are rotating counter-clockwise. a. $N = 256$, $t = t_f$. b. .$N = 1024$ particles, $t = t_f$. c .$N = 2048$ particles, $t \approx t_f$.

Examples of changing the number of particles N along the interface are given in Figure 4.4a for $N = 256$ and in Figure 4.4b for $N = 1024$ both with $E_0 = 200V/mm$. In Figure 4.4a we find that decreasing the particle density allows for clusters of particles with similar rotations to occur. This is similar to the experimental observations of Ouriemi and Vlahovska [**12, 77**] for low particle coverage. Comparing to the $N = 512$ case shown in Figure 4.2b we might have expected a continuous belt but the decrease in particle number and the fact that we have not changed the applied force from the flow field, since it depends in E_0, has allowed for clusters of the same rotation, and height similar to those in Figure 4.2b to exist. Increasing the particle number to $N = 1024$ appears to have two effects. The particles still appear in a continuous band as in the $N = 512$ case, but the wavelength of the band oscillation appears to have increased, and clustering of the particles along the sides of the bands is more noticeable. The distribution of particles now appears to be evenly distributed. Both of these cases are very dynamic, with the clusters in the $N = 256$ under constant rotation, and the band in the $N = 1024$ case doing an oscillatory motion.

As the number of particles continues to increase, the integrity of the belt structure degrades. An example is given in Figure 4.4c for $N = 2048$ and $E_0 = 200V/mm$. At this field strength, oscillations and particle circulation was observed for the lower values of N, but now, because of the large number of particles a steady state structure can be observed in regions. As the particles appear to collect in a region the hexagonal like structure appears in spots but fault lines are observed where there is a slight rotation of the basic structure. These fault lines are expected to be caused by the curvature of the drop surface since a uniform packing of the particles is not allowed as we increase from the equator to the poles. We also see the thinning of the belt in regions with an active transport of particles. This is just a snapshot in time but what is clear is that a steady state oscillatory like belt structure is not observed. It is possible that such a structure could exist if the calculation were continued further in time, but we have not observed it. Because of this, we limit any general conclusion below to the behavior of the particle belts to cases where N is less than or equal to 1024. A more improved model may be necessary to make general conclusions about higher density partially coated drops.

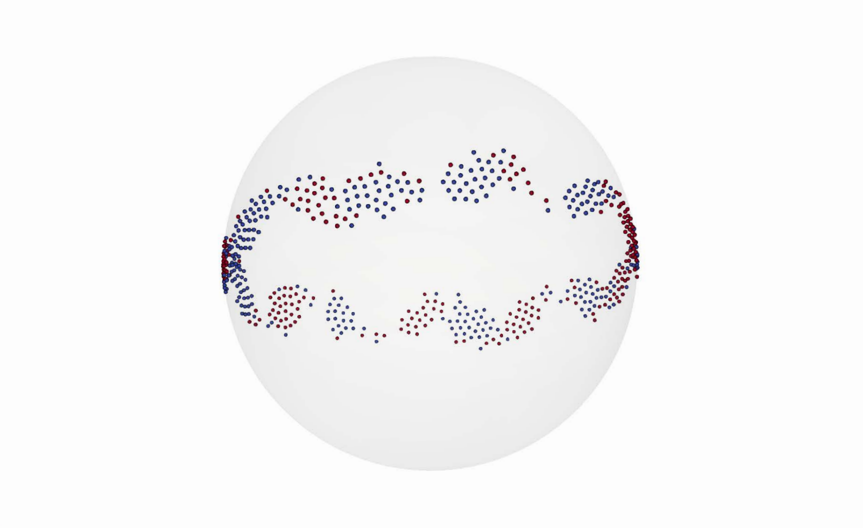

Figure 4.5. Particle distribution at $t = t_f$ for $N = 512$ particles with $E_0 = 400V/mm$
.

Increasing the electric field strength can be expected to decrease the amplitude of the oscillation because it increases the applied flow strength. This is illustrated in Figure 4.5 where $N = 512$ and $E_0 = 400V/mm$ and should be compared to the results in Figure 4.2b for $E_0 = 200V/mm$. There also appears to be a slight change in the particle belt period. These results are typical for our model with other values of particle number N. Care needs to be taken in increasing the applied electric field strength in our model. It has been observed experimentally that as the applied field strength increases, the drop becomes unstable and can deviate significantly from the steady spherical shape assumed here. Examples can be found in the experimental results of Ouriemi and Vlahovska [**12, 77**] where both steady shape deformations and wobbling drops are illustrated. In the Ouriemi and Vlahovska study of silicon oil drops in castor oil, $\gamma = 4.5mN/m$. They considered partially coated drops for $0 < Ca < 5$, where for the small values of Ca they observed steady state spherical drop shapes, while for slightly larger values the drops became oblate and prolate steady shapes up to $Ca \approx 1.5$. For larger values of Ca the drops became unstable and started to wobble. In our analysis, using the values for silicon oil drops in castor oil we have that for E_0 between $100V/mm$ and $400V/mm$, that $0.23 < Ca < 3.70$. Hence while we can expect the spherical drop approximation to be good for the $E_0 = 100V/mm$ ($Ca = 0.23$) or $E_0 = 200V/mm$ ($Ca = 0.92$) cases discussed above, for $E_0 = 400V/mm$ ($Ca = 3.70$) the drop is probably unstable and we present these results primarily to illustrate what to expect with the particle dynamics as the applied electric field is increased.

4.3.3. Impact of External Field Strength

The above results give us a qualitative picture of how varying the applied electric field and the number of particles impact the dynamics of the belt of particles along the equator of the drop. To get a more quantitative behavior we examine next how both applied electric field and particle number impact the belt width and the number of peaks (the wavelength) along the equatorial belt.

The amplitude of the oscillation A_θ can be simply defined as the angle between the maximum distance of all particles along the $z-$direction minus the minimum z value. Clearly the answer will depend on the time selected for this measurement. Our approach was to average this measurement over an interval of saved time snapshots, approximately one unit in time. Since the Runge-Kutta-Fehlberg (RKF) is an adaptive time stepping method with the time step variable, the results (a snapshot) were usually saved at times slightly larger than one unit, and hence there were less that 15000 particle time snapshots saved per run. To compute A_θ the first $t_s = 5000$ snapshots were ignored, and the rest up to t_f were included in the averaging. Increasing t_s did have some effect on the average

A_θ but the variation was within the error presented in the plots below. An average over a minimum of 20 runs were done for each E_0 and N value for different random initial data. The error bars in the plots below are a result of these different cases.

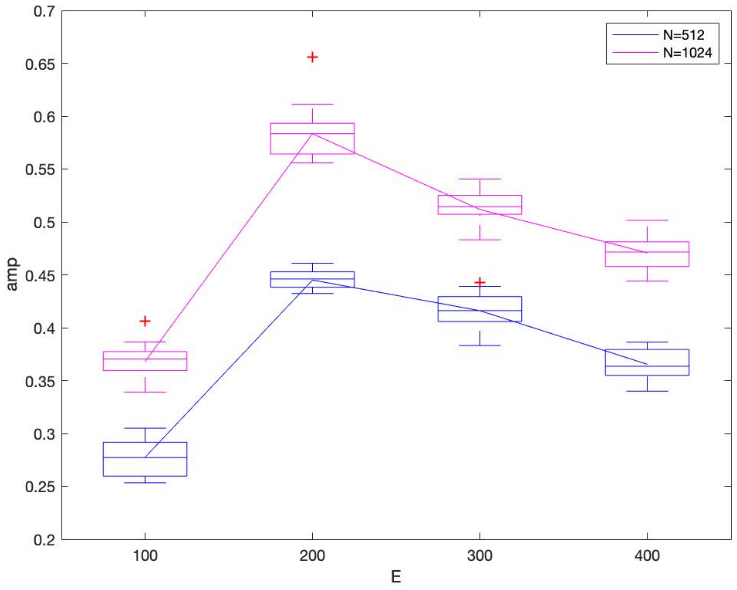

Figure 4.6. Amplitude of the angle of oscillation A_θ in radians as a function of electric field strength E_0 for $N = 512$ and 1014 particles.

In Figure 4.6 we plot A_θ as a function of E_0 for both $N = 512$ and $N = 1024$. The plots were made using the Matlab function *boxplot* with the central mark indicating the median, and the bottom and top edges of the box indicating the $25th$ and $75th$ percentiles, respectively. Although some variation exists in the data, the trend is obvious. As noted earlier, $E_0 = 100V/mm$ is below the Quincke threshold E_c and we get a tight packing of the particles about the equator. As E_0 is increased above E_c the belt begins to oscillate and A_θ suddenly increases. Further increase in E_0 decreases the amplitude of oscillation. This is expected since the the magnitude of the applied flow field increases with E_0. We also find that increasing N increases A_θ, which may be expected since more particles are trying to collect about the equator.

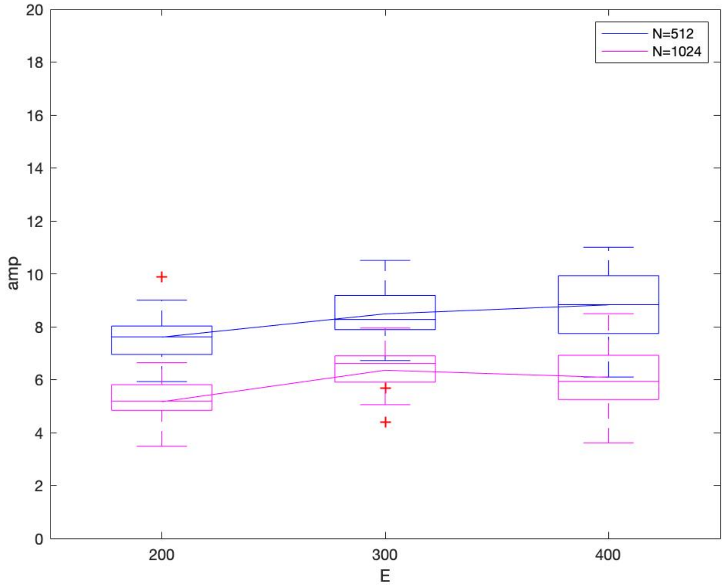

Figure 4.7. Wave number of maximum amplitude A_w as a function of electric field strength E_0 for 512 and 1014 particles

The wavelength of the belt oscillation is another quantity of interest. Although we could visually estimate this value from the snapshot of the particle distribution at time t_f, we decided to find an average value in a manner similar to how the average A_θ was calculated. The same data sets and times were analyzed as for A_θ. At each time snapshot, a curve for the average shape of the belt was found as follows. The drop was divided into 80 sections in the ϕ direction of size $2\pi/80$. In each section the average particle height was found. If no particles were within a section, the average was set to 0. These points were Fourier transformed and the wave number with the maximum amplitude was identified, A_w. As in the calculation of A_θ this was an average value determined for all time snapshots greater than 5000, and these values were averaged over 20 runs with random initial data. The results as a function of E_0 and for $N = 512$ and 1024 as plotted in figure 4.7. The low value of $E_0 = 100V/mm$ was not plotted since it formed an approximately uniform belt.

Figure 4.7 suggests that the wavelength of oscillation is insensitive to E_0 but it does depend on N. In particular, a smaller value of N gives a higher wavenumber, or smaller wavelength. This is consistent with the visual results presented in Figures 4.2 and 4.4.

4.3.4. Very Conductive Particles

An example of a highly conductive particle case is presented in Figure 4.8 at time t_f for $N = 512$ and $E_0 = 200V/mm$. In this case Qunicke motion is not predicted and we do not observe it. We do find particle chaining along the equation. This is an expected phenomena since now the polarization of each particle is parallel to the direction of the applied electric field. Depending on the applied field strength increasing particle density either lengthens the chain length or adds to the number of chains along the equator. There is some observed particle dynamics at these long times with chains growing or shortening. Some of this dynamics is due to numerical noise in the calculations, and some is due to the quasi-stability of a particular chain.

4.4. Conclusion

A model was developed to simulate the collective dynamics of colloids trapped at the interface of a drop placed in a uniform DC electric field. It was assumed that the particles were constrained to move on a sphere, representing the drop, and replaced the two-phase drop-suspending fluid system by an effective medium with properties that were

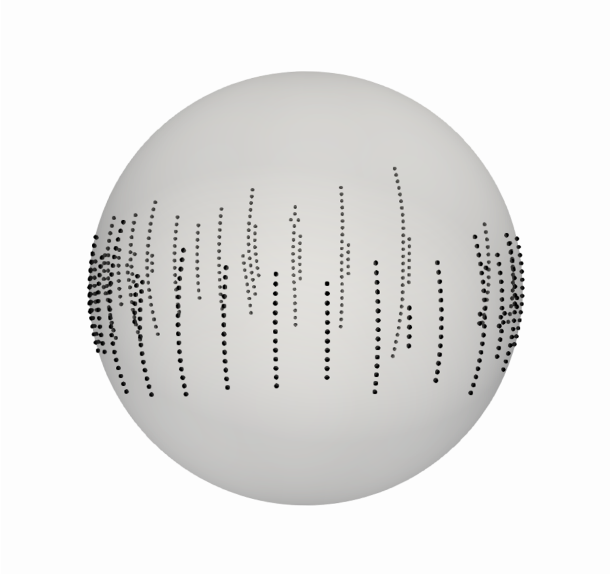

Figure 4.8. Steady state 512 particle distribution. High conductivity. $E_0 = 200V/m$

the average of the drop and suspending fluid. The model accounted for the electric field driven flow within the drop and suspending fluid, particle-particle electrostatic interaction, and the particle motion and rotation due to the induced flow and the applied electric field. The electrostatic interactions are computed by approximating the particles by dipoles and quadrupoles. The hydrodynamic interactions are accounted by reflections accurate to $O(d/R_0)^4$ in the ratio between the interparticle separation d and the drop radius R_0. Despite our modeling simplifications, the model captures the experimentally observed particle assemblies such as chains, bands and dynamic vortices around the equator. Specifically we found that the model predicts the formation of chains in the case of conducting particles and an undulating band around the equator in the case of dielectric particles. In the case of non-conducting particles, we showed that in the presence of Quincke rotation, the amplitude of the undulations of the observed equatorial particle belt increases with particle concentration but decreases with electric field strength, and that the wavelength of the undulations appears independent of the applied field strength. Our simulations also show that with increasing particle coverage or applied field strength isolated particle clusters become continuous belts with possible rotating clusters within the belts. Given that the strength of the hydrodynamic Taylor flow increases with electric field strength, the belt formation is not unexpected as the field strength is increased.

Although the model seems to qualitatively capture the observed dynamics of the experiments, improvements are needed for quantitative predictions. For example, a better modeling of the electrohydrodynamic force interaction between particles which accounts for the change in both fluid and electric properties across the fluid interface could impact specific predictions. Allowing for drop deformation due to the applied field could have a significant impact on the predictions with increasing electric field strength. Also missing here is the impact of the three phase contact line at the particle-fluid-fluid intersection. Future work will focus on these and other improvements in the modeling.

CHAPTER 5

Conclusion

To study the electrohydrodynamic behaviours of colloidal spheres in different fluid media and under different electric field, in Chapter 2, we start with a model to investigate the electrc-driven dynamics of particles in homogeneous fluid. Our theory is built on the Taylor-Melcher leaky dielectric model, which assumes ohmic conduction in the bulk and creeping flow. Considering an applied field with spatial variations much larger than the inter-particle spacing and the radius of the spheres, particle polarization is approximated by the dipole and quadrupole moments. We focus on an applied linear electric field in which case the approximation is exact. For the steady state of single sphere, we identify a necessary condition for when the nonuniform field induces Quincke rotation. We find that the threshold for electorotation in a linear field is lower that in the uniform field case. Increasing the electric field strength, makes the particle dynamics more complex: while Quincke electrorotation is characterized by steady spinning around the particle center, in stronger fields time-dependent orbiting motion around the minimum field location is observed. Then we generalize the model to consider multi-particle simulations in spatially slowly varying applied electric fields. The electrostatic interactions between particles include dipole-dipole and dipole-quadrupole interactions which are naturally introduced from the dielecropheritc force calculation. Our numerical calculations show intricate trajectories in the case of pairs, and chain-like assemblies in the case of many particles.

In Chapter 3, we analyze the electric forces on stationary spherical particles trapped at a fluid-fluid interface, under either a normal or tangential uniform electric field. We formulate the original electrostatic problem into integral equations for the electric potential by transforming into toroidal coordinates and then applying the Mehler-Fock integral transform. The resulting equations are solved numerically and asymptotically. We find that the particle experiences only a normal force in both cases. The analysis of the local field in the neighborhood of the contact line shows that the same integrable singularity occurs in both cases. In order to determine the interaction force between two particles resting on the interface, we consider the limit of widely separated particles, i.e., the distance between them is much larger than their radii. As a first step, we identify the far field asymptotic behavior of the electric potential of the first particle in the neighborhood of the second particle. The leading order behavior includes both dipole and quadrupole contributions. Once the dipole and quadrupole terms are known, the far field interaction force between two particles is found and shown to depend on the interparticle distance as R_0^{-4}. The force coefficients can be found analytically in the perfect dielectric case, but must the be calculated numerically for the leaky dielectric case. We show that the leading order force between particles is always repulsive for perfect dielectrics and governed by dipole-dipole interactions. We also show that for leaky dielectric particles the force can be attractive when the quadrupole terms are significant. However, in many cases when the force between leaky dielectric particles is repulsive, we show that it can be well-approximated by only dipole-dipole interactions.

In Chapter 4, we built a model to simulate the collective dynamics of colloids trapped at the interface of a drop placed in a uniform DC electric field. We generalize the multipole approach in previous chapters to calculate the forces between particles and determine the collective motion and assembly of colloidal spheres trapped at a drop interface in a uniform applied electric field. The electrostatic interactions are computed by approximating the particles by dipoles and quadrupoles. The hydrodynamic interactions are accounted by reflections accurate to $O(d/R_0)^4$ in the ratio between the interparticle separation d and the drop radius R_0. The model captures the experimentally observed particle assemblies such as chains, bands and dynamic vortices around the equator. Specifically we found that the model predicts the formation of chains in the case of conducting particles and an undulating band around the equator in the case of dielectric particles. In the case of non-conducting particles, we showed that in the presence of Quincke rotation, the amplitude of the undulations of the observed equatorial particle belt increases with particle concentration but decreases with electric field strength, and that the wavelength of the undulations appears independent of the applied field strength. Our simulations also show that with increasing particle coverage or applied field strength isolated particle clusters become continuous belts with possible rotating clusters within the belts. Given that the strength of the hydrodynamic Taylor flow increases with electric field strength, the belt formation is not unexpected as the field strength is increased.

Allowing for drop deformation due to the applied field could have a significant impact on the predictions with increasing electric field strength. Also missing in the study of Chapter 4 is the impact of the three phase contact line at the particle-fluid-fluid intersection. Future work will focus on these improvements in the modeling.

References

[1] W. Ramsden. Separation of solids in the surface-layers of solutions and suspensions (observations of surface-membranes, bubbles, emulsions, and mechanical coagulation) - preliminary account. Proc. R. Soc. London, 72:156–164, 1903.

[2] S.U.. Pickering. Emulsions. J. Chem. Soc. Trans.., 19:2001–2021, 1907.

[3] J. Wu and G.-H.. Ma. Recent studies of pickering emulsions: Particles make the difference. Small, 12(34):4633–4648, 2016.

[4] A. D. Dinsmore, M. F. Hsu, M. G. Nikolaides, M. Marquez, A. R. Bausch, and D. A. Weitz. Colloidosomes: Selectively permeable capsules composed of colloidal particles. Science, 298:1006–1009, 2002.

[5] A. F. Routha Q. Sun, J-F. Chen. Coated colloidosomes as novel drug delivery carriers. Expert Opinion on Drug Delivery, 16:903–906, 2019.

[6] P. B. Binks. Particles as surfactants - similarities and differences. Current Opinion in Colloid & Interface Science, 7:21–41, 2002.

[7] P. Aussillous and D Quere. Liquid marbles. Nature, 411:924–927, 2001.

[8] R. Aveyard, B. P. Binks, and J. H. Clint. Emulsions stabilised solely by colloidal particles. Advances in Colloid and Interface Science, 100:503–546, 2003.

[9] E. Dickinson. Food emulsions and foams: Stabilization by particles. Current Opinion in Colloid and Interface Science, 15:40–49, 2010.

[10] A. Jozefczak Z. Rozynek. Patchy colloidosomes - an emerging class of structure. European Physical Journal-Special Topics, 225:741–756, 2016.

[11] Paul Dommersnes, Zbigniew Rozynek, Alexander Mikkelsen, Rene Castberg, Knut Kjerstad, Kjetil Hersvik, and Jon Otto Fossum. Active structuring of colloidal armor on liquid drops. Nature Communications, 4:2066, 2013.

[12] Malika Ouriemi and Petia M. Vlahovska. Electrohydrodynamics of particle-covered drops. Journal of Fluid Mechanics, 751:106–120, jul 2014.

[13] Zbigniew Rozynek, Alexander Mikkelsen, Paul Dommersnes, and Jon Otto Fossum. Electroformation of Janus and patchy capsules. Nature Comm., 5, MAY 2014.

[14] A. Mikkelsen Z. Rozynek, K. Khobaib. Opening and closing of particle shells on droplets via electric fields and its applications. ACS Applied Materials & Interfaces, 11:22840–22850, 2019.

[15] M. Oettel and S. Dietrich. Colloidal interactions at fluid interfaces. Langmuir, 24(4):1425–1441, 2008. PMID: 18179271.

[16] PA Kralchevsky and ND Denkov. Capillary forces and structuring in layers of colloid particles. Current Opinion in Colloid and Interface Science, 6(4):383–401, AUG 2001.

[17] P. A. Kralchevsky and K. Nagayama. Lateral capillary forces between partially immersed bodies. In Particles at Fluid Interfaces and Membranes, pages 287–350. Elsevier, Netherlands, 2001.

[18] Lorenzo Botto, Eric P. Lewandowski, Marcello Cavallaro, Jr., and Kathleen J. Stebe. Capillary interactions between anisotropic particles. Soft Matter, 8(39):9957–9971, 2012.

[19] Venkateshwar Rao Dugyala, Santosh V. Daware, and Madivala G. Basavaraj. Shape anisotropic colloids: synthesis, packing behavior, evaporation driven assembly, and their application in emulsion stabilization. Soft Matter, 9(29):6711–6725, 2013.

[20] Marcello Cavallaro, Jr., Lorenzo Botto, Eric P. Lewandowski, Marisa Wang, and Kathleen J. Stebe. Curvature-driven capillary migration and assembly of rod-like particles. PNAS, 108(52):20923–20928, DEC 27 2011.

[21] N. C. Christov P. A. Kralchevsky M. P. Boneva, K. D. Danov. Attraction between particles at a liquid interface due to the interplay of gravity- and electric-field-induced interfacial deformations. Langmuir, 25:9129–9139, 2009.

[22] Krassimir D. Danov and Peter A. Kralchevsky. Forces acting on dielectric colloidal spheres at a water/nonpolar-fluid interface in an external electric field. 1. uncharged particles. Journal of Colloid and Interface Science, 405:278–290, 2013.

[23] Krassimir D. Danov and Peter A. Kralchevsky. Forces acting on dielectric colloidal spheres at a water/nonpolar fluid interface in an external electric field. 2. charged particles. Journal of Colloid and Interface Science, 405:269–277, 2013.

[24] G. I. Taylor. Disintegration of water drops in an electric field. Proc. Royal Soc. A, 280(1382):383–397, 1964.

[25] Geoffrey Taylor. Studies in Electrohydrodynamics. I. The Circulation Produced in a Drop by Electrical Field. Proceedings of the Royal Society of London. Series A. Mathematical and Physical Sciences, 291(1425):159 LP – 166, apr 1966.

[26] J.˜R. Melcher and G.˜I. Taylor. Electrohydrodynamics: A Review of the Role of Interfacial Shear Stresses. Annual Review of Fluid Mechanics, 1:111–146, 1969.

[27] D. A. Saville. Electrohydrodynamics: The Taylor-Melcher leaky dielectric model. Annu. Rev. Fluid Mech., 29:27–64, 1997.

[28] G. Quincke. Ueber rotation em im constanten electrischen felde. Ann. Phys. Chem., 59:417, 1896.

[29] A Cēbers, E Lemaire, and L Lobry. Electrohydrodynamic instabilities and orientation of dielectric ellipsoids in low-conducting fluids. Phys. Rev. E, 63(1):16301, dec 2000.

[30] E Lemaire and L Lobry. Chaotic behavior in electro-rotation. Physica A: Statistical Mechanics and its Applications, 314(1–4):663–671, nov 2002.

[31] Yu. Dolinsky and T Elperin. Electrorotation of a leaky dielectric spheroid immersed in a viscous fluid. Phys. Rev. E, 80(6):66607, dec 2009.

[32] Q. Brosseau, G. Hickey, and P. M. Vlahovska. Electrohydrodynamic quincke rotation of an ellipsoid. Phys. Rev. Fluids, 2:014101, 2017.

[33] D. Das and D. Saintillan. Electrohydrodynamic interaction of spherical particles under

Quincke rotation. Phys. Rev. E, 87(4), APR 29 2013.

[34] Yu. Dolinsky and T. Elperin. Dipole interaction of the Quincke rotating particles. PHYSICAL REVIEW E, 85(2, 2), FEB 27 2012.

[35] E. Lushi and P. M. Vlahovska. Periodic and chaotic orbits of micro-rotors in creeping flows. Journal of Nonlinear Science, 25:1111–1123, 2015.

[36] Antoine Bricard, Jean-baptiste Caussin, Nicolas Desreumaux, Olivier Dauchot, and Denis Bartolo. Emergence of macroscopic directed motion in populations of motile colloids. Nature, 503(7474):95–98, 2013.

[37] Antoine Bricard, Jean-baptiste Caussin, Debasish Das, Charles Savoie, Vijayakumar Chikkadi, Kyohei Shitara, Oleksandr Chepizhko, Fernando Peruani, David Saintillan, and Denis Bartolo. Emergent vortices in populations of colloidal rollers. Nature Communications, 6:1–8, 2015.

[38] M. Belovs and A. Cebers. Relaxation of polar order in suspensions with Quincke effect. Phys. Rev. E, 89(5), MAY 20 2014.

[39] K. Yeo, E. Lushi, and P. M. Vlahovska. Collective dynamics in a binary mixture of hydrodynamically coupled microrotors. Phys. Rev. Lett., 114:188301, 2015.

[40] Kyongmin Yeo, Enkeleida Lushi, and Petia M. Vlahovska. Dynamics of inert spheres in active suspensions of micro-rotors. Soft Matter, 12(25):5645–5652, 2016.

[41] Gasper Kokot, David Piet, George M. Whitesides, Igor S. Aranson, and Alexey Snezhko. Emergence of reconfigurable wires and spinners via dynamic self-assembly. Scientific reports, 5, MAR 26 2015.

[42] Alexey Snezhko. Complex collective dynamics of active torque-driven colloids at interfaces. Current Opinion Coloid and Interface Sci., 21(SI):65–75, FEB 2016.

[43] A. Cēbers. Bistability and “negative” viscosity for a suspension of insulating particles in an electric field. Phys. Rev. Lett., 92(3):034501, Jan 2004.

[44] E Lemaire, L Lobry, N Pannacci, and F Peters. Viscosity of an electro-rheological suspension with internal rotations. Journal of Rheology, 52(3):769–783, may 2008.

[45] H-F. Huang, M. Zahn, and E. Lemaire. Negative electrorheological responses of micro-polar fluids in the finite spin viscosity small spin velocity limit. i. couette flow geometries. J. Electrostatics, 69:442–455, 2011.

[46] N. Pannacci, E. Lemaire, and L. Lobry. Dc conductivity of a suspension of insulating particles with internal rotation. Eur. Phys. J. E, 28:411–417, 2009.

[47] Thomas B. Jones. Quincke Rotation of Spheres. IEEE Transactions on Industry Applications, IA-20(4):845–849, 1984.

[48] I Turcu. Electric field induced rotation of spheres. Journal of Physics A: Mathematical and General, 20(11):3301, 1987.

[49] H.~A. Pohl. The Motion and Precipitation of Suspensoids in Divergent Electric Fields. Journal of Applied Physics, 22:869–871, jul 1951.

[50] T B Jones and Masao Washizu. Multipolar dielectrophoretic and electrorotation theory. Journal of Electrostatics, 37(1):121–134, 1996.

[51] T B Jones. Basic theory of dielectrophoresis and electrorotation. IEEE Engineering in Medicine and Biology Magazine, 22(6):33–42, nov 2003.

[52] S. Kim and S. J. Karrila. Microhydrodynamics: Principles and Selected Applications. Butterworth-Heinemann, 1991.

[53] Kyongmin Yeo and Martin R Maxey. Simulation of concentrated suspensions using the force-coupling method. Journal of Computational Physics, 229(6):2401–2421, 2010.

[54] C. Pozrikidis. Particle motion near and inside an interface. J Fluid Mech., 575:333–357, 2007.

[55] A. Dörr and S. Hardt. Driven particles at fluid interfaces acting as capillary dipoles. Journal of Fluid Mechanics, 770:5–26, May 2015.

[56] A. Dorr, S. Hardt, H. Masoud, and H.A. Stone. Drag and diffusion coefficients of a spherical particle attached to a fluid-fluid interface. J. Fluid Mech., 790:607–618, 2016.

[57] M. G. Nikolaides, A. R. Bausch, M. F. Hsu, A. D. Dinsmore, M. P. Brenner, C. Gay, and D. A. Weitz. Electric-field-induced capillary attraction between like-charged particles at liquid interfaces. Nature, 420(6913):299–301, 11 2002.

[58] F Bresme and M Oettel. Nanoparticles at fluid interfaces. Journal of Physics: Condensed Matter, 19(41):413101, 2007.

[59] Paul Dommersnes, Zbigniew Rozynek, Alexander Mikkelsen, Rene Castberg, Knut Kjerstad, Kjetil Hersvik, and Jon Otto Fossum. Active structuring of colloidal armour on liquid drops. 4:2066 EP –, 06 2013.

[60] Malika Ouriemi and Petia M. Vlahovska. Electrohydrodynamics of particle-covered drops. Journal of Fluid Mechanics, 751:106–120, 2014.

[61] Alexander Mikkelsen, Jarosaaw Wojciechowski, Michal Rajaak, Juraj Kurimskae, Khobaib Khobaib, Ahmet Kertmen, and Zbigniew Rozynek. Electric field-driven assembly of sulfonated polystyrene microspheres. Materials, 10(4), 2017.

[62] Krassimir D. Danov and Peter A. Kralchevsky. Electric forces induced by a charged colloid particle attached to the water-nonpolar fluid interface. Journal of Colloid and Interface Science, 298(1):213–231, 2006.

[63] E. Lac and G. M. Homsy. Axisymmetric deformation and stability of a viscous drop in a steady electric field. J. Fluid. Mech, 590:239–264, 2007.

[64] R V Craster and Yu V Obnosov. Four-phase checkerboard composites. SIAM Journal on Applied Mathematics, 61(6):1839–1856, 2001.

[65] R. V. Craster and Yu V. Obnosov. Checkerboard composites with separated phases. Journal of Mathematical Physics, 42(11):5379–5388, 2001.

[66] Krassimir D Danov, Peter A Kralchevsky, and Mariana P Boneva. Electrodipping force acting on solid particles at a fluid interface. Langmuir, 20(15):6139–6151, jul 2004.

[67] Y. Hu, P.M. Vlahovska, and M.J. Miksis. Colloidal particle electrorotation in a nonuniform electric field. Phys. Rev. E, 97, 2018.

[68] R K. D. Danov, R. Dimova. Viscous drag of a solid sphere straddling a spherical or flat surface. Phys. Fluids, 12:2711–2722, 2000.

[69] M. Yeganeh Mohsen C. Maldarelli A. Dani, G. Keiser. Hydrodynamics of particles at an oil-water interface. Langmuir, 31:13290–13302, 2015.

[70] H. Masoud H. A. Stone A. Doerr, S. Hardt. Drag and diffusion coefficients of a spherical particle attached to a fluid-fluid interface. Journal of Fluid Mechanics, 790:607–618, 2016.

[71] J. Hemauer J. J. Feng J.-C. Loudet, M. Qiu. Drag force on a particle straddling a fluid interface: Influence of interfacial deformations. European Physical Journal E, 43:16, 2020.

[72] D. D. Joseph P. Singh. Fluid dynamics of floating particles. J. Fluid Mech., 530:31–80, 2005.

[73] J. Harting F. Jansen. From bijels to pickering emulsions: A lattice boltzmann study. Phys. Rev. E, 83:046707, 2011.

[74] J. Harting A. M. de Jong M. W. J. Prins S. Cappelli, Q. Xie. Dynamic wetting: status and prospective of single particle based experiments and simulations. New Biotechnology, 32:420–432, 2015.

[75] S. Nudurupati, M. Janjua, P. Singh, and N. Aubry. Electrohydrodynamic removal of particles from drop surfaces. Phys. Rev. E, 80:010402R, 2009.

[76] Edison Amah, Kinnari Shah, Ian Fischer, and Pushpendra Singh. Electrohydrodynamic manipulation of particles adsorbed on the surface of a drop. Soft Matter, 12:1663–1673, 2016.

[77] M. Ouriemi and P. M. Vlahovska. Electrohydrodynamic deformation and rotation of a particle-coated drop. Langmuir, 31:6298–6305, 2015.

APPENDIX A

Symmetries of the multipole moments

To satisfy the electric Laplace equation, the higher order multipole moments in the expansion of Eq. 2.1 retains certain symmetry properties and make the leaky-dielectric boundary equation Eq. 2.7 separable.

Using the symmetry of the quadrupole moment, $\mathbf{Q} = \mathbf{Q}^{\mathsf{T}}$, the trace of the cross product term $\mathbf{\Omega} \times \mathbf{Q}$ in Eq. 2.7 will be

$$\begin{aligned} tr(\mathbf{\Omega} \times \mathbf{Q}) &= \epsilon_{ikl}\Omega_k Q_{li} \\ &= \Omega_2 Q_{31} - \Omega_3 Q_{21} + \Omega_3 Q_{12} - \Omega_1 Q_{32} + \Omega_1 Q_{23} - \Omega_2 Q_{13} \\ &= 0. \end{aligned} \tag{A.1}$$

APPENDIX B

Mehler-Fock Integral Transform

The generalized Mehler-Fock integral transform pair of a function $B(u)$ [**62**], defined on $1 \leq u < \infty$, is given by

$$B(u) = \int_0^\infty P^k_{-1/2+i\tau}(u)\mathcal{C}(\tau)d\tau, \tag{B.1}$$

$$\mathcal{C}(\tau) = \frac{1}{\pi}\tau \sinh \pi\tau \; \Gamma(\frac{1}{2} - k + i\tau)\Gamma(\frac{1}{2} - k - i\tau) \int_1^\infty B(u)P^k_{-1/2+i\tau}(u)du. \tag{B.2}$$

Here $\mathcal{C}(\tau)$ is the transformed (or image) function defined on $0 \leq \tau < \infty$. $P^k_{-1/2+i\tau}(u)$ is the associated Legendre function of the first kind with complex index $-1/2 + i\tau$.

In all of our calculations we will set the argument of $\mathcal{C}$ as $u = \cosh\eta$. For the normal applied electric field problem, we need $k = 0$. Thus the inverse Mehler-Fock integral transform to determine $\mathcal{C}(\tau)$ is

$$\mathcal{C}(\tau) = \tau \tanh \pi\tau \int_0^\infty B(\cosh\eta)P^0_{-1/2+i\tau}(\cosh\eta)\sinh\eta \; d\eta. \tag{B.3}$$

For the tangential electric field, we take $k = 1$ and obtain

$$\mathcal{C}(\tau) = \frac{4\tau}{4\tau^2 + 1} \tanh \pi\tau \int_0^\infty B(\cosh\eta)P^1_{-1/2+i\tau}(\cosh\eta)\sinh\eta \; d\eta. \tag{B.4}$$

APPENDIX C

Functions in The Integral Equations of Section 3.2.3

These functions are needed in the definition of equations (3.52)-(3.53).

$$V_1(\tilde{\tau},\tau) = \frac{\tanh \pi\tau}{2} \sin \xi_0 \int_0^\infty \frac{K^0(\eta,\tau)K^0(\eta,\tilde{\tau})}{\cosh \eta - \cos \xi_0} \sinh \eta d\eta, \tag{C.1}$$

$$V_2(\tilde{\tau},\tau) = \frac{\tanh \pi\tau}{2} \sin (\xi_0 + \pi) \int_0^\infty \frac{K^0(\eta,\tau)K^0(\eta,\tilde{\tau})}{\cosh \eta + \cos \xi_0} \sinh \eta d\eta, \tag{C.2}$$

$$\begin{aligned} S_1(\tau) = {} & \frac{2^{3/2}}{3}(1-\gamma_{pl})[\cot \xi_0 \frac{\sinh (\pi - \xi_0)\tau}{\cosh \pi\tau} - 2\tau \frac{\cosh (\pi - \xi_0)\tau}{\cosh \pi\tau}] \\ & + (\gamma_{ul} - 1)2^{3/2}\tau \frac{\sinh (\pi - \xi_0)\tau}{\cosh \pi\tau} \coth \xi_0\tau \\ & + 2^{3/2}(1-\gamma_{ul})\tau \frac{\gamma_{ul} \sinh (\pi - \xi_0)\tau}{\cosh \pi\tau \sinh^2 \xi_0\tau[\gamma_{ul} \coth \xi_0\tau - \coth (\xi_0 - \pi)\tau]} \\ & + \int_0^\infty (\gamma_{ul} - 1)2^{3/2}\tilde{\tau} \frac{\sinh (\pi - \xi_0)\tilde{\tau}}{\cosh \pi\tilde{\tau}} V_1(\tilde{\tau},\tau) d\tilde{\tau}, \end{aligned} \tag{C.3}$$

$$\begin{aligned} S_2(\tau) = {} & \frac{2^{3/2}}{3}(\gamma_{lu} - \gamma_{pl})[-\cot (\xi_0 + \pi) \frac{\sinh \xi_0\tau}{\cosh \pi\tau} - 2\tau \frac{\cosh \xi_0\tau}{\cosh \pi\tau}] \\ & + 2^{3/2}(1-\gamma_{ul})\tau \frac{1}{\cosh \pi\tau \sinh \xi_0\tau[\gamma_{ul} \coth \xi_0\tau - \coth (\xi_0 - \pi)\tau]}, \end{aligned} \tag{C.4}$$

and

$$\begin{aligned} A_{21}(\tau) = {} & \frac{\gamma_{ul}}{\sinh^2 \xi_0\tau[-\coth (\xi_0 - \pi)\tau + \gamma_{ul} \coth \xi_0\tau]} \\ & - (\gamma_{pl} \coth \pi\tau + \gamma_{ul} \coth \xi_0\tau), \end{aligned} \tag{C.5}$$

$$A_{31}(\tau) = \frac{\gamma_{pl}}{\gamma_{ul}\sinh \pi\tau}$$

$$- \frac{1}{\sinh \xi_0\tau \sinh{(\xi_0 - \pi)\tau}[-\coth{(\xi_0 - \pi)\tau} + \gamma_{ul}\coth \xi_0\tau]}, \tag{C.6}$$

$$A_{22}(\tau) = \frac{1}{\sinh \xi_0\tau \sinh{(\xi_0 - \pi)\tau}[-\coth{(\xi_0 - \pi)\tau} + \gamma_{ul}\coth \xi_0\tau]}$$

$$- \frac{\gamma_{pl}}{\gamma_{ul}\sinh \pi\tau}, \tag{C.7}$$

$$A_{32}(\tau) = -\frac{1}{\sinh^2{(\xi_0 - \pi)\tau}[-\coth{(\xi_0 - \pi)\tau} + \gamma_{ul}\coth \xi_0\tau]}$$

$$+ (\gamma_{pl}\coth \pi\tau - \coth{(\xi_0 - \pi)\tau}). \tag{C.8}$$

APPENDIX D

Convergence tests on the numerical solution of far-field coefficients for Chapter 3

In this study, equations (3.52)-(3.53) are solved using uniformly spaced discretization and the calculation of the far-field coefficients in eqs. (3.88) and (3.89) are also calculated using uniform trapezoidal rule. Here we provide a convergence investigation on the far-field coefficient C_2^l at specific configurations. Note that even though it is difficult and tedious to conduct the numerical convergence on all parameter set, we assume the convergence results are valid for all interested configuration. And further convergence test can be conducted in the same way.

Suppose $\alpha = \pi/2$, $\gamma_{ul} = 4$ and we use 100 γ_{pl} values uniformly distributed in $[0, 30]$. Denote the solution vector of C_2^l as $\mathcal{V}$, and V_b is the best solution we obtain using the smallest grid size.

Table D.1. Convergence with respect to the grid size $\Delta\tau$. Integration upper bound $\tau_U = 60$.

Solution vector	$\Delta\tau$	$\|\|\mathcal{V}_i - \mathcal{V}_4\|\|$
$\mathcal{V}_1$	1/25	0.7760×10^{-3}
$\mathcal{V}_2$	1/50	0.0260×10^{-3}
$\mathcal{V}_3$	1/100	0.0008×10^{-3}
$\mathcal{V}_4$	1/200	NA

The convergence of table D.1 with respect to $\Delta\tau$ is fast and nearly to the $5th$ power. The rate in table D.2 with respect to the upper bound τ_U is slower but the absolute error is much smaller and could be negligible.

Table D.2. Convergence with respect to the integration upper bound τ_U. $\Delta\tau = 1/200$.

Solution vector	τ_U	$\|\|\mathcal{V}_i - \mathcal{V}_b\|\|$
$\mathcal{V}_5$	15	3.1834×10^{-8}
$\mathcal{V}_6$	30	2.7332×10^{-8}
$\mathcal{V}_4$	60	1.8380×10^{-8}
$\mathcal{V}_b$	120	NA

Therefore in our study we choose $\tau_U = 60$ and $\Delta\tau = 0.005$ and converged solutions are guaranteed.

APPENDIX E

Proving 3.113 using an analogy of the method by Danov and Kralchevsky, when $\gamma = \epsilon$, in a tangential field

In order to prove 3.113 analytically correct at the leading order when $\gamma = \epsilon$, we rearrange the coordinate system as shown in fig. E.1.

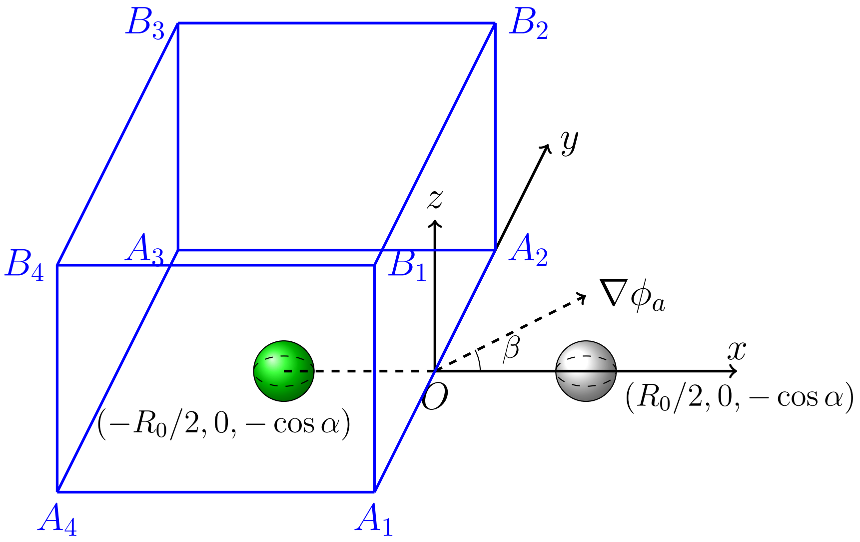

Figure E.1. Two widely separated particles at $(-R_0/2, 0, -\cos\alpha)$ and $(R_0/2, 0, -\cos\alpha)$, where $R_0 >> 1$. A general tangential field (parallel to $x - y$ plane) is imposed in the entire space. For simplicity, we assume the gradient of the applied potential $\nabla\phi_a$ inclines at an angle β with respect to the line connecting particle centers, as shown above. Parallel auxiliary planes are used for the derivation of inter-particle force.

Without losing any generality, assume the applied potential is $\phi_a = x\cos\beta + y\sin\beta$. Note that this setup is essentially equivalent to fig. 3.10 and does not change the expression of the inter-particle forces.

The electric forces on particle 1 at $(-R_0/2, 0, -\cos\alpha)$ can be calculated by

$$F_m^n = \iint_{S_n^1} \mathbf{\Sigma} d\mathbf{S} \cdot \mathbf{e_m}, \tag{E.1}$$

for $m = x, y$ and $n = u, l$. We firstly look at the force in x direction. In eq. (3.113), this force corresponds to F^{ax} . The Maxwell tensor $\mathbf{\Sigma}$ is defined the same as the force calculations before. Near the surface of particle 1, suppose the total potential above and below $x-y$ plane are ϕ_u and ϕ_l, respectively. Because $\nabla \cdot \mathbf{\Sigma} = \mathbf{0}$, using divergence theorem in the volume enclosed by the auxiliary cube $A_1A_2A_3A_4 - B_1B_2B_3B_4$, we obtain,

$$\begin{aligned} F_x^u =& \iint_{S_u^1} \mathbf{\Sigma} d\mathbf{S} \cdot \mathbf{e_x}, \\ =& - \iint_{A_{1,2,3,4}/S_I} \Sigma_{13} dA + \iint_{B_{1,2,3,4}} \Sigma_{13} dA \\ & - \iint_{A_{1,4}B_{1,4}} \Sigma_{12} dA + \iint_{A_{2,3}B_{2,3}} \Sigma_{12} dA \\ & - \iint_{A_{3,4}B_{3,4}} \Sigma_{11} dA + \iint_{A_{1,2}B_{1,2}} \Sigma_{11} dA, \end{aligned} \tag{E.2}$$

where S_I is the intersection region of particle 1 and $x - y$ plane. A_i and B_i denote the vertices of each integration rectangular.

Because the particles are assumed far away from each other (i.e. $R_0 >> 1$), the integration sides are also situated far from the particles. Hence Σ_{13} vanishes on $B_{1,2,3,4}$. Moreover, because $\Sigma_{12} = \cos\beta \sin\beta$ on both $A_{1,4}B_{1,4}$ and $A_{2,3}B_{2,3}$, the integrations on these two sides cancel each other. On $A_{1,2,3,4}/S_I$, when $\gamma = \epsilon$, the total potential at the flat interface must satisfy $\frac{\partial \phi_u}{\partial x} = \frac{\partial \phi_l}{\partial x}$ and $\epsilon_{ul} \frac{\partial \phi_u}{\partial z} = \frac{\partial \phi_l}{\partial z}$. Hence $\Sigma_{13}^u = \frac{\epsilon_u}{4\pi} \frac{\partial \phi_u}{\partial x} \frac{\partial \phi_u}{\partial z} = \frac{\epsilon_l}{4\pi} \frac{\partial \phi_l}{\partial x} \frac{\partial \phi_l}{\partial z} = \Sigma_{13}^l$. When we sum up the upper and lower contributions, they cancel each other.

Rewrite the potential at $A_{1,2}B_{1,2}$ as $\phi = \phi_a + \tilde{\phi}$, where $\tilde{\phi}$ is disturbance potential induced by particles. Now the integrations contributing to the force are,

$$
\begin{aligned}
F_x^u =& -\iint_{A_{3,4}B_{3,4}} \Sigma_{11} dA + \iint_{A_{1,2}B_{1,2}} \Sigma_{11} dA, \\
=& -\frac{\epsilon_u}{8\pi} \iint_{A_{3,4}B_{3,4}} [(\frac{\partial \phi_a}{\partial x})^2 - (\frac{\partial \phi_a}{\partial y})^2 - (\frac{\partial \phi_a}{\partial z})^2] dA \\
& + \frac{\epsilon_u}{8\pi} \iint_{A_{1,2}B_{1,2}} [(\frac{\partial \phi}{\partial x})^2 - (\frac{\partial \phi}{\partial y})^2 - (\frac{\partial \phi}{\partial z})^2] dA \\
=& \frac{\epsilon_u}{8\pi} \iint_{A_{1,2}B_{1,2}} [(\frac{\partial \tilde{\phi}}{\partial x})^2 + 2\cos\beta \frac{\partial \tilde{\phi}}{\partial x} - (\frac{\partial \tilde{\phi}}{\partial y})^2 - 2\sin\beta \frac{\partial \tilde{\phi}}{\partial y} - (\frac{\partial \tilde{\phi}}{\partial z})^2] dA.
\end{aligned}
\tag{E.3}
$$

Similarly,

$$
F_y^u = \frac{\epsilon_u}{4\pi} \iint [\frac{\partial \tilde{\phi}}{\partial x} \frac{\partial \tilde{\phi}}{\partial y} + \sin\beta \frac{\partial \tilde{\phi}}{\partial x} + \cos\beta \frac{\partial \tilde{\phi}}{\partial y}] dA. \tag{E.4}
$$

Since particles are widely separated, we assume the induced potential at $A_{1,2}B_{1,2}$ is a superposition of the far field potentials of the two particles,

$$
\tilde{\phi}^k \sim \tilde{\phi}_1^k + \tilde{\phi}_2^k, \tag{E.5}
$$

where $k = u, l$ and at the leading order

$$
\tilde{\phi}_1^k \sim \bar{C}_2^k \cos\beta \frac{x + R0/2}{R_1^3} + \bar{C}_2^k \sin\beta \frac{y}{R_1^3}, \tag{E.6}
$$

and

$$
\tilde{\phi}_2^k \sim \bar{C}_2^k \cos\beta \frac{x - R0/2}{R_2^3} + \bar{C}_2^k \sin\beta \frac{y}{R_2^3}, \tag{E.7}
$$

and $R_1 = \sqrt{(x + R0/2)^2 + y^2 + y^2}$, $R_2 = \sqrt{(x - R0/2)^2 + y^2 + y^2}$.

Substitute eqs. (E.5) to (E.7) into eqs. (E.3) and (E.4) and summing up the contributions from upper and lower surface, we obtain the analytic expression of particle interaction in x and y directions. At the nonzero leading order ($O(R_0^{-4})$) the forces are,

$$F^x = \frac{\epsilon_u + \epsilon_l}{2} \frac{3(\bar{C}_2)^2}{2R_0^4}(1 + 3\cos 2\beta), \quad F^y = -\frac{\epsilon_u + \epsilon_l}{2} \frac{3(\bar{C}_2)^2}{R_0^4} \sin 2\beta. \tag{E.8}$$

Note that higher order expansions in eqs. (E.6) and (E.7) do not contribute at the order $O(R_0^{-4})$. In spite of a difference in setting up the coordinate system, Equation (E.8) is equivalent to eq. (3.113).

APPENDIX F

Proving $\mathcal{F}^{\mathcal{I}}_{c3,d} = \frac{5}{3}\mathcal{F}^{\mathcal{I}}_{c,d}$ when $\gamma = \epsilon$ in Chapter 3

We call

$$W_{c3} = (\Sigma^k_{c3,11}, \Sigma^k_{c3,12}, \Sigma^k_{c3,13}),$$

$$W_c = (\Sigma^k_{c,11}, \Sigma^k_{c,12}, \Sigma^k_{c,13}),$$

are the contributions depending on $\cos 3\beta$ and $\cos\beta$ in eqs. (3.106) to (3.108), respectively. Then,

$$\mathcal{F}^{\mathcal{I}}_{c3,d} = 4(\epsilon_{ul} \iint_{S_u} W_{c3} \cdot d\mathbf{S} + \iint_{S_l} W_{c3} \cdot d\mathbf{S}),$$

$$\mathcal{F}^{\mathcal{I}}_{c,d} = 4(\epsilon_{ul} \iint_{S_u} W_c \cdot d\mathbf{S} + \iint_{S_l} W_c \cdot d\mathbf{S}).$$

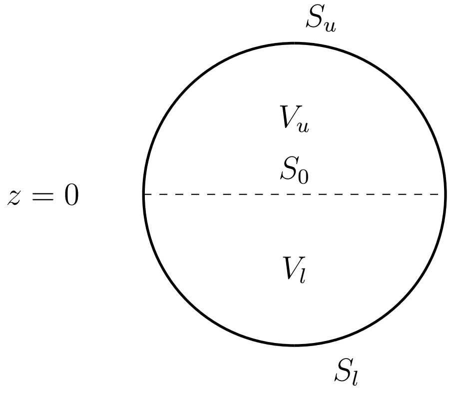

Figure F.1. Geometry of applying divergence theorem.

Note that W_{c3} and W_c are continuously differentiable in the whole space. Applying divergence theorem (see fig. F.1),

$$\begin{aligned}
\iint_{S_u} W_{c3}\cdot d\mathbf{S} &= \iiint_{V_u} (\nabla\cdot W_{c3})dV + \iint_{S_0} W_{c3}\cdot \mathbf{e_z dA} \\
&= \iiint_{V_u} [5(1+\frac{\partial\Phi_{k,1}}{\partial x} + x\frac{\partial^2\Phi_{k,1}}{\partial x^2} + y\frac{\partial^2\Phi_{k,1}}{\partial x\partial y})+ \\
&\quad 5(x\frac{\partial^2\Phi_{k,1}}{\partial y^2} - 1 - \frac{\partial\Phi_{k,1}}{\partial x} - y\frac{\partial^2\Phi_{k,1}}{\partial x\partial y}) + 5x\frac{\partial^2\Phi_{k,1}}{\partial z^2}]dV+ \\
&\quad \iint_{S_0} 5\frac{\partial\Phi_{k,1}}{\partial z}xdA \\
&=5\iiint_{V_u} (x\frac{\partial^2\Phi_{k,1}}{\partial x^2} + x\frac{\partial^2\Phi_{k,1}}{\partial y^2} + x\frac{\partial^2\Phi_{k,1}}{\partial z^2})dV \\
&\quad + \iint_{S_0} 5\frac{\partial\Phi_{k,1}}{\partial z}xdA \\
&= \iint_{S_0} 5\frac{\partial\Phi_{k,1}}{\partial z}xdA.
\end{aligned}$$

. And,

$$\begin{aligned}
\iint_{S_u} W_c\cdot d\mathbf{S} &= \iiint_{V_u} (\nabla\cdot W_c)dV + \iint_{S_0} W_c\cdot \mathbf{e_z dA} \\
&= \iiint_{V_u} [3(1+\frac{\partial\Phi_{k,1}}{\partial x} + x\frac{\partial^2\Phi_{k,1}}{\partial x^2}) - y\frac{\partial^2\Phi_{k,1}}{\partial x\partial y} + 4z\frac{\partial^2\Phi_{k,1}}{\partial z\partial x} + 3x\frac{\partial^2\Phi_{k,1}}{\partial y^2}+ \\
&\quad (x\frac{\partial^2\Phi_{k,1}}{\partial x\partial y} + 1 + \frac{\partial\Phi_{k,1}}{\partial x}) - 4(1+\frac{\partial\Phi_{k,1}}{\partial x} + z\frac{\partial^2\Phi_{k,1}}{\partial z\partial x}) + 3x\frac{\partial^2\Phi_{k,1}}{\partial z^2}]dV+ \\
&\quad \iint_{S_0} 3\frac{\partial\Phi_{k,1}}{\partial z}xdA \\
&=3\iiint_{V_u} (x\frac{\partial^2\Phi_{k,1}}{\partial x^2} + x\frac{\partial^2\Phi_{k,1}}{\partial y^2} + x\frac{\partial^2\Phi_{k,1}}{\partial z^2})dV \\
&\quad + \iint_{S_0} 3\frac{\partial\Phi_{k,1}}{\partial z}xdA \\
&= \iint_{S_0} 3\frac{\partial\Phi_{k,1}}{\partial z}xdA.
\end{aligned}$$

.

From a similar proof, we have $\iint_{S_l} W_{c3} \cdot d\mathbf{S} = \frac{5}{3} \iint_{S_l} W_c \cdot d\mathbf{S}$. Thus

$$\mathcal{F}^{\mathcal{I}}_{c3,d} = \frac{5}{3}\mathcal{F}^{\mathcal{I}}_{c,d}.$$

Following the same calculation, we can also obtain $\mathcal{F}^{\mathcal{I}}_{s3,d} = \frac{5}{3}\mathcal{F}^{\mathcal{I}}_{c,d}$ and $\mathcal{F}^{\mathcal{I}}_{s,d} = \frac{1}{3}\mathcal{F}^{\mathcal{I}}_{c,d}$.